



Dilute Magnetic Semiconductors: the role of *Mn* in *GaMnAs*(001) and *Mn/GaAs*(001) surfaces

A thesis presented by

Stephen Denny Thorpe

to

Physics Department

in partial fulfillment of the requirements
for the degree of

Doctor of Philosophy

in the subject of

Physics

University of Rome "Tor Vergata"

Rome, Italy - December 2009

Supervisors

Prof. A. Balzarotti
Colonna (ISM-CNR)

PhD Coordinator

Prof. P. Picozza Dr. S.

© [2009] by [Stephen Denny Thorpe]

All rights reserved.

Index

1. Introduction	3
1.1 Spintronics	3
1.2 Magnetic semiconductor	5
References	7
2. Non magnetic semiconductor <i>GaAs</i> surface	9
2.1 General aspects	9
2.2 The electronic counting rule	11
2.3 Arsenic rich structure: (2×4) and (4×4) reconstructions	14
2.4 (110) surface structure	23
References	27
3. Dilute Magnetic Semiconductor (DMS)	31
3.1 Overview	31
3.2 Structural properties	32
3.3 Electronic properties	34
3.4 Magnetic properties	36
3.5 Defects	39
3.6 <i>Mn</i> deposition on <i>GaAs</i>	41
References	43
4. Experimental Techniques	47
4.1 Overview	47
4.2 Molecular Beam Epitaxy (<i>MBE</i>)	47
4.2.1. Growth of <i>GaAs</i> and <i>GaMnAs</i> with <i>MBE</i>	49
4.2.2. <i>MBE</i> growth	52
4.2.3. Molecular flux and growth rate measured by <i>RHEED</i>	54
4.3 Low Energy Electron Diffraction (<i>LEED</i>) and Reflected High Energy Electron Diffraction (<i>RHEED</i>)	57
4.3.1. Theory of surface scattering	57
4.3.2. <i>LEED</i>	61
4.3.3. <i>RHEED</i>	64

4.4	Electron Energy Loss Spectroscopy	67
4.4.1.	Small angle inelastic scattering	71
4.5	Scanning Tunneling Microscopy (<i>STM</i>)	75
4.6	Photoemission Spectroscopy (<i>PES</i>) and Photoelectron Diffraction (<i>PED</i>)	79
4.6.1.	Photoelectron Diffraction (<i>PED</i>)	81
4.7	Reflectivity Anisotropy Spectroscopy (<i>RAS</i>)	85
	References	88
5.	Growth and characterization of <i>GaAs</i> and $Ga_{1-x}Mn_xAs$	91
5.1	Introduction	91
5.2	<i>GaAs</i> preparation	92
5.3	<i>GaMnAs</i> preparation	96
5.4	Magnetic characterization	97
5.5	Structural characterization	101
	References	107
6.	<i>GaMnAs</i>(001) and <i>Mn/GaAs</i>(001) surface characterization	111
6.1	Introduction	111
6.2	<i>GaMnAs</i> (001)	112
6.2.1.	Experimental results	115
6.3	<i>Mn/GaAs</i> (001). Experimental results	126
	References	142
7.	Conclusions	145
	Appendix. Future development	147
A.	Cross sectional <i>STM</i> measurement of <i>GaMnAs</i> (001) surface	147
B.	<i>STM</i> measurement on <i>Mn: GaAs</i> (001) $\beta 2(2 \times 4)$ surface	152
	References	156

Chapter 1

Introduction

1.1. Spintronics

Spintronics is an emergent technology that exploits the quantum feature of the electron to spin and makes use of its charge state [1,2]. The spin itself is manifested as a detectable weak magnetic energy state characterized as spin up or spin down. Conventional electronic devices rely on the transport of electrical charge carriers – electrons – to a semiconductor such silicon or gallium arsenide. Now, however, device engineers and physicists are inevitably dealing with the looming presence of quantum mechanics and are trying to exploit the spin of the electron rather than its charge. Devices that rely on the electron spin to perform their function form the foundations of spintronics (short of spin-based electronics), also known as magnetoelectronics [3]. Spintronics devices are smaller than 100 *nm* in size, more versatile and faster than those commercially used for making up processing chips and circuit elements. The potential market is worth hundreds of billions of Euros per annum [4].

Spintronics burst on the scene in 1988 when Albert Fert and Peter Grünberg discovered a very powerful effect called Giant Magnetoresistance (*GMR*) that rewarded their efforts with the Nobel prize in 2007: “The discovery of *GMR* opened the door to a new field of science, magnetoelectronics (or spintronics), where two fundamental properties of the electron, namely its charge and its spin, are simultaneously manipulated. While emerging nanotechnology was an original prerequisite for the discovery of *GMR*, at present magnetoelectronics are in turn a driving force for new applications of nanotechnology. In this field, demanding and exciting scientific and technological challenges become

intertwined, strongly reinforcing progress.”¹ The *GMR* results from subtle electron- spin effects in ultra thin multilayers of magnetic materials which cause huge changes in their electrical resistance when a magnetic field is applied. This mechanism resulted in the first spintronics device in the form of the spin valve. The incorporation of *GMR* materials into read heads allowed the storage capacity of a hard disk to increase from one to 20 gigabits. In 1997, IBM launched GMR read heads, into a market worth around a billion dollars per annum. This field of research is relatively young and it is difficult to forecast how it will evolve. This aspect is directly depending on new materials that the scientific community of Material Science is studying such as magnetic semiconductor and an exotic and more extreme effect called Colossal Magnetoresistance (*CMR*) [5].

Spintronics materials research is an important area of the nanomaterials science to both fundamental scientific research and industrial applications. These new devices are expected to be non-volatile, versatile, fast and capable of simultaneous data storage and processing, while consuming less energy. They are playing an increasingly significant role in high-density data storage, microelectronics, sensors, quantum computing, bio-medical applications, etc. It is expected that the development of spintronics to the microelectronics industry might be comparable to the development that the transistor roused 50 years ago. Nowadays every computer user already has a spintronics device on his desktop, as all modern computers use the spin valve to read and write data on their hard drive. It was immediately followed by the discovery of Tunneling Magnetoresistance (*TMR*) leading to the magnetic tunnel junction that has been utilized for the Magnetic Access Memory (*MRAM*) in commerce since 2004 [6, 7]. At present the research is concentrated on the fabrication of spin transistors and spin logics devices integrating magnetic and semiconductors, with the aim of improving the existing capabilities of electronic transistors and logics devices so that the future computation and thus the future computers could become faster and consume less energy.

The four main investigation areas in spintronics are:

- I. Understanding the fundamental physics, such as spin-dependent transports across the magnetic/semiconductor interfaces and spin coherence length in semiconductors;

¹ Scientific Background on the Nobel Prize in Physics 2007: www.nobelprize.org

- II. Synthesizing suitable spintronics materials with as higher as possible Curie Temperature, large spin polarization at the Fermi level and matching conductivity between the magnetic and semiconductor materials;
- III. Fabricating devices with nanometers feature sizes and developing new techniques for mass production;
- IV. Integrating spin-devices with current microelectronics and computing and elaborating again all the logics based on the quantum mechanics in order to improve the development of the quantum computing.

1.2. Magnetic semiconductors

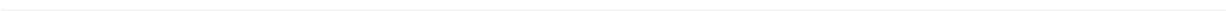
The first discovery of interplay between semiconducting bulk properties and ferromagnetism was the europium chalcogenides, a semiconductors spinels produce a great interest and the desire to improve the study of this materials in the 1960's and 1970's. In the 80's the technical difficulties of the preparation of single crystals and the low Curie temperature made this interest to become much lower. The second generation of ferromagnetic semiconductor was based on non magnetic semiconductors alloyed with magnetic elements (mostly transition metals). Such alloys between a nonmagnetic semiconductor host and magnetic elements in a low concentration (about 2%) are called dilute magnetic semiconductors (*DMS*) [8]. The first choice was *II – VI* compounds (like *ZnSe* and *CdTe*) because of the compatibility of the valence of cations (s^2) with that of typical magnetic elements $3d^54s^2$ like *Mn*. These materials exhibit a great change in their properties upon application of magnetic fields due to the exchange interaction between the conduction carriers and the localized magnetic moments. This magnetism was limited to paramagnetism or spin glasses resulting from antiferromagnetic superexchange interactions among magnetic ions. The discovery of ferromagnetism in *III – V* based *DMS's* (*In, Mn*)*As* and (*Ga, Mn*)*As* [9], has opened a unique opportunity of introducing ferromagnetism in the semiconductor which was already in use in electronics applications (lasers and transistors) and integrating ferromagnetism in semiconductor heterostructures. The highest transition temperature (T_c) obtained in (*Ga, Mn*)*As* is 170K [10], still below room temperature but

above liquid nitrogen temperature so to be useable for special applications. However, a model for the ferromagnetism capable to describe a number of experimental observation suggests a route to above room temperature ferromagnetism in the family of tetrahedrally bonded semiconductors like *III – V* compounds.

The aim of this thesis is to study the behavior of *Mn* in the *GaMnAs*(001) surface and to increase the comprehension of *Mn* incorporation on *GaAs* lattice by depositing *Mn* on the *GaAs*(001) surface with successive annealing treatments. The target is to understand the procedure for grow high quality *GaMnAs* films with high T_c (ideally room temperature) useful for several applications in spintronics and, furthermore, to improve knowledge of electronic properties for spin injection [11]. In Chapters 2 and 3 the *GaAs* and *GaMnAs* structures will be explained with all the surface reconstructions and electronic and magnetic properties. In Chapter 4 an overview of all experimental techniques used in this thesis will be shown. Chapter 5 is dedicated to the growth of *GaAs* and *GaMnAs* with magnetic and structural characterizations. All the experimental results are presented and discussed in Chapter 6.

References

- [1] S. A. Wolf, D. D. Awschalom, R. A. Buhrman, J. M. Daughton, S. von Molnár, M. L. Roukes, A. Y. Chtchelkanova, and D. M. Treger *Science* **294** 1488 (2001).
 - [2] Masaaki Tanaka *Journal of Crystal Growth* **278** 25-37 (2005).
 - [3] Gary A. Prinz *Science* **282** 1660 (1998).
 - [4] David D. Awschalom and Michael E. Flattè *Nature Physics* **3** 153 (2007).
 - [5] A. P. Ramirez *J. Phys. Condens. Matter* **9** 8171–8199 (1997).
 - [6] T. Dietl and H. Ohno *Materials Today* **9** 18 (2006).
 - [7] Katrin Pappert, Silvia Hümpfner, Charles Gould, Jan Wensch, Karl Brunner, Georg Schmidt, Laurens W. Molenkamp *Nature Physics* **3** 573 (2007).
 - [8] H. Munekata, H. Ohno, S. von Molnar, Armin Segmüller, L. L. Chang, and L. Esaki *Physical Review Letters* **63** 1849 (1989).
 - [9] H. Ohno *Science* **281** 951 (1998).
 - [10] Kenichi Ohno, Shinobu Ohya and Masaaki Tanaka *Journal of Superconductivity and Novel Magnetism* **20** 417 (2007).
 - [11] Y. Ohno, D. K. Young, B. Beschoten, F. Matsukura, H. Ohno and D. D. Awschalom *Nature* **402** 790 (1999).
-



Chapter 2

Non magnetic semiconductor *GaAs* surface

2.1. General aspects

The clean *GaAs* is a typical *III – V* semiconductor compound with a zincblende structure where *Ga* occupy the cubic cell and *As* tetrahedral position. The natural growth surface is a face of the cubic cell, typically the (001) surface. Because the zincblende crystal structure has a tetrahedral coordination in the bulk, the polar *GaAs*(001) surface could be *Ga* or *As* terminated (fig. 2.1). Compared to *Ge* and *Si* and to the *GaAs* cleaved (110) surface, a successful sample preparation is more difficult for *GaAs*(001) [1,2]. In fact preparation of a well ordered and clean *III – V* (001) surface usually requires a growth apparatus such as molecular beam epitaxy (**MBE**) or metal organic chemical vapor deposition (**MOCVD**) reactor. After the growth an *As* capping layer deposited on the sample surface can be used to prevent air contamination. The *As* decapping technique can be used to produce high quality surfaces, but one must be careful and the expected results are often missing in quality in comparison to **MBE** samples.

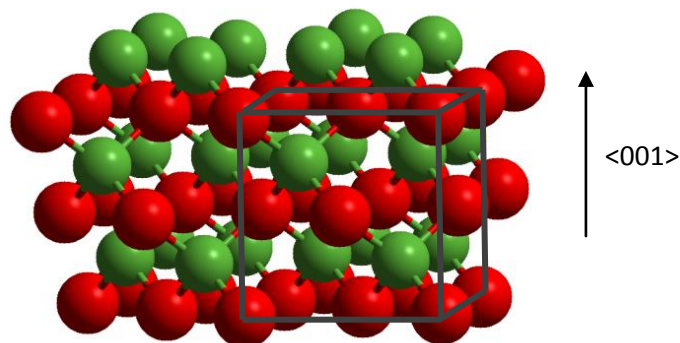


Fig.2.1. *GaAs* bulk terminated structure. Green balls are *As* atoms, red balls are *Ga* atoms.

An alternative method of preparation is to treat the $GaAs(001)$ surface with HCl and propanol in N_2 flux, followed by annealing in UHV . Anyway, in both cases annealing without As flux can lead to the formation of Ga droplets and to non stoichiometric surfaces since As is volatile. Moreover, $GaAs(001)$ surfaces involve an additional degree of freedom due to stoichiometry dependent reconstructions. Depending on the thickness of the grown sample and on experimental conditions, the surface exhibits a number of reconstructions, starting with the most As rich phase, which has the $c(4 \times 4)$ symmetry, through the (2×4) phase including the off-phase $c(2 \times 8)$ (similar to (2×4) phase but with $2 \times$ periodicity respect to previous row), (1×6) , (4×6) , and ending with the Ga stabilized phases (4×2) and (8×2) . Experimental and theoretical studies have resulted in the establishment of two basic and general features in the structure of the $GaAs(001)$ surface. To find the reconstruction with lowest energy for a given anion chemical potential μ_A that depends on the preparation conditions (like temperature and pressure), the surface stoichiometry and geometry at a given μ_A , has to be compared with the surface energy Ω_s determined by surface models (in fig. 2.2 the example of $GaAs(001)$ is presented). At a certain temperature there is a probability c_s that one surface phase is formed [3]:

$$c_s \approx \exp \left[\frac{-(m \times n)\Omega_s}{K_B T} \right]$$

where $(m \times n)\Omega_s$ is the formation energy of one determined surface $(m \times n)$ reconstruction. In general this probability is also influenced by entropy effect ($d\Omega_s = -S_{surface} dT$) which can modify the stability of a phase at a given temperature. In the gaseous phases the effect of temperature T and pressure p upon the chemical potentials is much more important than for condensed states. The chemical potentials μ_i depend logarithmically upon T and p and the large variation of μ_i can be used to control the state of condensed phases in equilibrium with the gas.

The stability of all reconstructions can be substantiated by a simple but practical rule, the electron counting rule (ECR) [4,5], illustrated in the next paragraph.

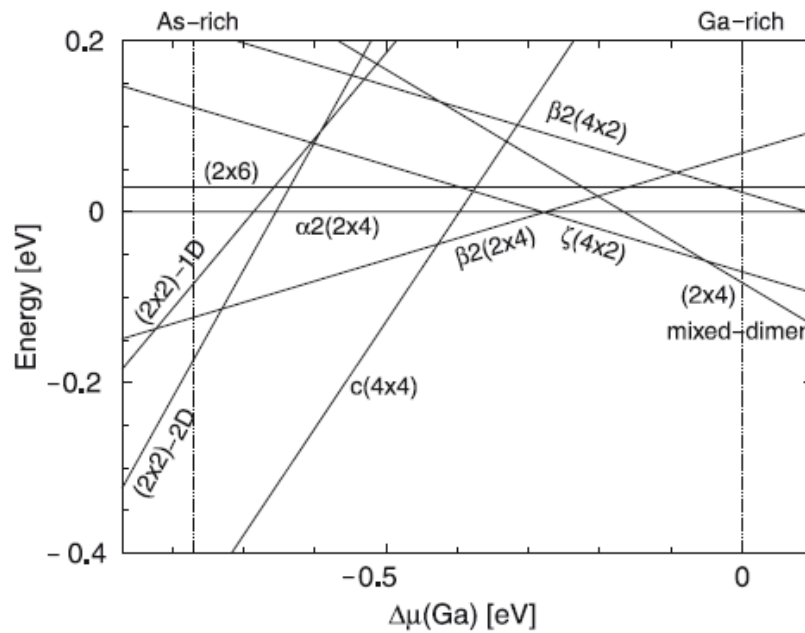


Fig. 2.2. $GaAs(001)$ surface energies as a function of Ga chemical potential for a unit cell.

2.2. The electron counting rule (ECR)

The atoms in the $GaAs$ bulk are sp^3 hybridized. Two hybridized orbitals, one from each type of atom, combine to form a two orbitals: bonding and antibonding. But at the surface some hybrid orbitals cannot form bonds, so partially filled sp^3 dangling bonds will remain without reconstruction. Final dangling bonds energies can be estimated from the starting energies of the s and p atomic levels. In fig. 2.3 can be seen the dangling bond energy level for Ga (electropositive element) that should be empty since it is in the conduction band, and the dangling bond energy level for As (electronegative element) that should therefore be filled since it is in the valence band. To achieve this, electrons transfer from Ga dangling bond to As dangling bond. However, charge transfer induces additional static electric capacitance energy due to charge accumulation, the resulting surface becomes energetically unstable unless some amount of dimers is removed from the surface to compensate this energy and achieve charge neutrality. Dimer missing characterizes the reconstruction of the $GaAs(001)$ surface, which is further generalized by *ECR*.

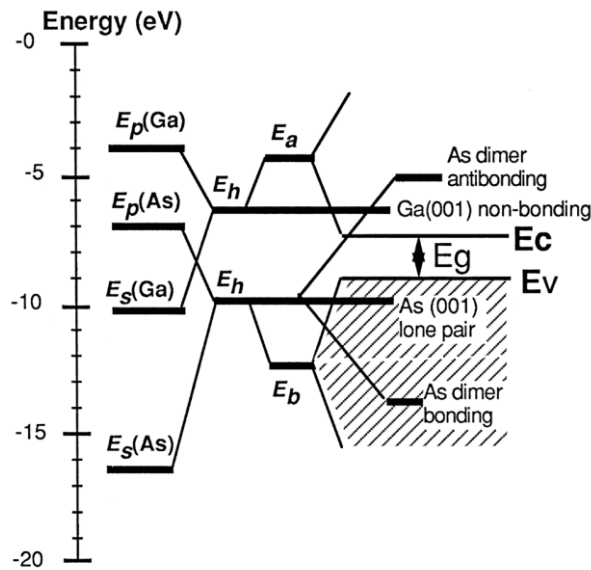


Fig.2.3. The energy levels diagram of $GaAs$ and its application to the (001) As -terminated surface. The hybrid energy levels E_h , are derived from the s and p orbitals; two of the As hybrids are unbounded sp^3 hybrid dangling bonds. Subsequent dimerization produces an $As - As$ dimer bonding and antibonding combination, leaving one As dangling bond per atom at the hybrid energy, E_h . Charge transfer from the underlying Ga into this state produces a filled lone pair orbital.

ECR requires that a stable surface structure is formed when the number of available electrons in the surface layer exactly fills all dangling bond states in the valence band, leaving those in the conduction band completely empty. This rule dictates that there should be no net charge leaving on the surface. With further lattice distortion, the surface energy band structure becomes more semiconducting, whereas partially filled dangling bonds may lead to a metallic surface resulting in a unstable structure. In general surface reconstructions and surface relaxations follow 3 guiding principles:

1. A surface tends to minimize the number of dangling bond by the formation of new bonds. The remaining dangling bonds tend to be saturated;
2. A surface tends to compensate charges;
3. A semiconductor surface tends to be insulating or semiconducting.

The lowest energy structure is obtained with filled states dangling bonds on the electronegative element (with V_n valence electrons) and empty dangling bonds on the electropositive element (with V_p valence electrons). To apply the principles exposed above

to $GaAs(001)$, we consider the As -rich surface with a missing As -dimer; the unit cell consists of D dimers with every N -th dimer missing, namely the surface has the $2 \times$ reconstruction; so the surface forms a $(2 \times N)$ reconstruction with $2 \times$ being the periodicity coming from the formation of As dimers and $N \times$ being the periodicity of missing surface dimers, leaving D dimers per unit cell where $D \leq N$. We now count up the numbers of electrons required to satisfy these conditions and equate that with the numbers of electron available in order to determine the relationship between N and D . Thus from Fig. 2.4 each top layer dimer requires six electrons (two in each dangling bonds and two in the dimer bond), making $6D$ electrons in total in the top layer per surface crystallographic cell.

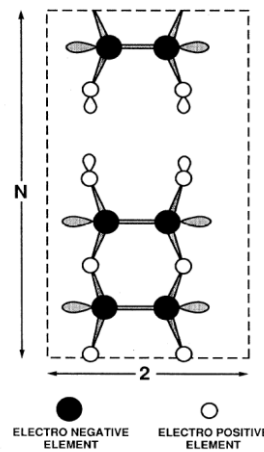


Fig.2.4. The bonds and dandling bonds, both filled (shaded) and empty (open), for $(2 \times N)$ a unit cell on the surface of a polar semiconductor with the zincblende crystal structure, where the 2 periodicity arises from missing dimers.

A total of $8D$ electrons are required to bond the dimers to the second layer of atom. The numbers of electrons available from the top-layer atoms is $2V_n D$, and the numbers of electrons available from the second layer is $2V_p N/2$ (since half of the total electrons from the second layer are involved in bonding to the third layer). Thus, a stable structure is obtained when: $6D + 8D = 2V_n D + 2V_p N/2$. In the case of our system, $V_n = 5$ and $V_p = 3$, thus $4D = 3N$. The smallest unit cell that satisfies this condition is the unit cell containing three dimers with every fourth dimer missing. If deeper layer atoms are involved in the reconstruction, consideration of ECR will give rise to additional two dimers models.

2.3. Arsenic rich surface structure: (2×4) and (4×4) reconstruction

The $GaAs(001)$ surface shows a $c(4 \times 4)$ symmetry for As –rich conditions, but changes its periodicity to $(2 \times 4)/c(2 \times 8)$ and finally $(4 \times 2)/c(8 \times 2)$ as the surface gets more Ga –rich. In addition, a large variety of transient structures or apparent symmetries such as (2×3) , (2×1) , (3×1) , (3×6) , (2×6) , (6×6) , (4×6) , etc., are reported [1–4]. The large number of observed surface structures have prompted the necessity to classify and understand them from a more general point of view. For example the ECR was recognized to govern many reconstructions. The ECR together with the dimerization as the major mechanism to reduce the number of dangling bonds on $GaAs(001)$ surface were able to successfully explain a large number of surface geometries. This success prompted Mönch to write [6]: “The electronic energy of such surfaces will be lowest when

- a) surface atoms in the top layer are forming dimers and
- b) dangling bonds are filled on surface anions (As) and are empty at the surface cations (Ga)”.

The (2×4) reconstruction has been extensively studied because is usually observed during MBE growth in As –rich condition. Several (2×4) structural models, summarized in fig. 2.5, satisfying ECR have been proposed.

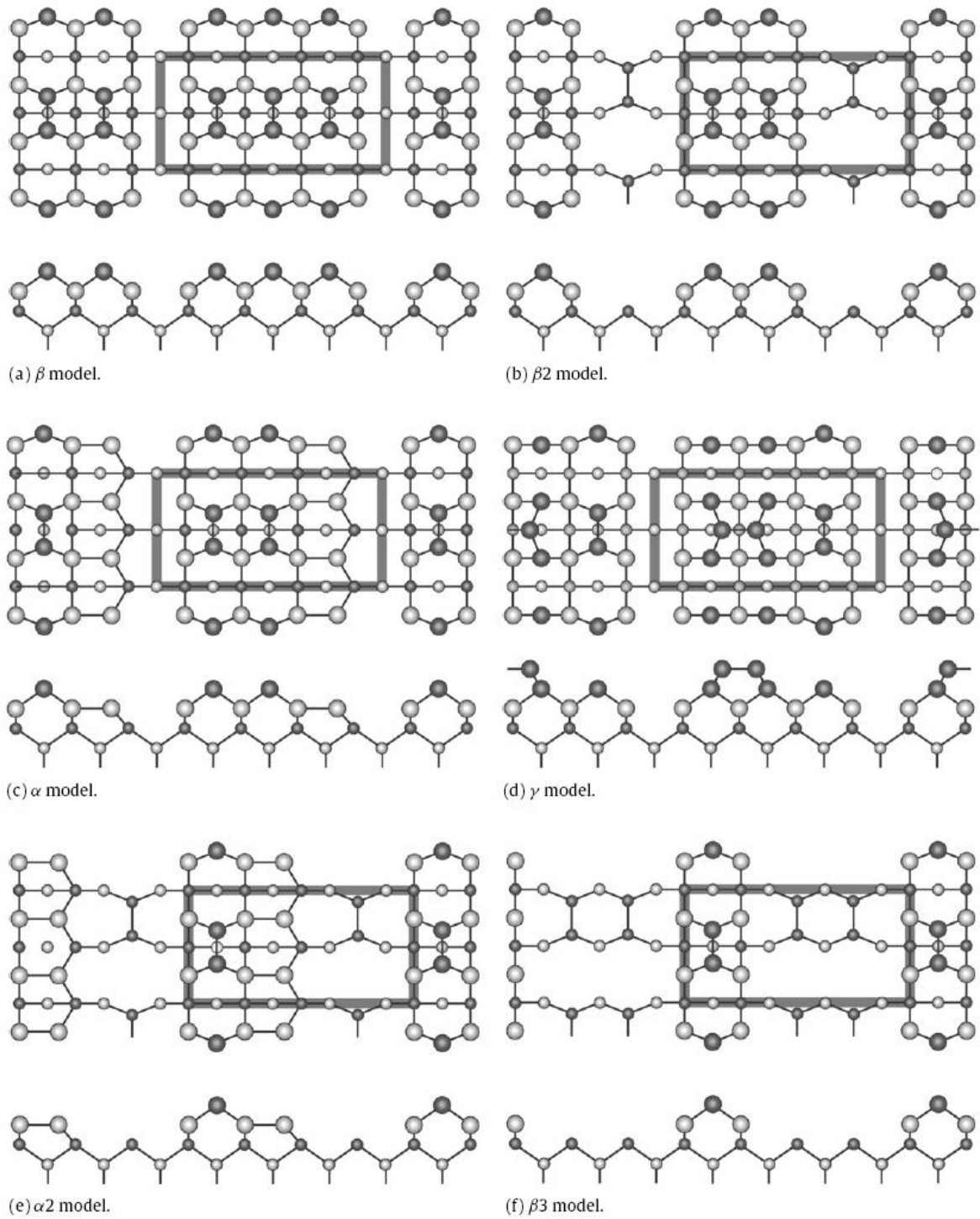


Fig.2.5. Top and side views of the relaxed $GaAs(001)(2 \times 4)$ α , β_2 , and β phases. Large (small) filled circles indicate top-(third-) layer As atoms, whereas large (small) empty circles represent second- (fourth-) layer Ga atoms. The γ phase has five layers [26].

The (2×4) $GaAs(001)$ surface is known to exhibit a very rich variety of ordered phases whose occurrence depends on the preparation conditions [7,8] and correlating, characteristic patterns with the surface stoichiometry, can be distinguished between three (2×4) phases, called α , β and γ [9]. The α phase occurs at the highest substrate temperature and was suggested to correspond to a geometry combining two As dimers in the uppermost atomic layer with $Ga - Ga$ bonds in the layer underneath. Schmidt et al. showed recently that the same stoichiometry can be realized with an energetically more favored structure, called $\alpha 2(2 \times 4)$ [10]. This structure, shown in fig. 2.5, is $0.034 eV$ per (1×1) unit cell lower in energy than the α model. The α structure will be unstable with respect to $\alpha 2$ irrespective of the surface-preparation conditions. The structural difference consists in the fact that the α model has two $As - As$ dimers in the first layer and the $\alpha 2$ has one $As - As$ dimer in the first layer and one in the third layer (Fig. 2.5 (c) and Fig. 2.5 (e)). The β phase (Fig. 2.5 (a)), which is stable for more anion-rich conditions, was explained originally by the three-dimer model due to Chadi [11]. Northrup and Froyen [12] later showed that a somewhat modified structure, called $\beta 2$ (Fig. 2.5 (b)), leads to a lower electrostatic energy and is energetically favored. The structure model shown in Fig. 2.5(a) contains three $As - As$ dimers, and is now referred to as the $\beta(2 \times 4)$ model. The model shown in Fig. 2.5(b) contains two As dimers in the outermost atomic layer with a third As dimer situated in the third atomic layer, within the trench formed due to missing dimers (so called $\beta 2(2 \times 4)$ model). The STM images in Fig. 2.6 shows the $\beta 2$ structure with the two dimers in the top layer inside the unit cell. The reconstruction depends on the growth conditions [12].

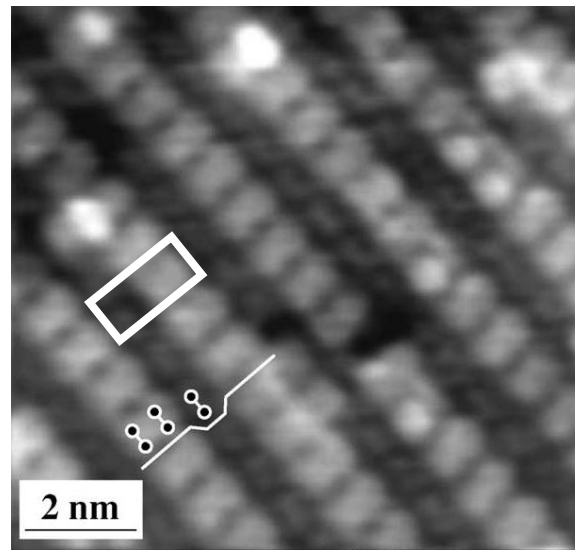


Fig. 2.6. *STM* image of $\beta 2(2 \times 4)$ at -2.1 V and 0.3 nA. The white rectangle represents the unit cell [12].

While the *ECR* gives an indication of which structures might be stable and which should not be, it does not allow us to discriminate energetically between two structures complying with the electron-counting principle. A major progress in that respect was the work by Northrup and Froyen on the role of electrostatic interactions between the surface structural units [12]. They showed that Coulomb repulsion between negatively charged *As* dimers favours the two-dimer $\beta 2(2 \times 4)$ structure over the three-dimer $\beta(2 \times 4)$ structure. Based on similar electrostatic arguments, Schmidt et al. [10] predicted recently that a one-dimer $\alpha 2(2 \times 4)$ structure should be lower in energy than the hitherto accepted $\alpha(2 \times 4)$ model. The estimation of relative surface energies from empirical concepts was further refined by Zhang and Zunger [14], who observed that the large collection of equilibrium surface structures is built from a limited number of recurring local structural motifs, such as threefold-coordinated pyramidal anions or surface dimers. The energies of these structural motifs can be obtained from a fit to the results of *ab initio* calculations on flat surfaces and bulk defects. Based on motif energies obtained in such a way, Zhang and Zunger estimated the surface energies for reconstructions larger than what could be dealt with from first principles at that time. Starting from atomic energy levels and bonding energies, Mirbt et al. derived a very simple expression called a surface reconstruction parameter in order to assess the stability of reconstruction models. According to this parameter, for the stability of

III – V surfaces it is required that under cation-rich conditions the sum of anion dangling bonds and anion–anion bonds should be minimized. For anion-rich conditions the expression $N_a - N_{a-a} + 2N_{c-c}$ needs to be minimized, where N_a is the number of anion dangling bonds and N_{a-a} and N_{c-c} denote the numbers of anion–anion and cation–cation bonds. Later, the same group pointed out how local stress may modify these rules [15].

The β and $\beta 2$ models were found to have the same energies and to be more stable than the structure with only two dimers (Fig. 2.5(c)). Other total-energy calculations [16, 17, 18] confirmed this result. The actual occurrence of the $\beta 2(2 \times 4)$ structure was proven by in situ grazing incidence *X – ray* diffraction measurements [19], dynamical **RHEED** analysis [20] and very recently by highly resolved **STM** images [21]. The γ phase, finally, occurring for even more *As*-rich surfaces, was found to be a mixture of the β phase and the $c(4 \times 4)$ phase, with the surface *As* coverage varying depending on the actual growth conditions [22, 23]. Moll et al. [18] performed total-energy calculations for several $c(4 \times 4)$ structures. In agreement with the present study, Sauvage-Simkin et al. [24] find the three dimers structure to have the lowest energy (cf. Fig. 2.5). Avery et al. proposed that the γ phase involves kink formation due to the preferential occupation by additional *As* atoms of second layer *Ga* sites in the missing dimer trenches of the $\beta 2(2 \times 4)$ structure [25]. The α and β phases emerge under less and more *As*-rich **MBE** conditions, respectively. The *GaAs*(001)(2×4) surface consists of the well-ordered $\beta 2$ domains obtained in a relatively wide range of substrate temperature (500 – 600 °C) under *As* fluxes (about $3 \cdot 10^{-7}$ mbar). At the higher end of the temperature region of the (2×4) phase, the surface contains a high density of defects with a local atomic geometry identical to the $\alpha 2$ structure. On the other hand, the $\beta 2(2 \times 4)$ structure coexists with $c(4 \times 4)\alpha$ domains at the lower end of temperature region. In the $\beta 2$ structure, the outermost *As* atoms are in a p^3 - type bonding configuration, while *Ga* atoms in the second layer produce sp^2 –type bonds with their nearest neighbor. This atomic arrangement indicates that all of the *Ga* and *As* dangling bonds are eliminated by transferring charge from *Ga* atoms to *As* atoms. The $\beta 2$ structure is readily accessible in *As* –rich **MBE** conditions. Although other structures, such as β , α and $\alpha 2$, could be also formed under actual **MBE** conditions, they were only observed as local defects in the $\beta 2$ structures.

The $c(4 \times 4)$ reconstruction of the $GaAs(001)$ surface is usually observed under extremely *As*-rich *MBE* conditions, and, therefore, has been believed to be the most *As*-rich phase. Chang et al. first reported that the $c(4 \times 4)$ reconstruction is observed during the *MBE* growth when the *As/Ga* flux ratio is increased and/or the substrate temperature is lowered [27,28].

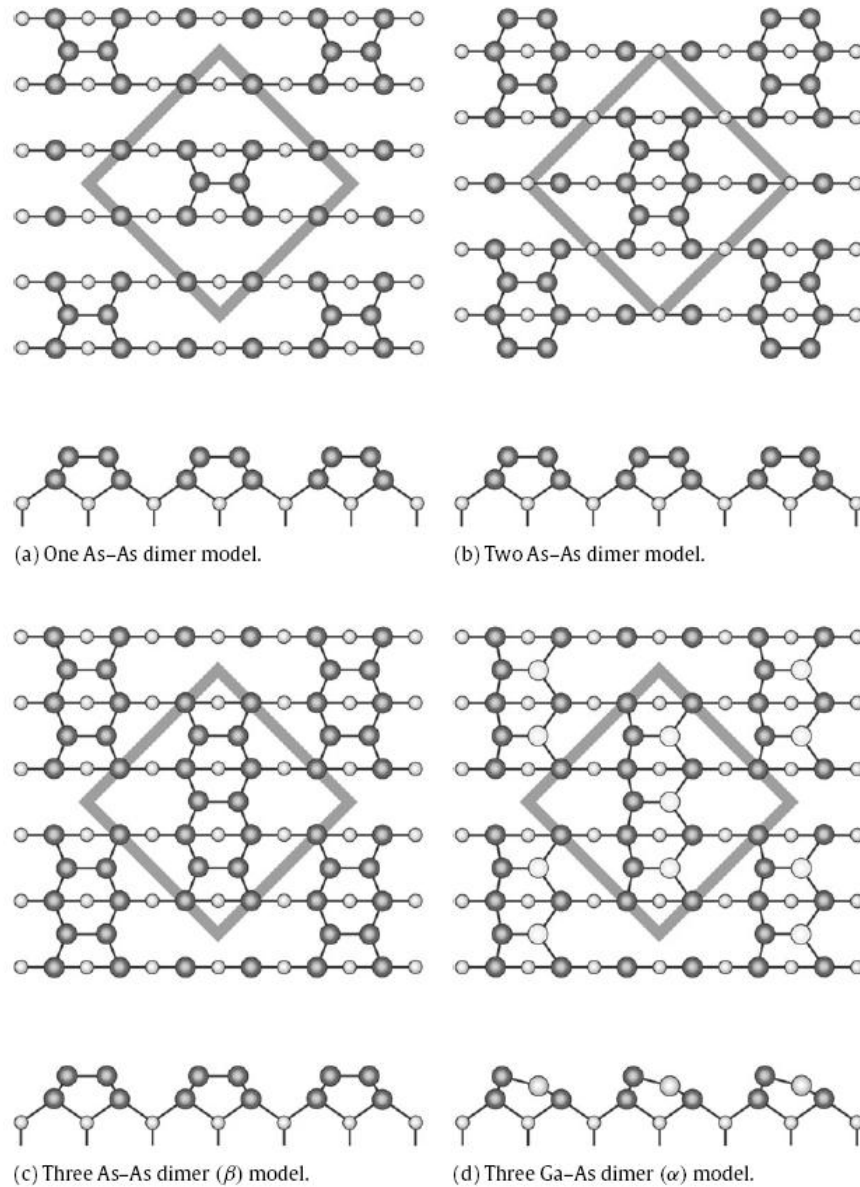


Fig.2.7. Top and side views of the relaxed $GaAs(001)c(4 \times 4)$ with one (a) two *As – As* dimers (b) or three *As-As* dimers (β phase) (c) and *As-Ga* dimers (α phase) (d) [26].

During the growth, when the substrate temperature is decreased from 540 to 200 °C under the As_4 flux, at 500 °C the (2×4) phase begins to evolve into the more *As*-rich phase of $c(4 \times 4)$, because the sticking probability of As_4 molecules increases with decreasing substrate temperature. Chadi, Tanner, and Ihm proposed the first structure model for the $c(4 \times 4)$ reconstruction, which consists of equal numbers of symmetric and asymmetric *As*–*As* dimers on the *Ga*-terminated surface [29]. This model was questioned by a combined **RHEED** and photoemission study: Larsen et al. [30] showed the existence of symmetric *As*–*As* dimers, and proposed two structure models shown in Fig. 2.7(a) and (b). These models have one (Fig. 2.7(a)) and two (fig. 2.7(b)) *As*–*As* dimers on the *As*-terminated surface per $c(4 \times 4)$ unit cell. Direct evidence of *As* dimers in the *GaAs*(001) – (4×4) reconstruction was obtained by grazing-incidence *X* – ray diffraction (**XRD**) measurements [31]: Sauvage-Simkin et al. showed that their **XRD** data can be explained only when a mixture of the two (Fig. 2.7(b)) and three *As*–*As* dimer models (Fig. 2.7(c)) is considered [31]. Similar results were reported by Sasaoka, Kato, and Usui [32]: the $c(4 \times 4)$ surface consists of the single (Fig. 2.7(a)) and three (Fig. 2.7(c)) *As*–*As* dimer models. The three *As*–*As* dimer model was also supported by **STM** observations [33, 34, 35] and was found to be stable by first principles calculations [12,18,36]. However, $c(4 \times 4)$ structures consisting of one and two *As* dimers have not been observed by **STM** [33, 34, 35] and the $c(4 \times 4)$ structure with two *As* dimers turned out to be unstable [18]. Recently, Ohtake et al. have proposed a new structure model consisting of three *Ga*–*As* dimers, instead of three *As*–*As* dimers, per $c(4 \times 4)$ unit cell (Fig. 2.7 (d)) [6]. Fig. 2.8 presents the typical blocks of this reconstruction; each block is formed by three *Ga*–*As* dimers.

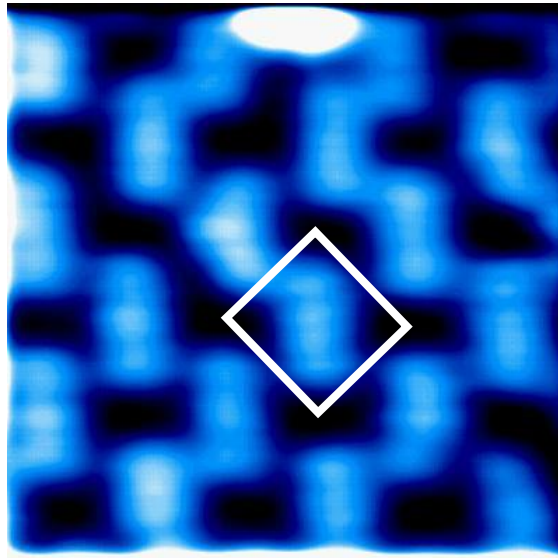


Fig.2.8. STM image of $c(4 \times 4)\alpha$ at -6 V and 0.3 nA 5×5 nm. The white rectangle represents the unit cell.

This model has been supported by **STM** observations [37,38,39], rocking-curve analysis of **RHEED** [37], **LEED** analysis [39], surface **X-ray diffraction** [40], **RDS** (Reflectance Differential Spectroscopy) [41], and first-principles calculations [36,38,41,42]. It is possible to observe the existence of two types of atomic structures for the $c(4 \times 4)$ phase that could explain the reported wide range of *As* coverage, and resolve disagreements in the interpretation of previous experiments. The results of **RDS** and **RHEED** rocking-curve measurements [43], suggested that there exists only one intrinsic reconstruction of $c(4 \times 4)$ under As_4 fluxes. Two types of $c(4 \times 4)$ reconstructions were observed when the As_2 molecular beam was used: the $c(4 \times 4)\alpha$ (*Ga-As* dimer structure) and the $c(4 \times 4)\beta$ (*As-As* dimer structure), depending on the preparation conditions (As_2 molecules is produced by cracking As_4 molecules above 750 °C); incident *As* molecular species play an important role in the formation of these phases. Both α and β structures do not have any unsaturated *Ga* and *As* dangling bonds. The $(4 \times 4)\beta$ structure, which is the most stable structure in the extremely *As*-rich condition, is formed under As_2 molecular beams, but is hardly accessible with As_4 beams. Although the $c(4 \times 4)\alpha$ structure is energetically metastable between less *As*-rich $\beta 2(2 \times 4)$ and more *As*-rich $c(4 \times 4)\beta$, the α structure is formed under either As_2 and As_4 environment.

The structure change between $c(4 \times 4)$ and (2×4) is reversible under *As* fluxes; when the $c(4 \times 4)\beta$ surface is heated without *As* fluxes: the formation of ordered

$c(4 \times 4)\alpha$ and $\beta 2(2 \times 4)$ phases are kinetically limited. The difference in the rocking-curve shape could be ascribed to the tilted ($Ga-As$) and untilted ($As-As$) dimer geometries. In the $c(4 \times 4)\alpha$ structure, the Ga atoms of the $Ga-As$ dimer are displaced downward by a large amount of $\sim 0.8 \text{ \AA}$ to form a planar sp^2 -type bonding configuration with their As nearest neighbors: the averaged bond angle of the surface Ga atom is 119° which compares with the value expected for the ideal sp^3 arrangement. On the other hand, the surface As atoms produce p^3 -type bonds with their nearest neighbor atoms: the average bond angle is $94^\circ-98^\circ$ and is smaller than the value 109.47° expected for an ideal sp^3 arrangement. Thus, this atomic arrangement can eliminate all of unsaturated dangling bonds by transforming the As (Ga) dangling bonds into s -type fully occupied (p_z -type empty) states. Finally the $c(4 \times 4)$ surface has two types of atomic structures,

2.4. (110) surface structure

The (110) surface of a *III – V* semiconductor compound, such as *GaAs*, is more easily prepared than other semiconductor surfaces. because it is a natural cleavage plane. The (110) surface is not reconstructed and consists of planar zigzag rows of alternating group *III* and group *V* atoms along the $[\bar{1}\bar{1}0]$ direction, indicating that this cleavage plane is a non polar surface. This makes it possible to image electronic structures located far below the surface (typically up to 6 – 7 subsurface monatomic layers) without influence of the surface electronic states modulation. As a result, the imaged confined quantum states resemble the symmetry of those in the bulk. The density of states of cation and anion sublattices can be well resolved at room temperature and thus can be imaged independently of one another; in Fig. 2.9 a model of this surface is reported where the *Ga* atoms in the second layer and *As* at first layer is observed.

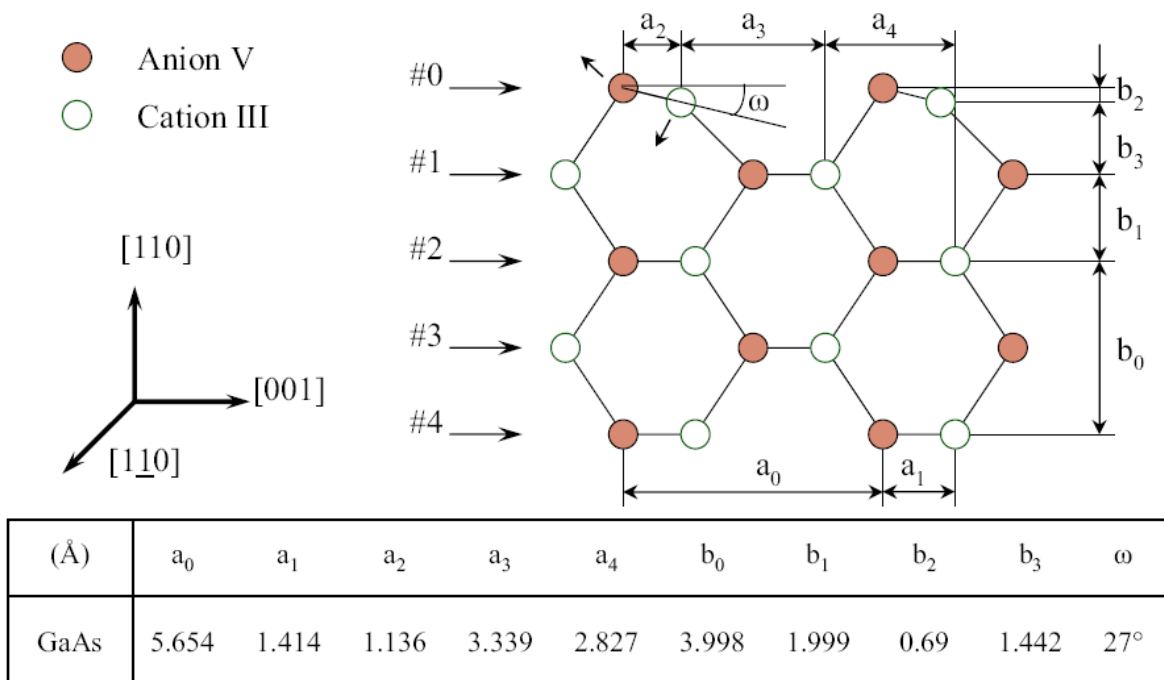


Fig.2.9. Side view on the cleaved *III – V* zinc-blende crystal. The cleavage plane has $[110]$ direction (top row of the atoms). Displacements of the surface atoms with respect to their original positions in the bulk are marked by the arrows.

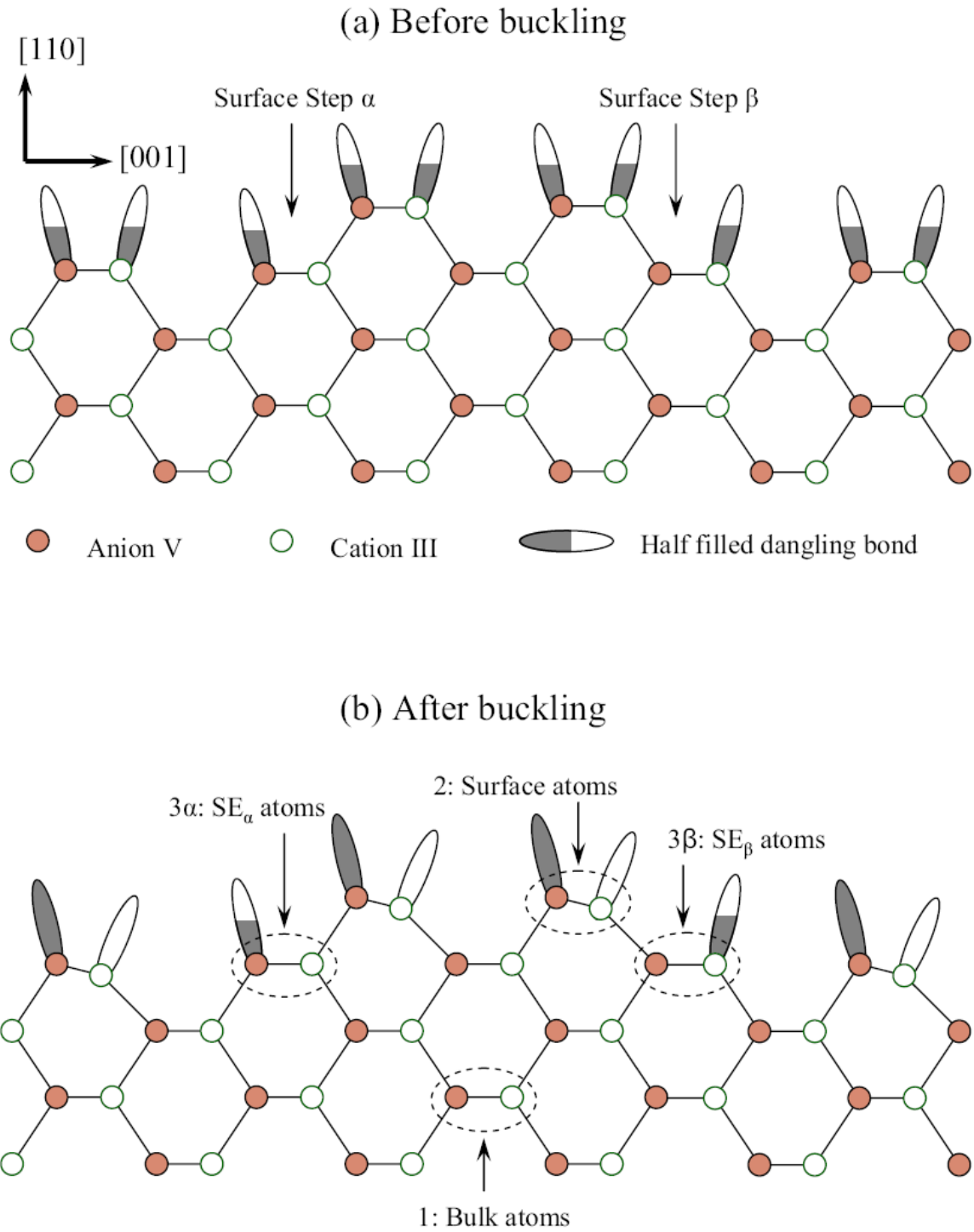


Fig.2.10. Schematic representation of the anion and cation surface states and their filling on the cleavage induced $\{110\}$ surfaces and step-edges (SE): (a) before buckling; (b) after buckling.

Even though the (110) is not reconstructed, this surface presents a relaxation (buckling). The buckling originates from the different preferential bonding configuration of the cations (group *III* element) and anions (group *V* element). The surface As anions have sp^3 – configuration consisting of four bonds arranged nearly tetrahedrally in space, similar to the arrangement of the As bonds in the bulk. The sp^3 – configuration of a cation (in our case Ga), however, is unstable. Instead, it prefers sp^2 – configuration with all three bonds to nearest As atoms laying in the same plane and one additional empty out-of-plane dangling bond. In order to minimize the energy and reach the stable configuration the surface atoms relax as shown in Fig. 2.4. As a result, the anion is relaxed outwards while the cation is moved inwards. This relaxation can be described by a single parameter, the buckling angle ω . The buckling angle is believed to be about 27° and cannot be directly measured by the **STM**, since the surface image depends on the electronic surface state density that varies with energy. The displacement of surface atoms along the [001] direction may extinguish reflection symmetry with respect to the $[1\bar{1}0]$ axis of the features observed on the (110) surface. The relaxation drives the surface states out of the bulk energy-gap and results in the formation of so-called dangling bonds that constitute most of the surface states. This process is schematically described in Fig. 2.10. Dangling bonds of anions and cations are well separated in energy by the band gap. This makes possible to image, at low sample bias, selectively only anion or cation sublattices. The cation bonds (so called C_3 states) are empty and located in the region of the conduction-band bottom. The anion bonds (A_5) are filled and reside in the region of the valence band top. Their position may shift with respect to the bulk bands and narrow the surface band-gap depending on their population. Ebert *et al.* [44] showed in their experiments and calculations that the dangling bond picture is too simple to explain the **STM** results. For the complete description, the surface resonances have also to be considered. The appearance of surface states strongly depends on their energy position [see, for example, Fig. 2.11]. In many cases, this greatly assists the identification and the tracing of the surface-charge distribution. The appearance of the surface states and their resolution by **STM** also depends on the symmetry properties and degree of state localization at the tip apex. In this respect special attention deserves the so-called True Lattice Resemblant Corrugation (*TLRC*) or "super resolution", when both anion

and cation atoms appear in the *STM* image. In some cases, both surface and first subsurface layers are also visible in the same image. It is believed that this happens when an atom at the tip apex establishes a chemical bond with the sample-surface atoms [34]. The appearance of *TLRC* always involves a sudden transition from the normal imaging mode to an anomalous mode with ultra high resolution. Such a resolution appears in a very narrow energy window, usually at low sample bias, when the tip is close to the sample [35, 25]. However, it varies significantly from tip to tip.

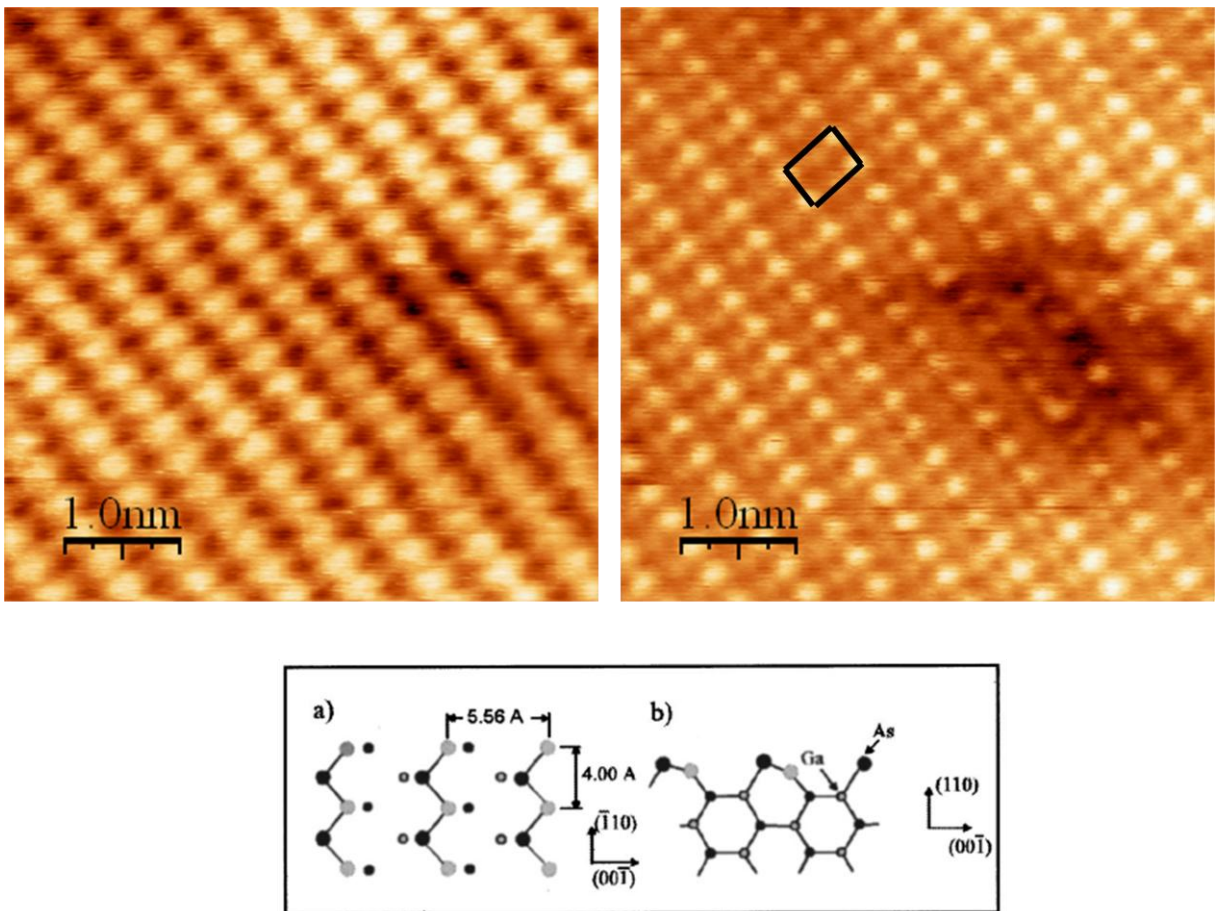


Fig. 2.11. STM images of filled (left) and empty (right) states of *GaAs*(001) and schematic representation.

References

- [1] M. D. Pashley, K. W. Haberern, W. Friday, J. M. Woodall, P. D. Kirchner, *Phys. Rev. Lett.* **60**, **2176** (1988).
- [2] D. K. Biegelsen, R.D. Bringans, J.E. Northrup, L.E.Swartz, *Phys. Rev. B* **41**, **5701** (1990).
- [3] H. Lüth *Surface and Interfaces of Solid Materials* Springer Study Edition, Springer (1995).
- [4] M. D. Pashley, *Phys. Rev. B* **40**, **10481** (1990).
- [5] F. Bechstedt *Principles of Surface Physics* Springer (2003).
- [6] W. Mönch *Semiconductor Surfaces and Interfaces* Springer (1995).
- [7] L. Däweritz, R. Hey *Surf. Sci.* **236**, **15** (1990).
- [8] Q.-K. Xue, T. Hashizume, T. Sakurai *Prog. Surf. Sci.* **56**, **1** (1997).
- [9] H. H. Farrel, C.J. Palmstrøm *J. Vac. Sci. Technol. B* **8**, **903** (1990).
- [10] W. G. Schmidt, S. Mirbt, F. Bechstedt *Phys. Rev. B* **62**, **8087** (2000).
- [11] D. J. Chadi *J. Vac. Sci. Technol. A* **5**, **834** (1987).
- [12] J. E. Northrup, S. Froyen *Phys. Rev. B* **50**, **2015** (1994).
- [13] V. La Bella, M. R. Krause, Z. Dong, P. M Thibado *Surface Science Reports* **60**, **1–53** (2005).
- [14] S. B. Zhang, A. Zunger *Phys. Rev. B* **53**, **1343** (1996).
- [15] S. Mirbt, N. Moll, K. Cho, J. D. Joannopoulos *Phys. Rev. B* **60**, **13 283** (1999).
- [16] W. G. Schmidt, F. Bechstedt *Surf. Sci.* **360**, **L473** (1996).
- [17] W. G. Schmidt, F. Bechstedt *Phys. Rev. B* **54**, **16 742** (1996).
- [18] N. Moll, A. Kley, E. Pehlke, M. Scheffler *Phys. Rev. B* **54**, **8844** (1996).
- [19] Y. Garreau, M. Sauvage-Simkin, N. Jedrecy, R. Pinchaux, M. B. Veron *Phys. Rev. B* **54**, **17 638** (1996).
- [20] J. M. McCoy, U. Korte, P. A. Maksym *Surf. Sci.* **418**, **273** (1998).
- [21] V. P. LaBella, H. Yang, D. W. Bullock, P. M. Thibado, P. Kratzer, M. Scheffler *Phys. Rev. Lett.* **83**, **2989** (1999).
- [22] T. Hashizume, Q.-K. Xue, A. Ichimiya, T. Sakurai *Phys. Rev. Lett.* **73**, **2208** (1995).

- [23] T. Hashizume, Q.-K. Xue, A. Ichimiya, T. Sakurai: *Phys. Rev. B* **51**, **4200** (1995).
- [24] M. Sauvage-Simkin, R. Pinchaux, J. Massies, P. Calverie, N. Jedrecy, J. Bonnet, I. K. Robinson *Phys. Rev. Lett.* **62**, **563** (1989).
- [25] T. Hannappel, L. Toben, S. Visbeck, H. J. Crawack, C. Pettenkofer, F. Willig *Surf. Sci.* **470**, **L1** (2000).
- [26] A. Othake *Surface Science Reports* **63**, **295–327** (2008).
- [27] L. L. Chang, L. Esaki, W. E. Howard, R. Ludeke, G. Schul *J. Vac. Sci. Technol.* **10**, **11** (1973).
- [28] L. L. Chang, L. Esaki, W. E. Howard, R. Ludeke, G. Schul *J. Vac. Sci. Technol.* **10**, **655** (1973).
- [29] D. J. Chadi, C. Tanner, J. Ihm *Surf. Sci.* **120**, **L425** (1982).
- [30] P. K. Larsen, J. H. Neave, J. F. van der Veen, P. J. Dobson, B. A. Joyce *Phys. Rev. B* **27**, **4966** (1983).
- [31] M. Sauvage-Simkin, R. Pinchaux, J. Massies, P. Calverie, N. Jedrecy, J. Bonnet, I. K. Robinson *Phys. Rev. Lett.* **62**, **563** (1989).
- [32] C. Sasaoka, Y. Kato, A. Usui *Surf. Sci.* **265**, **L239** (1992).
- [33] D. K. Biegelsen, R. D. Bringans, J. E. Northrup, L.-E. Swarts *Phys. Rev. B* **41**, **5701** (1990).
- [34] A. R. Avery, D. M. Holmes, J. Sudijono, T. S. Jones, B. A. Joyce *Surf. Sci.* **323**, **91** (1995).
- [35] G. R. Bell, J. G. Belk, C. F. McConville, T. S. Jones *Phys. Rev. B* **59**, **2947** (1999).
- [36] J.E. Northrup, S. Froyen *Phys. Rev. Lett.* **71**, **2276** (1993).
- [37] A. Ohtake, J. Nakamura, S. Tsukamoto, N. Koguchi, A. Natori *Phys. Rev. Lett.* **89**, **206102** (2002).
- [38] A. Ohtake, P. Kocán, J. Nakamura, A. Natori, N. Koguchi *Phys. Rev. Lett.* **92**, **236105** (2004).
- [39] A. Nagashima, A. Nishimura, T. Kawakami, J. Yoshino *Surf. Sci.* **564**, **218** (2004).
- [40] M. Takahasi, J. Mizuki *Phys. Rev. Lett.* **96**, **055506** (2006).
- [41] C. Hogan, E. Placidi, R. Del Sole *Phys. Rev. B* **71**, **041308** (2005).
- [42] E. Penev, P. Kratzer, M. Scheffler *Phys. Rev. Lett.* **93**, **146102** (2004).

- [43] I. Kamiya, D. E. Aspnes, L. T. Florez, J. P. Harbison *Phys. Rev. B* **46**, **15894** (1992).
- [44] Ph. Ebert, B. Engels, P. Richard, K. Schroeder, S. Blügel, C. Domke, M. Heinrich, and K. Urban *Phys. Rev. Lett.* **77**, **2997** (1996).
- [45] G. J. de Raad, D. M. Bruls, P. M. Koenraad, and J. H. Wolter *Phys. Rev. B* **64**, **075314** (2001).
- [46] G. J. de Raad, in *Voltage-dependent Scanning Tunneling Microscopy on the {110}-surfaces of GaAs, AlGaAs and their heterostructures*, Eindhoven University of Technology, The Netherlands, 2001.

Chapter 3

Dilute Magnetic Semiconductor: $Ga_{1-x}Mn_xAs$

3.1. Overview

Dilute magnetic semiconductors (*DMS*) consist of standard semiconductors in which some lattice atoms are randomly substituted by a magnetic atom, thus inserting local magnetic moments in the semiconductor matrix (see fig. 3.1).



Fig. 3.1. Schematic representation of a) non-magnetic semiconductors and b) diluted magnetic semiconductors.

These magnetic moments can originate from $3d$ or $4f$ open shells of transition metals, like Mn , or rare-earth elements. *DMS* can exhibit a wide range of magnetic properties, from paramagnetism and spin-glass behavior to ferromagnetism. They can span the range from highly insulating to metallic, even in the same alloy system. The *III – V* semiconductors with a sizable concentration of magnetic elements had not been obtained until the 1990's due to the low solubility of transition metals in *III – V* materials (less than 10^{18} cm^{-3}). The use of non-equilibrium growth, primarily by molecular beam epitaxy (*MBE*) at relatively low temperatures, made it possible to grow *III – V DMS* such as $In_{1-x}Mn_xAs$ [1, 2] and $Ga_{1-x}Mn_xAs$ [3, 4] with a considerably higher concentration of magnetic atoms.

3.2. Structural properties

In the $(Ga, Mn)As$ compound Mn provides both localized spins and carriers (holes) due to its acceptor nature. A schematic phase diagram of **MBE** growth is depicted in Fig. 3.2. Clear **RHEED** oscillations are observed at the initial growth stage (even without Mn), which indicate the growth mode to be two dimensional [5, 6]. This phase diagram shows the tendencies of physical properties vs. growth parameters; however recently it is possible to grow metallic films with Mn contents of at least $x = 0.08$ [see Chapter 1]. When T_s is lowered, more compensating defects (Section 3.5) come into play and the $Ga_{1-x}Mn_xAs$ layers are insulating. At even lower growth temperatures roughening of the sample occurs, and eventually the $Ga_{1-x}Mn_xAs$ films become polycrystalline. When the growth temperature is too high, segregation of $MnAs$ clusters occurs at the sample surface, thus inhibiting the incorporation of Mn in the semiconductor matrix. Metallic $Ga_{1-x}Mn_xAs$ films are ferromagnetic, while the highest Curie temperatures are found for samples with the lowest resistivity. Ferromagnetism can even be observed in insulating samples [8, 9].

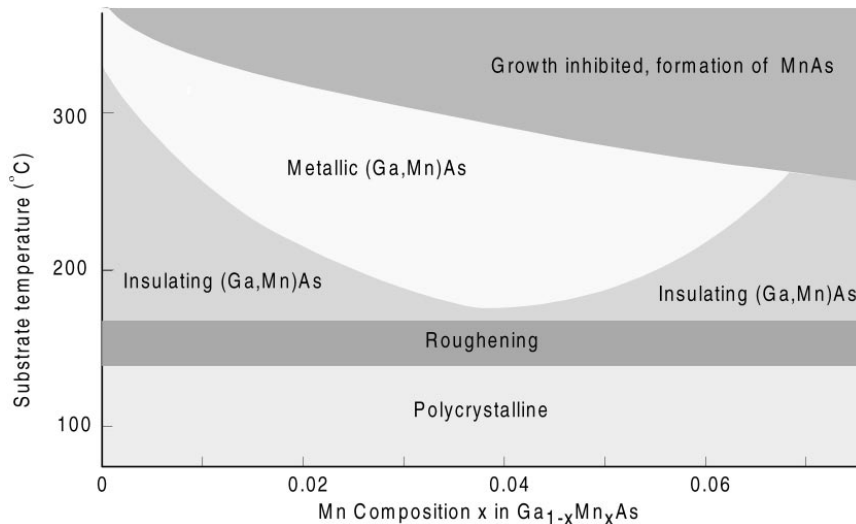


Fig. 3.2. Schematic phase diagram showing the relation between growth parameters (substrate temperature and Mn concentration) and the properties of $(Ga, Mn)As$ grown by **MBE** [7].

Normally, either a $GaAs$ buffer layer or a $In_{1-x}Mn_xAs$ buffer layer is grown before growth of $Ga_{1-x}Mn_xAs$. $GaAs$ is grown at low temperatures (LT) and has the same crystal structure, except that $LT - GaAs$ layers typically contain up to 2% excess As , which results in a lattice expansion of the order of 0.1%. As mentioned earlier, the amount of point defects in these LT layers depends on the growth temperature, and consequently this holds as well as for the lattice parameters.

The $Ga_{1-x}Mn_xAs$ growth can be started by simply commencing the Mn beam during the low-temperature $GaAs$ growth and keeping substrate temperature (T_s) constant at 250° and ideally all Mn atoms randomly substitute Ga atoms (Mn_{Ga}) in the zinc blend structure of $GaAs$. Although the properties of grown $Ga_{1-x}Mn_xAs$ do depend on growth parameters such as As overpressure and T_s [10, 11], as long as the established growth procedure is followed, the properties of $Ga_{1-x}Mn_xAs$ films are reproducible; for example, for a given Mn concentration x , the ferromagnetic transition temperature T_c can always be maintained in the range of $2000x \pm 10 K$. The surface reconstruction of $Ga_{1-x}Mn_xAs$ is (1×2) during and after growth. When the Mn flux or the substrate temperature or both are too high, a **RHEED** pattern indicative of the appearance of the $MnAs$ ($NiAs$ –structure) second phase on the surface emerges. Maximum x so far obtained is about 0.07, above which surface segregation occurs even at low-growth temperature. The lattice constant a of $GaMnAs$ is larger than that of $GaAs$ ($a_{GaAs} = 5.65325 \text{ \AA}$) and increases with increasing Mn content [7]. Since $Ga_{1-x}Mn_xAs$ grows pseudomorphic on $GaAs$ [12, 13, 14], the $Ga_{1-x}Mn_xAs$ layer is under compressive biaxial strain with $\epsilon_{xx} = \epsilon_{yy} = (a_{GaAs} - a)/a$ of the order of minus a few tenths of a percent. Due to dependency on the Mn concentration one might expect that the $Ga_{1-x}Mn_xAs$ lattice constant follows Vegard's law, which states a linear relationship between the concentration of the substitute element and the size of the lattice parameters:

$$a = (1 - x)a_{GaAs} + xa_{MnAs} \quad [3.1]$$

where a_{MnAs} is the lattice parameters of the hypothetical zinc-blende $MnAs$. This increase of a proportionally to x occurs because $Ga_{1-x}Mn_xAs$ has an intrinsic lattice constant that is larger than that of $GaAs$. However, the lattice constant of $Ga_{1-x}Mn_xAs$ at a given Mn content, and therefore as well lattice constant for the hypothetical $MnAs$ zinc-blende phase, strongly depend on the growth conditions. Moreover, using density-functional theory (*DFT*)

calculations Mašek *et al.* [15] have predicted that increase in lattice constant due to substitutional Mn_{Ga} is minimal, and that the increase in a is mainly induced by the As_{Ga} and Mn_I point defects (see Section 3.5). They found that the lattice constant is given by:

$$a(x_S, x_A, x_I) = a_{GaAs} + 0.02x_S + 0.69x_A + 1.05x_I \text{ (\AA)} \quad [3.2]$$

where x_S, x_A and x_I denote the Mn_{Ga}, As_{Ga} and Mn_I concentrations, respectively. On the assumption that concentrations of both As_{Ga} and Mn_I defects are correlated with the Mn content, or with the (optimal) growth temperature, eq. [3.2] can be used to explain the apparent Vegard's law behavior.

3.3. Electronic properties

$GaAs$ is a direct band gap semiconductor with an energy gap $E_g = 1.42 \text{ eV}$ at $300K$. When magnetic impurities like Mn are incorporated in a semiconductor their magnetic and transport properties will depend on the positions of the energy levels corresponding to the magnetic levels with respect to the energy bands of the host semiconductor. Together with the on-site correlation energy U , this position of the Mn energy levels will determine the charge and spin state of the Mn atom, and whether it will act as a dopant. Isolated Mn atoms have $(Ar)3d^54s^2$ electron configuration, and when these atoms are incorporated in a $III - V$ semiconductor, they are expected to substitute the trivalent cation. As the Mn atom has only two valence electrons, the formation of a hole is expected and at this substitutional position there are three possible electronic ground states for the Mn impurity: $A^0(d^4)$, $A^0(d^5 + h)$ (a complex configuration with hole (h) weakly bound to the Mn ion) and $A^-(d^5)$ [16]. Here, A^0 denotes the state in which the Mn center is neutral with respect to the $GaAs$ background and thus corresponds to a Mn^{3+} state, while A^{2-} is the "negatively charged" Mn^{2+} center. The notation in brackets is the electronic configuration of the d electrons. In case of $A^0(d^4)$, the hole resides in the Mn $3d$ shell. In $GaAs$ doped with Mn the $A^0(d^4)$, configuration is not observed [17], as due to a strong intra-site Hund coupling a state with five d electrons is energetically more favorable, as is the case for $A^0(d^5 + h)$ and $A^-(d^5)$. In accordance to that, photoemission measurements in $Ga_{1-x}Mn_xAs$ [18] reveal an energy level deep ($\sim 2.7 \text{ eV}$) below the

valence band edge which can be attributed to the $Mn d^4/d^5$ acceptor state [19], i.e. the transformation of the triply ionized ions Mn^{3+} into Mn^{2+} . As the acceptor state lies under the top of the valence band, the ground state corresponds to the $Mn d^5$ state. When an $A^0(d^4)$, traps an electron tightly in the $3d$ shell forming the high spin, $S = 5/2$, $3d^5$ configuration, it is negatively charged in respect to the $GaAs$ background and can therefore bind the hole in a effective mass acceptor state $A^0(d^5 + h)$. The energy of this hydrogen-like state will then be found just above the valence band, where the binding energy of the hole corresponds to the ionization energy of the acceptor. In the low doping range Mn ions are indeed found to be acceptors with an ionization energy of $112 meV$ [20, 21]. In Fig. 3.3 it is described, from reference [17, 22], the presence of the change of energy gap in the $GaMnAs$ respect to $GaAs$ with **STS** technique. Various experimental results indicate that the ground state of the Mn impurity at low doping concentrations corresponds to the $A^0(d^5 + h)$ configuration [16]. Photoemission experiments show that the itinerant holes originating from the Mn acceptor level mainly have an $As 4p$ –character, and can thus be associated with the host semiconductor valence band [23].

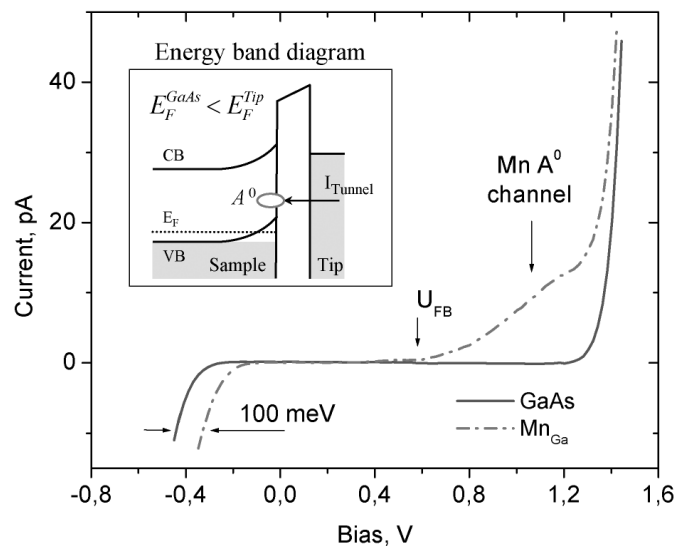


Fig. 3.3. $I(V)$ curves acquired on the clean $GaAs$ surface (solid line) and in the middle of the cross like feature (dashed line) with $3 \cdot 10^{18} cm^{-3}$ Mn doping level. The simulated position of the flat-band potential U_{FB} is indicated by the labeled arrow. Inset displays energy band diagram for the positive sample bias [22].

When the Mn concentration is increased the acceptor states will start to overlap and the energy level will broaden and form an impurity band. At high Mn content this impurity band will merge with the $GaAs$ valence band, leading to the insulator-to-metal transition as holes are induced in the valence band that can be considered as itinerant. In this case the ground state of some of the Mn atoms will be $A^-(d^5)$, where the hole resides in the valence band and the Mn ion is in the $3d^5$ ($S = 5/2$) configuration. This configuration will also be favored due to the high hole concentrations in the typical doping range of $Ga_{1-x}Mn_xAs$, which may lead to screening of the Coulomb potentials of the A^- centers, resulting in a lower ionization energy of the holes [16].

3.4. Magnetic properties

Sharp, square hysteresis loops, indicating a well-ordered ferromagnetic structure, have been measured in the magnetization (M) versus magnetic field (B) curves with B applied in the plane of the film measured for several Mn concentrations [24]. Below $x = 0.005$ no ferromagnetism was detected. The low-temperature saturation magnetization, M_S , of the $(Ga, Mn)As$ film is given by $M_{Mn} = N_{Mn}g\mu_B S_{Mn}$, where N_{Mn} is the nominal Mn concentration, $g = 2$ the g^2 factor of Mn , μ_B is the Bohr magneton, and S_{Mn} the spin of Mn . The possible values for S_{Mn} , as we saw before, are $5/2$ for Mn^{2+} and $4/2$ for Mn^{3+} . The measured M_S with nominal x results between the two [7]. Normally absence of remanence above T_c of $(Ga, Mn)As$ confirmed that the concentration of $MnAs$ inclusions ($T_c = 310 K$), if present, is very low. When B is applied perpendicular to the $(1\ 0\ 0)$ sample surface, an elongated magnetization curve with little hysteresis is obtained, indicating that the easy-axis for magnetization is in the plane. This occurs because $(Ga, Mn)As$ layers growth on $GaAs$ substrate are under compressive strain. Susceptibility χ of $(Ga, Mn)As$ films follows the Curie-Weiss form $\chi = C/(T - \theta)$, where C is the Curie constant and θ the paramagnetic Curie temperature. θ appears to fall close to T_c . In the absence of carriers, however, θ becomes negative ($-2 K$) indicating that the direct

² A g-factor (also called g-value or dimensionless magnetic moment) is a dimensionless quantity which characterizes the magnetic moment and gyromagnetic ratio of a particle or nucleus.

exchange among Mn is antiferromagnetic and the ferromagnetic interaction observed in these films are carrier (hole) mediated [25].

Electrical transport measurements as a function of T as well as B have proven a powerful investigation tool for $(Ga, Mn)As$ films. The dominant contribution from the anomalous Hall effect in p -type $(Ga, Mn)As$ made it possible to determine the magnetic properties from the magnetotransport measurements. The sheet Hall resistivity R_{Hall} (or the Hall resistivity ρ_{Hall}) in magnetic materials is expressed as $\rho_{Hall} = R_{Hall}d = R_0B + R_S M$ where R_0 is the ordinary (normal) Hall coefficient, R_S the anomalous Hall coefficient, d the sample thickness, and M the magnetization of the sample. Separate measurements showed that R_S is proportional to R_{sheet} , indicating that the skew scattering is responsible for the anomalous term [26], and thus $R_S/d = cR_{sheet}$ where c is a temperature-independent constant. Because of the high-hole concentration, the anomalous Hall term is the dominant term even up to room temperature. This allows one to determine M of the sample from R_{Hall} ($M \sim (1/c) R_{Hall} / R_{sheet}$). Fig. 3.4 shows the temperature dependence of R_{sheet} of six 200 nm thick $(Ga, Mn)As$ epitaxial films grown on $(Al_{0.9}Ga_{0.1})As$ buffer layer [7]. The temperature dependence of R_{sheet} of samples with intermediate Mn composition (x from 0.035 to 0.053) shows that they are on the metal side of the metal-insulator transition whereas low and high x samples are on the insulator side.

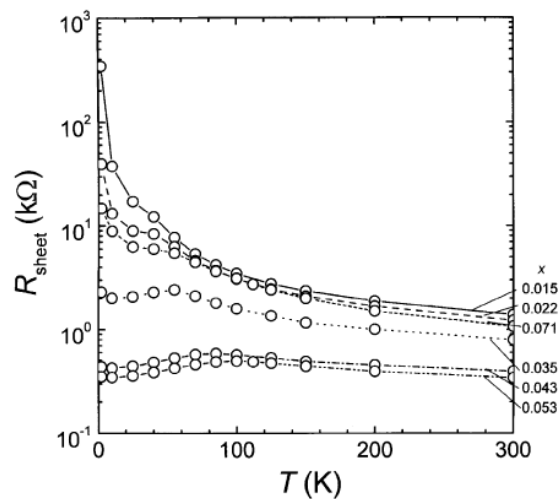


Fig. 3.4. Temperature dependence of sheet resistivity R_{sheet} of $(Ga, Mn)As$ thin films grown on $(Al_{0.9}Ga_{0.1})As$ buffer layers. Samples with intermediate composition (0.035 – 0.053) are metallic [7].

At T_c , all samples show a hump in $R_{sheet} - T$ curves, which is most pronounced in metallic samples. This anomalous temperature dependence is most probably due to the critical scattering, in which carriers are scattered by magnetic fluctuation through exchange interaction.

Several models have been put forward to explain the origin of ferromagnetism in $GaMnAs$. In principle various mechanisms for the hole mediated exchange coupling in $Ga_{1-x}Mn_xAs$ are possible like *double exchange*, *Zener mechanism*, *RKKY interaction*. For further information about these mechanism see ref. [27, 28, 29]. A brief discussion of these models is reported below. Numerous experimental results indicate that the ferromagnetic interaction in dilute magnetic semiconductors is mediated by the charge carriers, which are in most cases valence band holes. The antiferromagnetic superexchange in these samples can be overcompensated by ferromagnetic interactions mediated by band holes. The magnetic interaction among Mn has been shown to be antiferromagnetic in n -type $In_{1-x}Mn_xAs$ [30] and in fully carrier compensated $Ga_{1-x}Mn_xAs$ using Sn as a donor [31], indicating the critical role of the holes for the magnetic coupling. The hole mediated origin of the ferromagnetism in $Ga_{1-x}Mn_xAs$ is further evidenced by the correlation between its transport and magnetic properties. The ferromagnetic properties of diluted magnetic semiconductors result from the presence of a spin-dependent interaction between the electrons or holes in the sp bands of the semiconductor host and electrons residing on the d shells of the magnetic impurities [32], as illustrated schematically in Fig. 3.5.

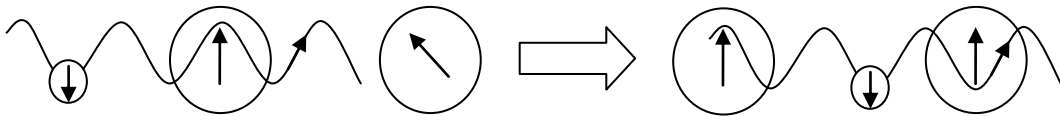


Fig. 3.5. Schematic illustration of the hole mediated exchange interaction in diluted magnetic semiconductors. A long range ferromagnetic interaction of the Mn spins results from a strong antiferromagnetic coupling of the itinerant or weakly bound holes to the localized spins.

This interaction assumes a form of the Heisenberg exchange coupling, $\mathcal{H}_{ex} = -J_{ex} \vec{s} \cdot \vec{S}$ where J_{ex} describes the strength of the interaction between the carrier spin \vec{s} and the transition-metal spin \vec{S} . If J_{ex} is positive the lowest energy state corresponds to a parallel spin alignment, while an antiferromagnetic alignment is favored when J_{ex} is negative. In

$Ga_{1-x}Mn_xAs$, the hybridization of the valence band holes (with p –orbital character) and the Mn d states that results in spin-dependent interaction, the so called kinetic exchange, which is characterized by a rather large exchange energy $J_{pd} = -1$ eV [32]. The negative sign of J_{pd} reflects an antiferromagnetic coupling between the hole spin and the localized Mn spin. These $sp - d$ exchange couplings give rise to a spin-splitting of the bands proportional to the sample magnetization. The antiferromagnetic coupling between the hole spin and the localized Mn spin leads to a long range ferromagnetic coupling between neighboring Mn spins (see fig. 3.5), which eventually results in a ferromagnetic state at low temperatures.

3.5. Defects

Although there is some lattice mismatch between the $Ga_{1-x}Mn_xAs$ layer and the $GaAs$ substrate, $Ga_{1-x}Mn_xAs$ can be grown pseudomorphically (fully strained), so no dislocations are formed at the interface. However due to the low temperatures which are required to grow $Ga_{1-x}Mn_xAs$ (see fig. 3.2), point defects are inevitable and the concentration of (double) donor-like defects can be as high as 30% of the Mn content x . There are three main types of defects in $Ga_{1-x}Mn_xAs$: *As antisite*, *Mn Interstitials* and *MnAs precipitates*.

As antisites (As_{Ga}) are defects formed when As atoms occupy a Ga site in the zinc blend structure. These defects are well established in $GaAs$ layers grown by low temperature (LT) **MBE**. In the LT-regime both the surface mobility of As molecules and the As desorption rate are reduced, so that part of the excess As is non-stoichiometrically incorporated into the lattice and forms As_{Ga} as the dominant As –related defect [33, 34]. It is therefore not surprising that these defects play an important role in the electronic properties of $Ga_{1-x}Mn_xAs$. As_{Ga} act as double donors [35], and one As_{Ga} may thus compensate the holes induced by two Mn_{Ga} . As the ferromagnetism in DMS materials is hole-mediated, a reduction of the hole concentration affects both the electronic and magnetic properties of $Ga_{1-x}Mn_xAs$. The amount of As_{Ga} decreases with increasing temperature. $Ga_{1-x}Mn_xAs$ layers with low Mn content, which can be grown at higher

temperatures, should thus contain few As_{Ga} defects, whereas these defects amount to significant numbers in samples with a higher Mn content which have to be grown at lower T_S . The As_{Ga} concentration will also depend on the As overpressure, so that the amount of As_{Ga} defects can be limited by using a near stoichiometric As flux during the $Ga_{1-x}Mn_xAs$ growth, as well as a growth temperature which should be as close to the Mn segregation limit as possible. The amount of As_{Ga} can be reduced by a post-growth annealing treatment at temperatures above 400 °C [36], but this procedure is not applicable to $Ga_{1-x}Mn_xAs$ samples, as $MnAs$ precipitates are likely to form in this temperature range.

During the $Ga_{1-x}Mn_xAs$ growth Mn ions do not only occupy substitutional lattice sites, but part of the Mn dopants will also take interstitial positions in the host lattice. In $GaAs$, isolated Mn interstitials (Mn_I) are double donors [37, 38], each one compensating two Mn_{Ga} acceptors, similar to As_{Ga} defects. Mn_I are found to be the dominant defects, where as much as ~15% of the total Mn are estimated to be interstitial [39]. They could be found in tetrahedral position or octahedral position in the zinc blende structure; however the tetrahedral position are more energetically favorable. Under the non equilibrium growth conditions, Mn_I are easily formed near the surface by a simple low-energy adsorption pathway. After the subsequent As deposition the substitutional position becomes favorable with regard to the interstitial sites [38]. As a consequence, the majority of these surface Mn_I migrates to Ga sites. Since this last step requires an activation over a kinetic barrier, under non equilibrium growth conditions this conversion from Mn_I to Mn_{Ga} will not be complete and the concentration of Mn_I is expected to have a similar temperature dependence as that of As_{Ga} , namely a decreasing amount of Mn_I defects with increasing growth temperatures. The high compensating effect of Mn_I will not only reduce the conductivity, but will also weaken the hole-mediated magnetic coupling between the Mn spins and therefore lower the Curie temperature. Moreover, Mn_I tends to couple antiferromagnetically to Mn_{Ga} when they are in close vicinity through the direct exchange interaction [40, 41], thus reducing the saturation magnetization, while isolated Mn_I have no significant contribution to the ferromagnetic state. Therefore the growth temperature is a crucial parameter to control the amount of compensating defects.

As the formation of $MnAs$ is energetically more favorable than the substitutional incorporation of Mn in the $GaAs$ matrix, a $MnAs$ phase is formed at the sample surface whenever the substrate temperature exceeds the Mn segregation limit during the deposition of $Ga_{1-x}Mn_xAs$. The formation of $MnAs$ precipitates inhibits the incorporation of Mn in Mn_{Ga} positions and it is therefore undesired. Moreover, $MnAs$ clusters are metallic and thus they form a local Schottky-barrier and tend to deplete the surrounding $Ga_{1-x}Mn_xAs$ of free carrier holes. Although $MnAs$ is thermodynamically the most stable phase in the range of the typical Mn concentrations that are used in $Ga_{1-x}Mn_xAs$, the activation energy to form this phase is quite high, so it is possible to suppress the formation of $MnAs$ by keeping the substrate temperature relatively low (see Fig. 3.2).

A well known procedure to improve the quality of the $Ga_{1-x}Mn_xAs$ alloy is to subject it to a post-growth heat treatment or "annealing" at temperature below $600^\circ C$ to avoid $MnAs$ formation; this treatment enhances the conductivity σ and T_C of $Ga_{1-x}Mn_xAs$. Such effect can be attributed to an increase in hole density p which can rise by more than an order of magnitude. Annealing also increases the saturation magnetization, decreases the coercive fields and induces changes in the magnetocrystalline anisotropy of the $Ga_{1-x}Mn_xAs$ layers. A reduction of the lattice constant is also observed upon annealing indicating that the changes induced by annealing are induced through the removal of point defects like interstitial Mn [42].

3.6. $GaMnAs(001)$ and $Mn/GaAs(001)$ surfaces.

During and after **MBE** growth $GaMnAs(001)$ exhibits an asymmetry (1×2) reconstruction. Contrarily to the well defined arrangements of $MnAs$ atoms at the surface [43-46] after deposition on $GaAs(001)$ substrate, the structure of $GaMnAs(001)$ surface is still unidentified and, due to a high disordering that explains the asymmetry, no data in literature are present. In this work an initial step of this surface study will be shown.

The thermodynamic stability of $Mn/GaAs$ and the reaction phase sequence resulting from the interfacial interactions are not well known. As the initial stage of interface formation, the chemisorption of Mn on the semiconductor surface is of high importance to

understand the properties of the interface. There are significant works concerning the *Mn* deposition on the cleaved *GaAs* surface (110) [47-50], but few literature of *Mn* on *GaAs*(001) surface is available [51-53]. For this reason it could be very important to perform measurement on the *GaAs*(001) surface and compare the results with the *GaMnAs* growth in order to obtain more information on the growth mechanism; this study improves the knowledge of electronic and structural properties which are strongly correlated, as said above, with magnetic properties that are the crucial point of this compounds for industrial usage.

References.

- [1] H. Munekata, H. Ohno, S. von Molnár, A. Segmüller, L. L. Chang, and L. Esaki *Phys. Rev. Lett.* **63**, 1849 (1989).
- [2] H. Ohno, H. Munekata, T. Penney, S. von Molnár, and L. L. Chang *Phys. Rev. Lett.* **68**, 2664 (1992).
- [3] J. De Boeck, R. Oesterholt, A. Van Esch, H. Bender, C. Bruynseraede, C. Van Hoof, and G. Borghs *Appl. Phys. Lett.* **68**, 2744 (1996).
- [4] H. Ohno, A. Shen, F. Matsukura, A. Oiwa, A. Endo, S. Katsumoto, and Y. Iye *Appl. Phys. Lett.* **69**, 363 (1996).
- [5] A. Shen, H. Ohno, F. Matsukura, Y. Sugawara, N. Akiba, T. Kuroiwa, A. Oiwa, A. Endo, S. Katsumoto, Y. Iye *J. Crystal Growth* **175-176**, 1069 (1997).
- [6] A. Shen, Y. Horikoshi, H. Ohno, S.P. Guo *Appl. Phys. Lett.* **71**, 1540 (1997).
- [7] Hideo Ohno *J. Magn. Magn. Mat.* **200**, 110-129 (1999).
- [8] F. Matsukura, H. Ohno, A. Shen, and Y. Sugawara *Phys. Rev. B* **57**, R2037 (1998).
- [9] Oiwa, S. Katsumoto, A. Endo, M. Hirasawa, Y. Iye, H. Ohno, F. Matsukura, A. Shen, and Y. Sugawara *Solid State Comm.* **103**, 209 (1997).
- [10] F. Matsukura, A. Shen, Y. Sugawara, T. Omiya, Y. Ohno, H. Ohno presented at the *25th International Symposium on Compound Semiconductors*, 12-16 October 1998, Nara, Japan.
- [11] H. Shimizu, T. Hayashi, T. Nishinaga, M. Tanaka *Appl. Phys. Lett.* **74** 398 (1999).
- [12] I.Kuryliszyn-Kudelska, J.Z.Domagala, T.Wojtowicz, X.Liu, E. Lusakowska, W.Dobrowolski, and J.K.Furdyna *J. Appl. Phys.* **95**, 603 (2004).
- [13] A. Shen, F. Matsukura, S. P. Guo, Y. Sugawara, H. Ohno, M. Tani, H. Abe, and H. C. Liu *J. Cryst. Growth* **201-202**, 673 (1999).
- [14] J. Sadowski, J. Z. Domagala, J. Bąk-Misiuk, S. Koleńnik, M. Sawicki, K. áwiętek, J. Kanski, L. Ilver, and V. Ström *J. Vac. Sci. Technol. B* **18**, 1697 (2000).
- [15] J. Mašek, J. Kudrnovský, and F. Máca *Phys. Rev. B* **67**, 153203 (2003).
- [16] F. Matsukura, H. Ohno, and T. Dietl in *Handbook on Magnetic Materials*, vol. **14**, edited by K. H. J. Buschow (Elsevier, Amsterdam, 2002), pp. 1-87.

- [17] A. M. Yakunin, A. Yu. Silov, P. M. Koenraad, W. VanRoy , J. De Boeck, J. H. Wolter *Physica E* **21** 947–950 (2004).
- [18] J. Okabayashi, A. Kimura, O. Rader, T. Mizokawa, A. Fujimori, T. Hayashi, and M. Tanaka *Phys. Rev. B* **58**, R4211 (1998).
- [19] T. Dietl *Semicond. Sci. Technol.* **17**, 377 (2002).
- [20] O. Madelung (ed.) *Semiconductors : group IV elements and III-V compounds* (Data in Science and Technology: Springer-Verlag, Berlin, 1991).
- [21] M. Linnarsson, E. Janzén, B. Monemar, M. Kleverman, and A. Thilderkvist *Phys. Rev. B* **55**, 6983 (1997).
- [22] A. M. Yakunin, A. Yu. Silov, P. M. Koenraad, J. H. Wolter, W. Van Roy, J. De Boeck, J.-M. Tang, and M. E. Flattè *Phys. Rev. Lett.* **92**, 216806-1 (2004).
- [23] J. Okabayashi, A. Kimura, O. Rader, T. Mizokawa, A. Fujimori, T. Hayashi, and M. Tanaka *Phys. Rev. B* **64**, 125304 (2001).
- [24] H. Ohno, A. Shen, F. Matsukura, A. Oiwa, A. Endo, S. Katsumoto, Y. Iye *Appl. Phys. Lett.* **69** 363 (1996).
- [25] Y. Satoh, N. Inoue, Y. Nishikawa, J. Yoshino *Third Symposium on Physics and Application of Spin Related Phenomena in Semiconductors*, 17-18 Nov. 1997, Sendai, Japan, p. 23.
- [26] C.L. Chien, C.R. Westgate (Eds.) *The Hall Effect and Its Applications*, Plenum, New York, 1980.
- [27] T. Dietl, H. Ohno, F. Matsukura, J. Cibert, D. Ferrand *Science* **287** 1019 (2000).
- [28] T. Jungwirth, Jairo Sinova, J. Měšek, J. Kučera, A.H. MacDonald *Rev. Mod. Phys.* **78**, 809 (2006).
- [29] Mathieu Malfait PhD thesis *Magnetic and transport properties of $Ga_{1-x}Mn_xAs$ diluted magnetic semiconductors* (2006).
- [30] S. von Molnár, H. Munekata, H. Ohno, and L. L. Chang *J. Magn. Magn. Mat.* **93**, 356 (1991).
- [31] Y. Satoh, D. Okazawa, A. Nagashima, and J. Yoshino *Physica E* **10**, 196 (2001).
- [32] T. Dietl and H. Ohno *MRS Bull.* 28, 714 (2003).

- [33] M. Kaminska, Z. Liliental-Weber, E. R. Weber, T. George, J. B. Kortright, F. W. Smith, B.-Y. Tsaur, and A. R. Calawa *Appl. Phys. Lett.* **54**, **1881** (1989).
- [34] R.M. Cohen *Mat. Sci. Eng.* **R 20**, **167** (1997).
- [35] S. Sanvito, G. Theurich, and N. Hill *J. Supercond.* **15**, **85** (2002).
- [36] R.C. Lutz, P. Specht, R. Zhao, O.H. Lam, F. Börner, J. Gebauer, R. Krause Rehberg, and E.R. Weber *Physica B* **273**, **722** (1999).
- [37] F. Mäca and J. Mäek *Phys. Rev. B* **65**, **235209** (2002).
- [38] S. C. Erwin and A. G. Petukhov *Phys. Rev. Lett.* **89**, **227201** (2002).
- [39] K. M. Yu, W. Walukiewicz, T. Wojtowicz, I. Kuryliszyn, X. Liu, Y. Sasaki, and J. K. Furdyna *Phys. Rev. B* **65**, **201303** (2002).
- [40] J. Blinowski and P. Kacman *Phys. Rev. B* **67**, **121204** (2003).
- [41] D. J. Priour, E. H. Hwang, and S. Das Sarma *Phys. Rev. Lett.* **92**, **117201** (2004).
- [42] K. W. Edmonds, P. Bogusławski, K. Y. Wang, R. P. Campion, S. N. Novikov, N. R. S. Farley, B. L. Gallagher, C. T. Foxon, M. Sawicki, T. Dietl, M. Bongiorno Nardelli, and J. Bernholc *Phys. Rev. Lett.* **92**, **037201** (2004).
- [43] M. Kästner, C. Herrmann, L. Däeritz, and K. H. Ploog *J. Appl. Phys.* **92**, **5711** (2002).
- [44] M. Kästner, F. Schippan, P. Schützendübe, L. Däweritz, K.H. Ploog *Surf. Sci.* **460**, **144–152** (2000).
- [45] F. Schippan, M. M. Kästner, L. Däweritz, and K. H. Ploog *Appl. Phys. Lett.* **76**, **834** (2000)
- [46] M. Kästner, F. Schippan, P. Schützendübe, L. Däweritz, and K. Ploog *J. Vac. Sci. Technol. B* **18(4)**, **2052** (2000).
- [47] J. X. Cao, X. G. Gong, and R. Q. Wu *Phys. Rev. B* **72**, **153410** (2005).
- [48] Fu Huaxiang, Ye Ling, Zhang Kaiming, Xie Xide *Surf. Sci.* **341**, **273-281** (1995).
- [49] C. Hughes, R. Ludeke, F. Schaffler, and D Rieger *J. Vac. Sci. Technol. B* **4**, **924** (1986).
- [50] D. Kitchen, A. Richardella, J.-M. Tang, M. E. Flattè and A. Yazdani *Nature* **442**, **436** (2006).

- [51] Y. Osafune, G. S. Song, J. I. Hwang, Y. Ishida, M. Kobayashi, K. Ebata, Y. Ooki, and A. Fujimori *arXiv:0711.3257v2 [cond-mat.mtrl-sci]* (2008)
- [52] J. L. Hilton, B. D. Schultz, S. McKernan, and C. J. Palmstrøm *Appl. Phys. Lett.* **84**, **3145** (2004).
- [53] X. Jin, Y. Chen, G. S. Dong, M. Zhang, M. Xu, X. G. Zhu, and Xun Wang E. D. Lu, H. B. Pan, P. S. Xu, and X. Y. Zhang, and C. Y. Fan *Phys. Rev. B* **51**, **9702-9706** (1995).

Chapter 4

Experimental Techniques

4.1. Overview.

In this Chapter all techniques used to grow and characterize the *GaMnAs* and *Mn/GaAs(001)* surfaces will be illustrated. In the first part the epitaxial growth technique will be explained; in the second part attention will be focused on electronic (***Photoelectron Spectroscopy, Reflection Anisotropy Spectroscopy, Electron Energy Loss Spectroscopy***) and morphological (***Scanning Tunneling Microscopy and Photoelectron Diffraction***) methods.

4.2. Molecular Beam Epitaxy (*MBE*).

Molecular Beam Epitaxy (***MBE***) is a technique employed to grow thin and pure films of crystalline compounds [1]. In order to achieve high purity, Ultra High Vacuum (*UHV*) ($P_{tot} < 10^{-10} \text{ mbar}$) is necessary. It was first applied for growing semiconductors compounds and it is still largely used mainly because of the high technological value of such materials; in particular to the development of new devices as Quantum Dots (QDs) lasers, diodes and detectors. As shown in Fig. 4.1, molecular beams, produced by special thermal sources (Knudsen cells), impinge a crystalline substrate heated at a proper temperature.

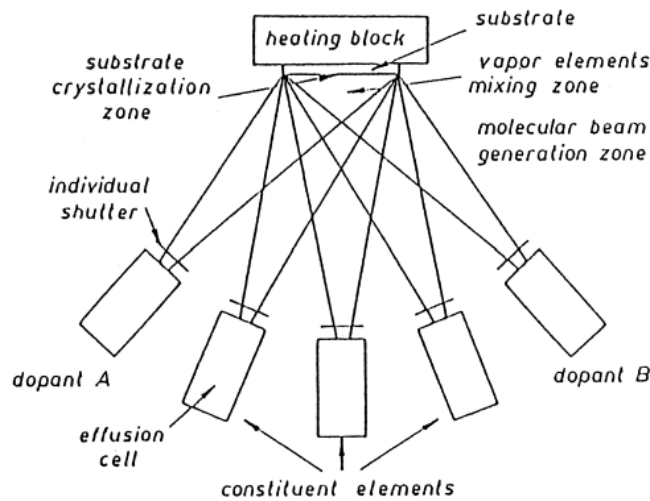


Fig. 4.1. Schematic representation of main constituents of MBE system.

Molecular beams may be considered unidirectional and their interactions negligible (molecular flux regime) in the space region between the cells and the substrate. These conditions are in opposition with the hydrodynamic regime. Each cell contains one of the element that forms the crystal, a doping element or an element used for formation of alloys; the sources are placed around the substrate in order to make the composition of the growth crystal as uniform as possible. Mechanical shutter (for growth process control) are placed in front of the effusion cells. The growth chamber is surrounded by a cryopumping system (metallic panels where liquid nitrogen flows during the growth) in order to increase the pumping speed and minimize the incorporation of contaminating gas (as H_2O , CO , CO_2) in the growth layer. During the growth the substrate rotates in a plane orthogonal to the incident beam direction in order to reach the best smoothness to the growth layer or/and the doping uniformity. The main benefits of MBE growth are:

1. low growth rate ($v \sim 1 \mu m \cdot h^{-1}$); this allows to control the variation of the chemical composition (and/or on the doping profiles) into distances in the order of atomic dimensions;
2. in comparison with other growth techniques, the growth temperature T_s is quite low, so that the interdiffusion may be neglected;
3. *UHV* allows to make use of probes for the surface quality (typically **RHEED** - **Reflection of High Energy Electron Diffraction**) of the epitaxial layer before, during and after the growth;

4. it is possible the sequential growth of several high quality alloys on the same substrate.

4.2.1. Growth of *GaAs* and *GaMnAs* with *MBE*

MBE processes occurs at non-thermodynamic equilibrium; when the shutter of an effusion cell is opened, the molecular flux (atoms and molecules) impinge on the upmost atomic layer of the crystal surface and kinetic surface processes occur like adsorption, surface migration, incorporation or thermal desorption of atoms or molecules on the crystal surface. In the case of *III – V* semiconductors it can be assumed that, in the limit of low temperatures of the substrate (T_s), every atom of the *III* group sticks to the surface, while just a portion of *V* group atoms sticks on the epitaxial layer: the atoms in excess are desorbed.

Mass spectroscopy studies on *GaAs*(111) growth [2], reveal that *Ga* atoms desorb from the surface after a finite time; contrary the As_2 dimers, without available *Ga* atoms, have a sticking coefficient $s = 0$ (the ratio between impinging atoms and incident atoms flux). From these results, it can be deduced that high quality *GaAs* films grown by *MBE* are controlled by the adsorption kinetics of *As*, while the rate is determined by *Ga* flux.

A model to explain the epitaxial growth processes on *GaAs*(001) substrate was suggested by Foxon and Joyce [3]. Because the kinetics strongly depends on *As* flux, they studied the interaction of this atoms, in the form of As_2 or As_4 (the composition depends from the effusion cell geometry), with atomic *Ga* on the *GaAs*(001) surface. The growth process for *Ga* and As_2 is the dissociative chemisorptions of As_2 molecules on single *Ga* atoms (Fig. 4.2); the As_2 sticking coefficient (≤ 1) is proportional to the *Ga* flux, J_{Ga} . The excess As_2 resublimates and the *GaAs* grows stoichiometrically.

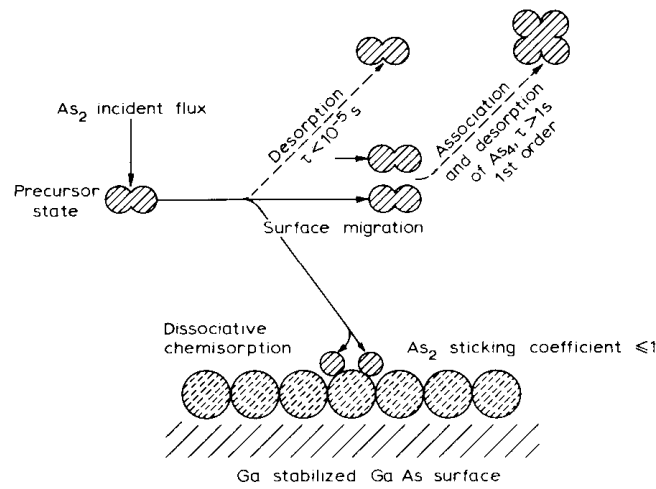


Fig. 4.2. GaAs growth from Ga and As₂.

In the case of As₄ (Fig. 4.3) molecular couples (tetramers) reacts with the adjacent Ga sites. If two As₄ molecules are close and two Ga free atoms are available, the dissociation from As₄ to two As₂ dimers is favorite; thus the maximum value of the sticking coefficient *s* is 0.5. In the condition $J_{As_4} > J_{Ga}$, there is a high probability that the As molecules occurs occupying the neighboring Ga sites, and their desorption rate is proportional to the number of provided molecules. Thus, the growth proceeds by means of As adsorption and desorption via bimolecular interactions (second order process) that results an As atom for each Ga atom.

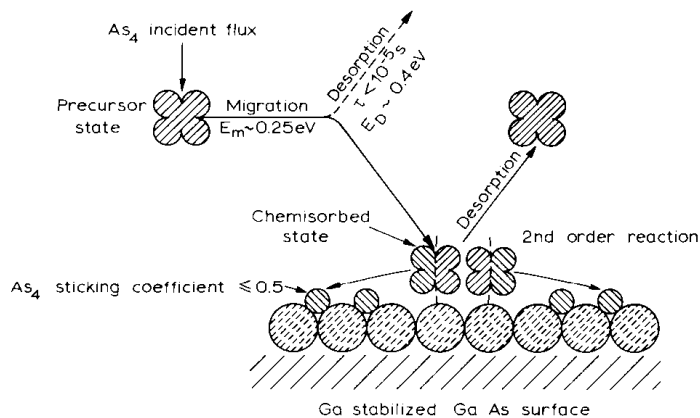


Fig. 4.3. GaAs growth from Ga and As₄.

Also the substrate temperature T_s plays an important role in the *GaAs* growth; independently of the *As* flux, when the T_s increases the desorbed amount of As_2 is greater, with a consequent increase of the surface *Ga* population. The **RHEED** analysis of the epitaxial layer evidences that for low T_s and high fluxes ratio J_{As}/J_{Ga} , the surface is *As*-reach and shows a 2×4 reconstruction, while for high T_s and low ratio J_{As}/J_{Ga} the surface is *Ga*-reach and shows a 4×2 symmetry. Thus the surface concentration of the two species depends on both the incident fluxes and on T_s .

To grow *GaMnAs* on *GaAs* substrates, after the growth of the High Temperature (HT) *GaAs* layer, the substrate is cooled down to the desired growth temperature (200 – 300°C) in *As* flux. When the substrate temperature is lowered below 480 – 520°C, the (2×4) surface reconstruction changes to $c(4 \times 4)$. When the substrate temperature is stable, a low-temperature (LT) *GaAs* buffer is grown. During the *LT – GaAs* both (1×1) and (1×2) surface reconstructions can form, depending on the growth conditions. The *Ga* flux used is the same as the *HT – GaAs* layer, but the *As* flux is significantly reduced. This lower value is possible because *As* no longer desorbs at these lower substrate temperatures. The *As* flux should be near stoichiometric to restrict the amount of *As* antisite defects, but must be large enough to avoid the formation of *Ga* droplets on the sample surface.

The growth of the *GaMnAs* thin film is similar to that of *LT – GaAs*, but with an additional *Mn* flux (Φ_{Mn}). All fluxes are first stabilized with the main shutter closed before the substrate is exposed to the beam, to ensure a fixed stoichiometry and in particular to avoid a too high *Mn* flux (the method to measure the fluxes is described in Section 4.2.3), which would degrade the surface with *MnAs* cluster formation. The *Mn* incorporation (percentage x respect to *Ga* atoms) is determined by the effusion flux during growth, and can be estimated by the ratio:

$$x = \frac{\Phi_{Mn}/\eta_{Mn}}{\Phi_{Ga}/\eta_{Ga} + \Phi_{Mn}/\eta_{Mn}} \quad [4.1]$$

where Φ_{Ga} is the *Ga* flux and η the sensitivity to the material of the vacuum gauge utilized to measure the flux. During the *GaMnAs* growth the **RHEED** pattern is more diffuse than *HT – GaAs* growth, and typically a (1×2) symmetry is observed.

4.2.2. MBE growth

The crystal quality of **MBE** growth depends on the uniformity of molecular beams striking the substrate; the latter is obtained with a isotropic distribution of the molecular flux in the solid angle between the source and the substrate and with a proper cells-substrate distance [4]. It is furthermore important that a beam generator produces high purity stable fluxes with a proper intensity. The molecular beams are usually obtained through the material annealing in the Knudsen cells (Fig. 4.4).

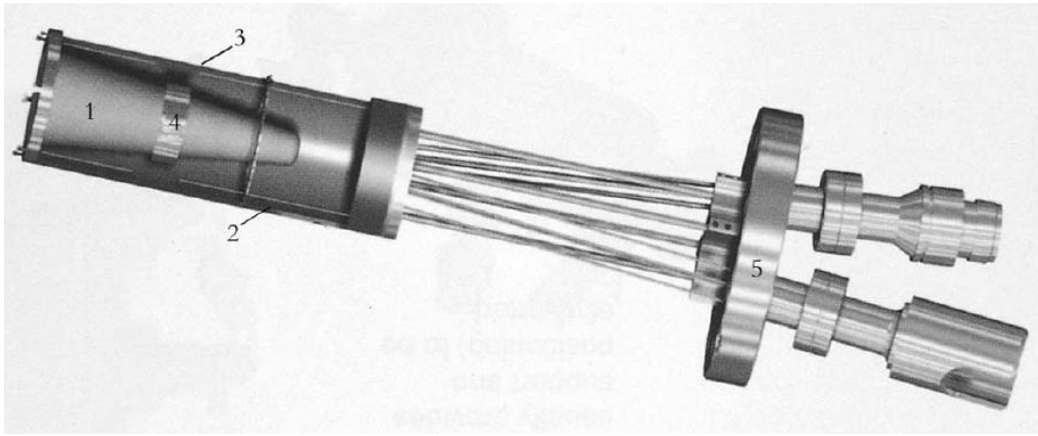


Fig. 4.4. Cutaway view of an MBE thermal effusion furnace: (1) pyrolytic BN crucible (2) resistive heater filament, (3) metal foil radiation shields, (4) wrap-around thermocouple and (5) mounting flange.

In an ideal Knudsen cell the evaporation occurs from an hollow, through a small orifice of area A , that contains the condensed phase and the vapor in equilibrium. The rate of molecules that leave the cell per time unit (the effusion rate Γ_e) is given by the Knudsen equation [1]:

$$\Gamma_e = \frac{dN_e}{dt} = A(P_{eq} - P_v) \sqrt{\frac{N_A}{2\pi M k T}} \quad [4.2]$$

where P_v is the chamber pressure, P_{eq} is the vapor pressure, N_A the Avogadro number, T the cell temperature, N_e the atoms number and M the molecular weight of the material in the cell. Considering that the $P_v \sim 10^{-10} \div 10^{-11} \text{ mbar}$ and $P_{eq} \sim 10^{-4} \div 10^{-6} \text{ mbar}$ the equation [4.2] can be simplified assuming $P_{eq} - P_v \approx P_{eq}$. A molecule m leave the effusion cell along a path identified by the angle ϑ with the normal of the orifice (A). The differential effusion rate, $d\Gamma_\vartheta$, from the opening in vacuum is proportional to the orifice area $A \cos \vartheta$

seen by m (for directions in the angle range between ϑ and $\vartheta + d\vartheta$) and to number of molecules for unit of time and surface that cross the orifice (Γ_e/A) and to the probability P

that m cross the orifice with an angle in the range between ϑ and $\vartheta + d\vartheta$.

The probability P is related to the solid angle by:

$$d\omega = \frac{dS}{r^2} = 2\pi \sin\vartheta d\vartheta. \quad [4.3]$$

The total solid angle seen by the orifice is 2π , so the probability is:

$$P = \frac{d\omega}{2\pi} = \sin\vartheta d\vartheta; \quad [4.4]$$

thus the differential effusion rate is:

$$d\Gamma_\vartheta = C_0 A \cos\vartheta \frac{\Gamma_e}{A} \sin\vartheta d\vartheta, \quad [4.5]$$

where C_0 is a proportionality constant, whose value is fixed by the condition $0 \leq \vartheta \leq \frac{\pi}{2}$ and

by the equality between the effusion rate and Γ_e :

$$\Gamma_e = \int_0^{\pi/2} d\Gamma_\vartheta = \int_0^{\pi/2} C_0 \Gamma_e \cos\vartheta \sin\vartheta d\vartheta = \frac{C_0 \Gamma_e}{2} \rightarrow C_0 = 2. \quad [4.6]$$

From [4.5] and [4.6]:

$$d\Gamma_\vartheta = \frac{\Gamma_e}{\pi} \cos\vartheta d\omega, \quad [4.7]$$

the so called *cosine emission law*.

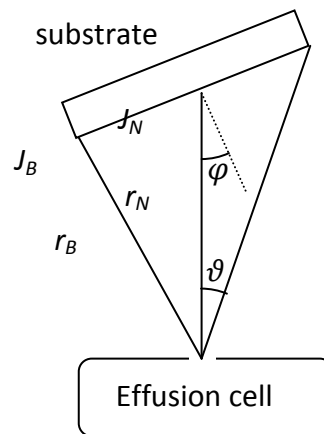


Fig. 4.5. Representation of effusion cell substrate system.

To have the molecular beam flux J at each point of the substrate, it is possible to combine equations [4.2] and [4.7]:

$$J_N = \frac{d\Gamma_{\vartheta=0}}{dS}(\varphi = 0) = \frac{\Gamma_e}{\pi r_N^2} = 1.118^{22} \frac{P_{eq} A}{r_N^2 \sqrt{MT}} \left(\frac{mol}{cm^2 sec} \right). \quad [4.8]$$

and

$$J_B = \frac{d\Gamma_{\vartheta}}{dS(\vartheta)}(\varphi = 0) = \frac{d\Gamma_{\vartheta} \cos\vartheta}{d\omega} \frac{r_N^2}{r_N^2 r_B^2} = \frac{\Gamma_e \cos^2\vartheta}{\pi r_N^2} \frac{r_N^2}{r_B^2} = J_N \cos^4\vartheta. \quad [4.9]$$

Where J_N is the flux at the center of the sample and J_B the flux at the boundaries of the sample (see Fig. 4.5). When $\varphi \neq 0$ the [4.8] and [4.9] become:

$$J_N(\varphi \neq 0) = J_N \cos\varphi; J_B(\varphi \neq 0) = J_B \frac{r_N^2}{r_B^2} \cos\vartheta \cos(\vartheta + \varphi). \quad [4.10]$$

When one considers ideal cells, the molecular flux follows a sinusoidal like function and a similar distribution is expected on the whole substrate surface. It is important to say that the distribution profile drastically changes when the material in the crucible decreases.

4.2.3 Molecular fluxes and growth rate measured by RHEED

In a real effusion cell, to have an high uniformity of the beam, the orifice is large to supply an intensive flux. With a nowadays **MBE** technology it is possible to obtain a very high smoothness on the grown layer; our **MBE** allows deposition uniformity on *GaAs* substrates with dimensions up to a 3" diameter, while in industrial chambers the limit is raised to 5". Because of the non ideality of the effusion cells, the formula 4.7 cannot be used to establish the flux on the substrate. The most diffuse method for the fluxes measurement is to use a pressure gauge mounted at the back of manipulator. The measurement of the partial pressures allows to calculate the fluxes ratio [10]:

$$\frac{J_x}{J_y} = \frac{P_x \eta_x}{P_y \eta_y} \sqrt{\frac{M_y T_x}{M_x T_y}} \quad [4.11]$$

where J_i ($i = x, y$) is the flux of the element i , P_i is the measured pressure, M_i and T_i respectively the molecular weight and temperature, and η the gauge ionization efficiency related to nitrogen given by the empirical formula (with Z atomic number):

$$\frac{\eta}{\eta_{N_2}} = 0.6 + 0.4 \frac{Z}{14} \quad [4.12]$$

To determine the **MBE** growth rate the most powerful method is the intensity variation analysis of the **RHEED** streaks [5, 6]. The growth of an **MBE** epitaxial layer is characterized by periodic intensity variations of the scattered electronic beams. This feature is due to the changes in surface roughness during the growth. In an ideal representation, at the beginning of monolayer growth the surface is very smooth and this determines an high reflectivity for the scattered beams or, in other words, the maximum condition for the **RHEED** spots intensity. The beginning of the growth leads to the random nucleation of two dimensional (*2D*) islands on the surface, with a consequent reduction of the surface reflectivity and, than, the intensity of the reflected beam. The *2D* islands growth ends with the formation of a complete monolayer (condition equivalent to the starting one). Thus one may expect a minimum for the reflectivity around 50% of surface coverage. The **RHEED** intensity shows successive maxima and minima respectively according to minimum and maximum in *2D* islands density. In Fig. 4.6 it is shown the representation of the correlation of the surface coverage with **RHEED** intensity; Fig. 4.7 show typical **RHEED** oscillations of *GaAs* growth.

The oscillatory behavior of the **RHEED** beam is universally considered a proof of the layer-by-layer growth of **MBE**; the oscillation period, the amplitude of which depends on substrate temperature, correspond with the time required to the deposition of the material equivalent to the growth of one monolayer and it allows the determination of the growth rate v .

Actually before the first monolayer has completed, new islands begins to grow on it, so starting the growth of the second monolayer. Thus one may observe that the intensity on the successive maximum is lower (due to the higher surface disorder). In the case of *GaAs*, varying J_{Ga} it is possible to change the oscillations period.

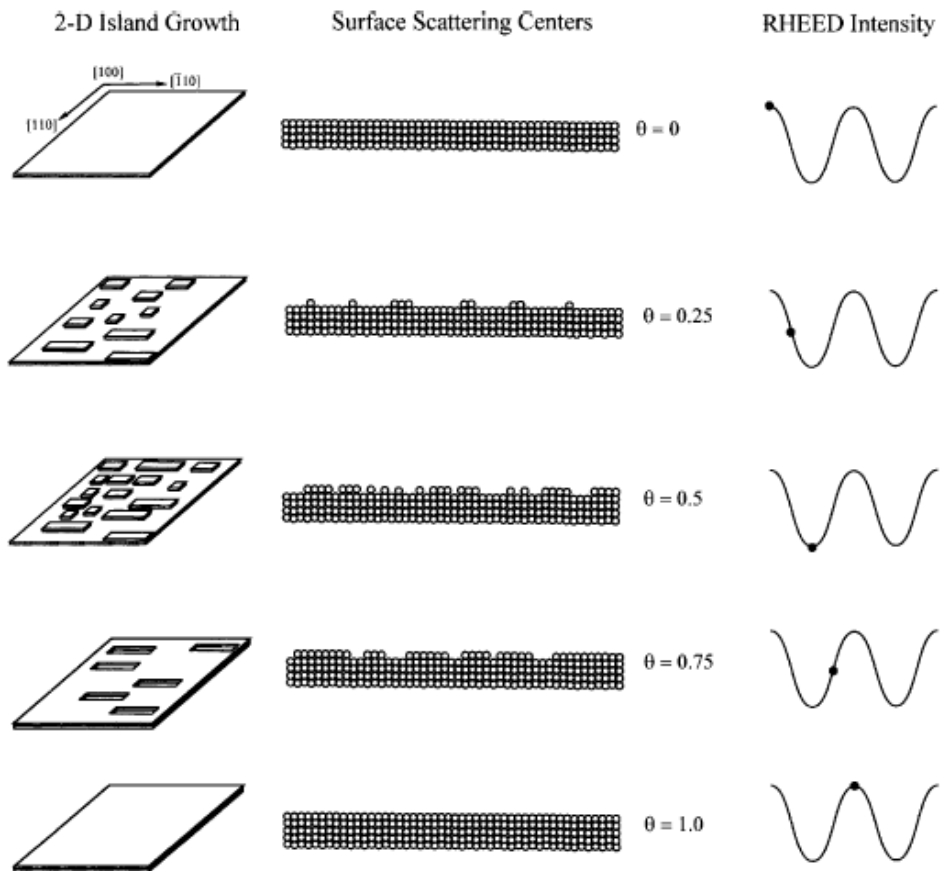


Fig. 4.6. Schematic diagram of the correlation of surface coverage of 2-D clusters with idealized RHEED oscillations.

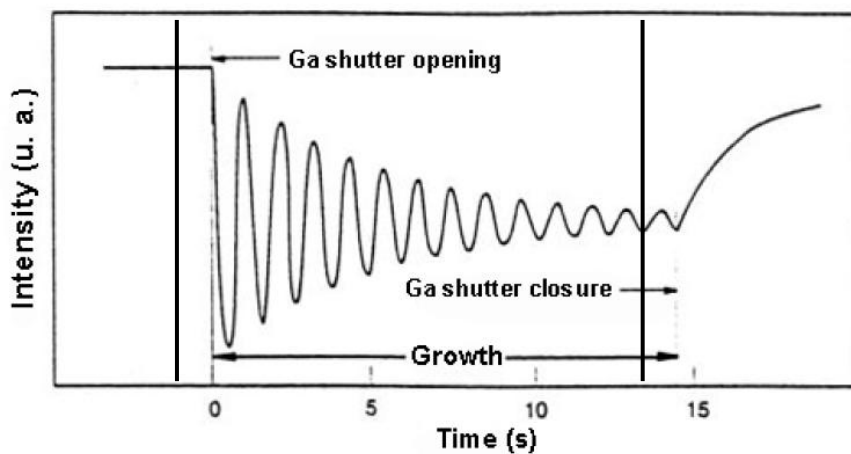


Fig. 4.7. *RHEED* oscillations of *GaAs* growth.

4.3. Low Electron Energy Diffraction (LEED) and Reflection of High Energy Electron Diffraction (RHEED)

The elastic scattering experiments are an important source of information about the symmetry and the geometry arrangement of atoms near the surface. The geometry and possible excitations of about 10^{15} surface atoms per cm^2 must be studied against the background of about 10^{23} atoms per cm^3 present in the bulk. For these reasons the appropriate geometry for surface and interface physics is the reflection geometry and the only particles that do not penetrate too deeply into the solid can be used. From Fig. 4.8, it is possible to observe that electrons are candidate probe.

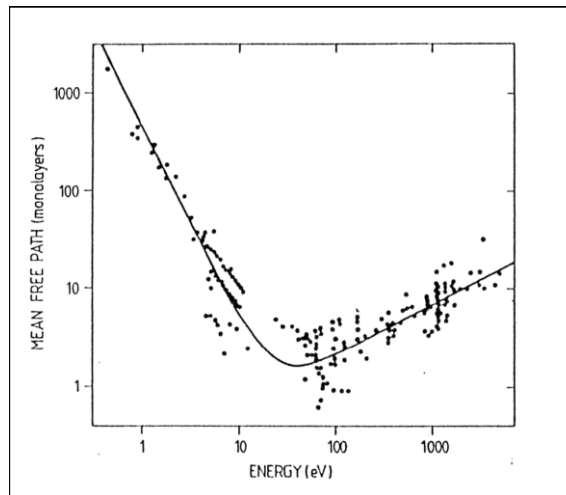


Fig. 4.8. Mean free path of electrons in solids as a function of their energy.

4.3.1. Theory of surface scattering

The interaction of the electrons with the lattice is described by the potential [7]:

$$V(\vec{r}, t) = \sum_{\vec{n}} v[\vec{r} - \vec{\rho}_{\vec{n}}(t)] \quad [4.14]$$

where $\vec{n} (= m, n, p)$ labels the atoms in a primitive lattice, and v is the interaction potential with a single near-surface atom at the position $\vec{\rho}_{\vec{n}}(t)$ that contains the time independent position $\vec{r}_{\vec{n}}$ and the displacement $\vec{s}_{\vec{n}}(t)$:

$$\vec{\rho}_{\vec{n}}(t) = \vec{r}_{\vec{n}} + \vec{s}_{\vec{n}}(t). \quad [4.15]$$

The incident particles have a wave vector \vec{k} whose modulus depends on the energy $E = \hbar^2 k^2 / 2m$ and after interaction with the surface, are scattered into a state \vec{k}' . The scattering probability per unit time according to time dependent perturbation theory is:

$$W_{\vec{k}\vec{k}'} = \lim_{\tau \rightarrow \infty} \frac{1}{\tau} |c_{\vec{k}\vec{k}'}(\tau)|^2 \quad [4.16]$$

where $c_{\vec{k}\vec{k}'}(\tau)$ is the transition amplitude referred to incident and scattered plane wave function ($\psi_i(\vec{r}, t) = V^{-1/2} e^{i(\vec{k}\cdot\vec{r} - Et/\hbar)}$ and $\psi_s(\vec{r}, t) = V^{-1/2} e^{i(\vec{k}'\cdot\vec{r} - E't/\hbar)}$):

$$c_{\vec{k}\vec{k}'}(\tau) = \frac{-i}{\hbar} \int d\vec{r} \int_0^\tau dt \psi_s^*(\vec{r}, t) V(\vec{r}) \psi_i(\vec{r}, t). \quad [4.17]$$

Substituting the expression of potential [4.14] and all the electrons incident and scattered in terms of plane wave function, the probability amplitude of scattering at time τ is:

$$c_{\vec{k}\vec{k}'}(\tau) = \frac{-i}{\hbar} \sum_{\vec{n}} \int_0^\tau e^{i(E' - E)t/\hbar} \int e^{i(\vec{k}' - \vec{k})\cdot\vec{r}} v[\vec{r} - \vec{\rho}_{\vec{n}}(t)] d\vec{r} dt. \quad [4.18]$$

The position of a moving atom is described by the vector $\vec{\xi} = \vec{r} - \vec{\rho}_{\vec{n}}(t)$ with $d\vec{\xi} = d\vec{r}$:

$$c_{\vec{k}\vec{k}'}(\tau) = \frac{-i}{\hbar} \sum_{\vec{n}} \int_0^\tau dt e^{i(E' - E)t/\hbar} e^{i(\vec{k}' - \vec{k})\cdot\vec{\rho}_{\vec{n}}(t)} \int d\vec{\xi} v(\vec{\xi}) d\vec{r} e^{-i(\vec{k}' - \vec{k})\cdot\vec{\xi}} \quad [4.19]$$

If the atomic scattering factor is:

$$f(\vec{K}) = \int d\vec{\xi} v(\vec{\xi}) e^{-i\vec{K}\cdot\vec{\xi}} \quad [4.20]$$

with $\vec{K} = \vec{k}' - \vec{k}$:

$$c_{\vec{k}\vec{k}'}(\tau) = \frac{-i}{\hbar} f(\vec{K}) \sum_{\vec{n}} \int_0^\tau dt e^{i(E' - E)t/\hbar} e^{i\vec{K}\cdot\vec{\rho}_{\vec{n}}(t)} \quad [4.21]$$

In the case of surface scattering the instantaneous position is:

$$\vec{\rho}_{\vec{n}}(t) = \vec{r}_{\vec{n}} + \vec{s}_{\vec{n}}(t) = \vec{r}_{\vec{n}_{\parallel}} + z_p \hat{e}_{\perp} + \vec{s}_{\vec{n}}(t) \quad [4.22]$$

The splitting into two components parallel and perpendicular to the surface is convenient because of the translational symmetry parallel to the surface which allows a Fourier representation of $\vec{s}_{\vec{n}}(t)$ with $\vec{n} = (\vec{n}_{\parallel}, p)$:

$$\vec{\rho}_{\vec{n}}(t) = \vec{r}_{\vec{n}_{\parallel}} + z_p \hat{e}_{\perp} + \sum_{q_{\parallel}} \hat{s}(\vec{q}_{\parallel}, z_p) \exp[\pm i\vec{q}_{\parallel} \cdot \vec{r}_{\vec{n}_{\parallel}} \pm i\omega(\vec{q}_{\parallel})t]. \quad [4.23]$$

In this representation the displacement from equilibrium $\vec{s}_{\vec{n}}(t)$ is described by harmonic waves with frequency $\omega(\vec{q}_{\parallel})$ and wave vector \vec{q}_{\parallel} parallel to the surface. Replacing [4.23] in [4.21]:

$$c_{\vec{k}\vec{k}'}(\tau) = \frac{-i}{\hbar} f(\vec{K}) \sum_{\vec{n}_{\parallel,p}} \int_0^{\tau} dt e^{i(E' - E)t/\hbar} \exp \left\{ -i\vec{K} \cdot [\vec{r}_{\vec{n}_{\parallel}} + z_p \hat{e}_{\perp} + \sum_{q_{\parallel}} \hat{s}(\vec{q}_{\parallel}, z_p) \exp[\pm i\vec{q}_{\parallel} \cdot \vec{r}_{\vec{n}_{\parallel}} \pm i\omega(\vec{q}_{\parallel})t]] \right\} \quad [4.24]$$

if the displacements from equilibrium are small, it is possible to expand with Taylor series the term $\exp[-i\vec{K} \cdot \vec{s}_{\vec{n}}(t)] \sim 1 - i\vec{K} \cdot \dots$. The term without the displacement contribution is the *elastic scattering*:

$$c_{\vec{k}\vec{k}'}(\tau) = \frac{-i}{\hbar} f(\vec{K}) \sum_{\vec{n}_{\parallel,p}} \int_0^{\tau} dt e^{i(E' - E)t/\hbar} e^{-i\vec{K} \cdot (\vec{r}_{\vec{n}_{\parallel}} + z_p \hat{e}_{\perp})}. \quad [4.25]$$

The elastic scattering rate $W_{\vec{k}\vec{k}'}$ can be found from [4.16] and gives the delta function $\delta(E' - E)$ in the time limit $\tau \rightarrow \infty$. The sum over the two dimensional set $\vec{n}_{\parallel} = (n, m)$ of the surface whose base vectors are (\vec{a}, \vec{b}) , contains terms like $\sum_{m,n} e^{-i\vec{K} \cdot (m\vec{a} + n\vec{b})} = \sum_{m,n} (e^{-i\vec{K} \cdot \vec{a}})^m (e^{-i\vec{K} \cdot \vec{b}})^n$. As in the case of a three dimensional lattice sum, in the limit of $m, n \rightarrow \infty$, there is non zero contribution only if the Laue conditions are satisfied:

$$\vec{K} \cdot \vec{a} = 2\pi h \text{ and } \vec{K} \cdot \vec{b} = 2\pi k \text{ with } h, k \text{ integer} \quad [4.26]$$

This condition is fulfilled, with $\vec{K} = \vec{K}_{\parallel} + K_{\perp} \hat{e}_{\perp}$, when:

$$\vec{K}_{\parallel} = \vec{k}'_{\parallel} - \vec{k}_{\parallel} = \vec{G}_{\parallel} \quad [4.27]$$

where \vec{G}_{\parallel} is a vector of the bi-dimensional reciprocal lattice. For N surface atoms the probability of elastic scattering becomes:

$$W_{\vec{k}\vec{k}'} = \frac{2\pi}{\hbar} N \left| f(\vec{K}) \sum_p e^{i\vec{K}_{\perp} z_p} \right|^2 \delta(E' - E) \delta_{\vec{K}_{\parallel}, \vec{G}_{\parallel}} \quad [4.28]$$

where the Krönecker delta $\delta_{\vec{K}_{\parallel}, \vec{G}_{\parallel}}$ is the expression [4.27].

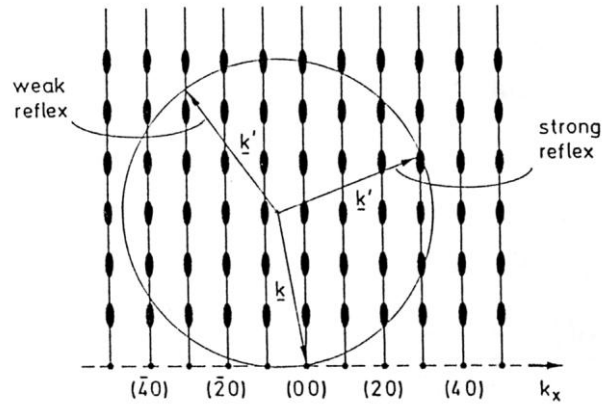


Fig. 4.9. Ewald construction for elastic scattering on a quasi-bi-dimensional surface lattice. The term “quasi” depends on the fact that not only the scattering from the topmost lattice plane, but also from underlying planes, is taken into account. The thicker region of the rods arise from the third Laue condition. For instance, the (30) reflection is high (bright spots) whereas the (31) is weak (dark spots).

The third Laue condition does not appear because the sum over the p index in [4.28] is not extended to $(-\infty, +\infty)$ but just to the range of the electron penetration depth. Taking into account the contribution of this sum, one obtains that the reciprocal space probed by diffracted electrons consists of a series of continuous rods parallel to the z direction (arbitrary taken as the direction normal to the surface) as shown in Fig. 4.9. The intensity of the diffracted beams is modulated along this direction and the modulation is generated by the third Laue condition. The lattice is represented by the function:

$$\sum_{n=-\infty}^{+\infty} \delta(x - na) \quad [4.29]$$

where a is the one dimensional direct lattice constant. The generic δ Dirac function term of the sum may be written as:

$$\delta(x - na) = \frac{1}{a} \sum_{v=-\infty}^{+\infty} e^{iv\frac{2\pi}{a}(x-na)} = \frac{1}{a} \sum_{G=-\infty}^{+\infty} e^{iG(x-na)} \quad [4.30]$$

where $G = v\frac{2\pi}{a} = vg$. The points identified by G constitute the reciprocal lattice. Thus the [4.30] becomes:

$$\delta(k - vg) = \frac{1}{g} \sum_{n=-\infty}^{+\infty} e^{ina(k-vg)} \quad [4.31]$$

where k is the continuous variable in the reciprocal lattice. Because the sum in [4.29] in real experiment is finite, the reciprocal space cannot be anymore represented by points but by lines. Setting $(k - vg)a = \alpha$, from [4.31] it is possible to write:

$$\begin{aligned} \frac{1}{g} \sum_{n=-N}^{+N} e^{ina} &= \frac{1}{g} + \frac{2}{g} \sum_{n=1}^N \cos n\alpha = \frac{1}{g} \left[1 + 2\operatorname{Re} \frac{e^{i\alpha}(1 - e^{iN\alpha})}{1 - e^{i\alpha}} \right] = \\ &= \frac{1}{g} \left[1 + 2\operatorname{Re} \frac{e^{i\alpha/2}(1 - e^{i(N+1/2)\alpha})}{-2i\sin(\alpha/2)} \right] = \\ &= \frac{1}{g} \left[1 + i \frac{[\sin(\alpha/2) - \sin((N+1/2)\alpha)]}{\sin(\alpha/2)} \right] = \frac{1}{g} \frac{\sin((N+1/2)\alpha)}{\sin(\alpha/2)} \quad [4.32] \end{aligned}$$

The last term oscillates as a function of N and has pronounced peaks. The FWHM of these peaks is a decreasing function of N . The zeroes are localized at the points $\alpha = 2m\pi/(2N+1)$ with m integer; thus the width of the function around the maxima is proportional to N^{-1} . In the limit $N \rightarrow \infty$ the function tends to a δ -Dirac function (3D lattice) and the corresponding reciprocal lattice is made up by points.

4.3.2. LEED

Low Electron Energy Diffraction is used as the standard technique to check the crystallographic quality of a surface [8]. The experimental apparatus collects elastically scattered electrons which produce a diffraction pattern made of single spots onto a fluorescent screen (Fig. 4.10)

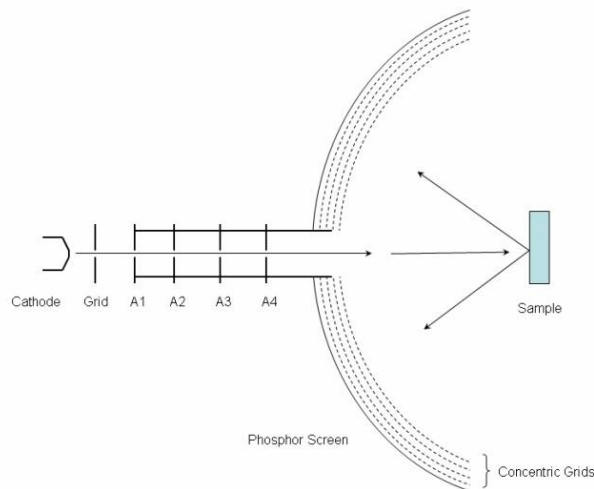


Fig. 4.10. **LEED** schematic representation.

Monochromatic electrons are emitted by a cathode filament which is at a negative potential, typically $10 - 600 \text{ V}$, with respect to the sample. They are accelerated and focused into a beam, typically about 0.1 to 0.5 mm wide, by a series of electrodes that serve as electron lenses. The energy necessary to diffraction processes can be found from De Broglie wavelength $\left(E(eV) = 151.3(\lambda(\text{\AA}))^{-2}\right)$ comparable with lattice constant and correspond to the range $10 - 600 \text{ eV}$. A part of electrons incident on the sample surface are backscattered elastically, and diffraction can be detected if sufficient order exists on the surface; electrons which penetrate deeply into the substrate have a high probability of being inelastically scattered (see Fig. 4.8). A **LEED** detector usually contains three or four hemispherical concentric grids and a phosphor screen. The grids are used for screening out the inelastically scattered electrons. The first grid screens the space above the sample from the retarding field. The next grid is at a potential to block low energy electrons, it is called the suppressor. To make the retarding field homogeneous and mechanically more stable this grid often consists of two grids. The fourth grid is only necessary when the **LEED** is used to measure the current at the screen.

To understand the essential features, kinematic theory is sufficient. The condition for elastic Bragg spot is given by [4.27]. This condition is valid for the limiting case where only the topmost atomic layer is involved in scattering. Elastically scattered electrons have to fulfill the periodicity of surface lattice $(\chi_s(\vec{r}))$ and the generic wave function is:

$$\phi_s(\vec{r}) = e^{i\vec{k}_{\parallel}\cdot\vec{r}_{\parallel}}\chi_s(\vec{r}) \quad [4.33]$$

By exploiting the Fourier expansion of the function $\chi_s(\vec{r})$ we can write:

$$\chi_s(\vec{r}) = \sum_G \alpha_G e^{i\vec{G}_{\parallel}\cdot\vec{r}_{\parallel}} \quad [4.34]$$

Substituting $\phi_s(\vec{r})$ and the incident electrons $\phi_i(\vec{r}) = e^{i\vec{k}\cdot\vec{r}}$ in the Schrödinger equation, the scattered wave outside the crystal becomes:

$$\phi_s(\vec{r}) = \sum_G A_G e^{i\vec{k}_G\cdot\vec{r}} \quad [4.35]$$

with A_G constant and \vec{k}_G of components:

$$\vec{k}_G = \left[k_x + G_x, k_y + G_y, -\sqrt{2\frac{m_e E}{\hbar^2} - |\vec{k}_\parallel + \vec{G}|^2} \right]. \quad [4.36]$$

Elastic scattering implies $|\vec{k}|^2 = |\vec{k}_G|^2$ for any value of \vec{G} .

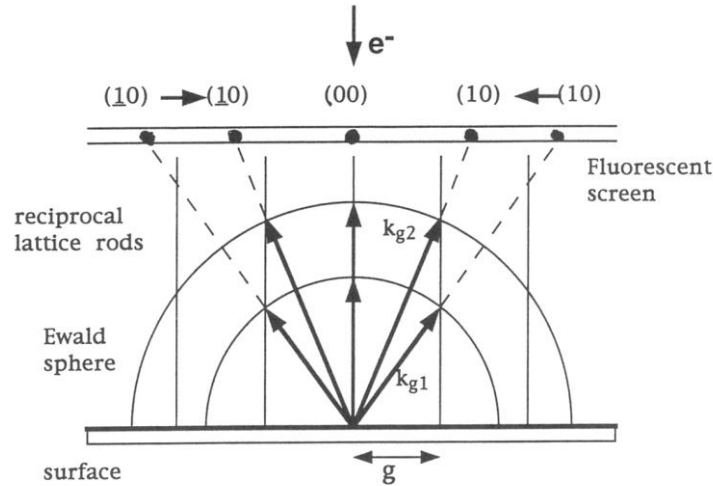


Fig.4.11. LEED experiment: correspondence between the wave vector \vec{k}_G and the diffraction pattern. Changing the primary energy E changes also \vec{k}_G (see [4.36]) and more rods are involved increasing the number of spots.

The end of \vec{k}_G vector describes the Ewald sphere, whose radii are $|\vec{k}|^2$ and the diffracted waves form a discrete series whose directions are the \vec{k}_G vectors. In the experimental arrangement used in **LEED** spectroscopy the electron beam is normal to the surface so that $\vec{k}_\parallel = 0$. Thus the component parallel to the surface of the wavevector is $\vec{k}_G = \vec{G}_\parallel$. The fluorescent screen images the projection of the intersection points between the Ewald sphere and the rods of the 2D reciprocal lattice G . Since the Ewald sphere radius is $\frac{m_e E}{\hbar^2}$, the increase of E increases the number of the diffracted beams. Therefore the diffraction pattern is contracted and a larger number of spots is observed.

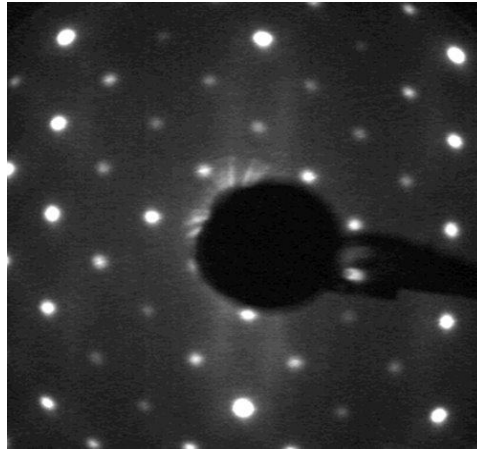


Fig. 4.12. Typical pattern of reconstructed $GaAs(001)c(4 \times 4)$. The brighter spots represents the bulk layer diffraction; the darker spots represents the reconstructed layers. The primary energy is 42.6 eV .

4.3.3. RHEED

RHEED is another application of elastic electron scattering used to monitor the surface symmetry, reconstruction, morphology and disorder [7]. In particular, as explained in section 4.2.1, **RHEED** can provide important information about proper **MBE** growth conditions because of the small angle of incidence ($\theta \sim 1^\circ \div 3^\circ$); a consequence of this geometry is that the electrons probes few atomic layers, improving the surface sensitivity. All other electron diffractions technique, because of their geometry, are unsuitable during **MBE** growth. The **RHEED** pattern can be visualized as an intersection of Ewald sphere, whose radius is large at energy $> 5 \text{ keV}$, with a set of reciprocal lattice rods (Fig. 4.13). In this way the spacing between the rods can be related to the spacing between rows of atoms in the surface layer. The high energy implies that the Ewald sphere intersects a lot of rods and, contrary to **LEED**, a elongated streaks appear also because the beam is not perfectly monochromatic and the Ewald sphere is thick. When the flat surface become more rough, the streaks become fragmented and longer; when the surface is 3D the streaks change in spots. Measurement along two or three different azimuth (distance between two streaks) are required to determine the surface symmetry. The continuous rods of the reciprocal lattice are normal to the surface and possess 2D translation symmetry (as in **LEED**). The Ewald sphere intersects all rods contained in the projection of this sphere onto the surface. Diffracted beams are thus observed in the angular directions α and β Since the Ewald sphere

radius is very large, the angles between successive reflections will be practically the same and are given by:

$$\beta_0 = \operatorname{arctg} \left[\frac{g_{\perp}}{\sqrt{(k_0^2 - g_{\perp}^2)}} \right] = \operatorname{arctg} \left(\frac{t}{L} \right). \quad [4.37]$$

Since $g_{\perp} = 2\pi/d_{\parallel}$ where d_{\parallel} is the distance between equivalent rows of atoms parallel to the incident beam and $g_{\perp} \ll k_0$, it is possible to reduce the [4.37] to $d_{\parallel}t = L\lambda_0$, where λ_0 is the wavelength of the incident electron. A **RHEED** pattern can be defined good if the streaks are narrow (low thermic excitation and low number of defects) and not too long (high monochromaticity of the beam); Fig. 4.14 represents a typical $c(4 \times 4)$ with the lighter strikes corresponding the bulk diffraction and the thinner and darker strikes corresponding the surface reconstructed diffraction.

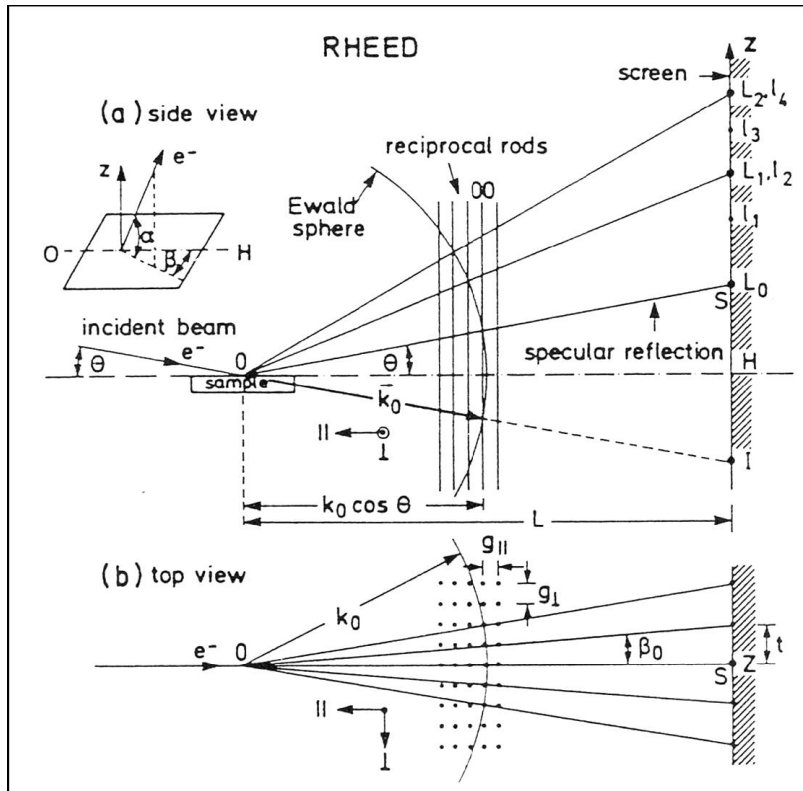


Fig. 4.13. Schematic picture of a typical **RHEED**. L is the distance sample screen, while L_n corresponds to Laue zones of the ideal surface, and l_n corresponds to the intermediate Laue zones induced by surface reconstruction. In a good **RHEED** pattern it is possible to observe the second Laue zone.

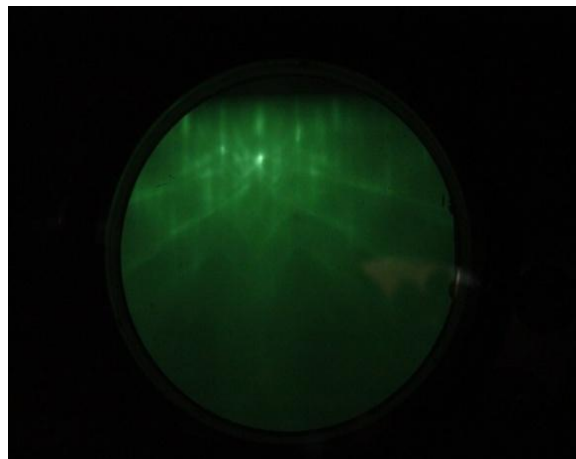


Fig. 4.14. **RHEED** pattern of reconstructed $GaAs(001)c(4 \times 4)$. The lighter strikes correspond to the bulk diffraction and the thinner and darker strikes correspond to the surface reconstructed diffraction.

4.4. Electron Energy Loss Spectroscopy (EELS)

EELS technique is based on the analysis of electron energy losses undergone by primary electrons by means of the interaction with sample. The energy losses are due to inelastic scattering with the surface and offers information about elementary excitations of the crystal [9]. The processes involved are mainly three:

1. excitation of lattice vibrations of atoms on a clean surface (acoustical and optical) phonons and vibrations of adsorbate atomic and molecular species;
2. excitation of transitions involving the valence band (interband or intraband electronic excitation, surface states and plasmon of bulk, surface or interface);
3. core-level excitations.

The spectral range of energy losses extends from few tenths of meV for phonons or adsorbate vibrations, to several hundreds of eV necessary to ionize core electrons. Energy losses spectroscopy is very similar to optical spectroscopy with the advantages that it is possible to change the energy of incident electrons very easily and the shallow penetration of electrons that makes this technique more sensitive to the surface.

To understand the loss of energy after interaction of electrons with the sample surface, we recall the amplitude probability of scattering $c_{\vec{k}\vec{k}'}(\tau)$. The second term after Taylor expansion of [4.24] with displacement contribution is the *inelastic scattering*:

$$\begin{aligned}
 c_{\vec{k}\vec{k}'}^{inel}(\tau) &= \frac{-i}{\hbar} f(\vec{K}) \sum_{\vec{n}_{\parallel}, p} \int_0^{\tau} dt \exp[i(E' - E)t/\hbar] \exp[-i\vec{K} \cdot (\vec{r}_{\vec{n}_{\parallel}} + z_p \hat{e}_{\perp})] \times \\
 &\quad \times (-1) \sum_{\vec{q}_{\parallel}} \vec{K} \cdot \hat{s}(\vec{q}_{\parallel}, z_p) \exp[\pm i(\vec{q}_{\parallel} \cdot \vec{r}_{\vec{n}_{\parallel}} + i\omega(\vec{q}_{\parallel})t)] = \\
 &= -\hbar^{-1} f(\vec{K}) \sum_{\vec{n}_{\parallel}, p, \vec{q}_{\parallel}} \vec{K} \cdot \hat{s}(\vec{q}_{\parallel}, z_p) \exp[-i(\vec{K}_{\parallel} + \vec{q}_{\parallel}) \cdot \vec{r}_{\vec{n}_{\parallel}}] \times \\
 &\quad \times \exp(-iK_{\perp} z_p) \int_0^{\tau} dt \exp[i(E' - E \pm \hbar\omega)t/\hbar] dt. \tag{4.38}
 \end{aligned}$$

The *inelastic scattering probability* becomes:

$$\begin{aligned}
W_{\vec{k}\vec{k}'}^{inel} &= \frac{2\pi}{\hbar} N \sum_{\vec{q}_{\parallel}} \delta(E' - E \pm \hbar\omega(\vec{q}_{\parallel})) \delta_{\vec{K}_{\parallel} \pm \vec{q}_{\parallel}, \vec{G}_{\parallel}} \times \\
&\times \sum_p |f(\vec{K}) \vec{K} \cdot \hat{s}(\vec{q}_{\parallel}, z_p) \exp[-iK_{\perp} z_p]|^2
\end{aligned} \tag{4.39}$$

where N is the number of surface atoms. In the first part, the delta function and the Krönecher δ ensure energy conservation and the conservation of the wave vector component parallel to the surface:

$$\begin{aligned}
E' &= E \mp \hbar\omega(\vec{q}_{\parallel}) \\
\vec{K}_{\parallel} &= \vec{k}'_{\parallel} - \vec{k}_{\parallel} = \pm \vec{q}_{\parallel} + \vec{G}_{\parallel}.
\end{aligned} \tag{4.40}$$

The first equation [4.40] indicates that in all inelastic scattering processes the energy lost must be found as quantum energy of an excited surface mode. The second equation indicates the conservation of particle wave vector component parallel to the surface. The second term of [4.39] yields a selection rule for surface scattering, which helps to identify the symmetry of an excited vibrational surface excitation: if \vec{K} is perpendicular to the direction of the atomic displacement (or the electronic dipole moment) $\hat{s}(\vec{q}_{\parallel}, z_p)$, the inelastic scattering vanishes. The energy $\hbar\omega$ and wave vector \vec{q}_{\parallel} may be transferred to collective surface excitations like phonons, plasmons, etc., to single particles like electrons in the conduction band (intra band scattering), or to electrons excited from an occupied electron band into an empty one (inter band scattering). In all these cases, the characteristic excitation $\hbar\omega$ requires a definite momentum transfer (\vec{q}_{\parallel}). On a periodic crystal, surface collective excitations are described by a dispersion relation $\hbar\omega(\vec{q}_{\parallel})$ and in scattering processes within band structure $E(\vec{k}_{\parallel})$ it is possible to write: $E'(\vec{k}'_{\parallel}) - E(\vec{k}_{\parallel}) = \hbar\omega(\vec{q}_{\parallel})$. The scattered wave vector in inelastic processes \vec{k}' differs from the specular vector \vec{k}_s (typical of elastic scattering) by the transfer vector \vec{q} (if $\vec{G}_{\parallel} = 0$):

$$\vec{k}' = \vec{k} - \begin{pmatrix} q_x \\ q_y \\ \Delta k_z \end{pmatrix} \tag{4.41}$$

Only components of surface plane (q_x, q_y) are fixed by a conservation law; Δk_z depends only on energy and scattering geometry.

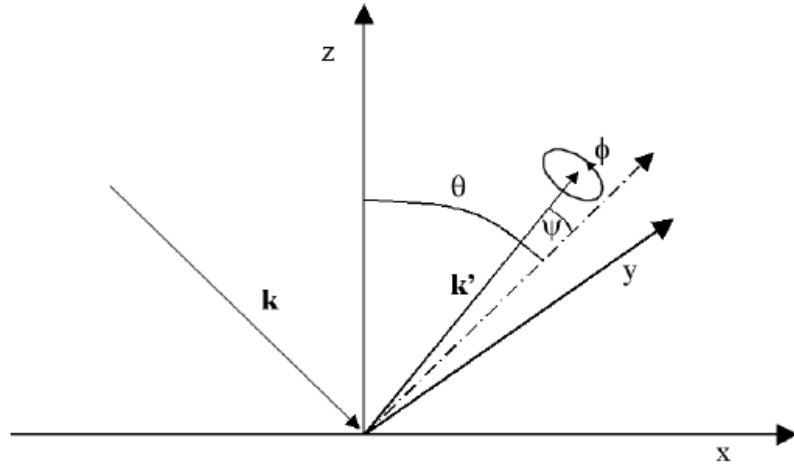


Fig. 4.15. Schematic representation of inelastic scattering as a function of azimuthal angle θ (between the scattering direction and the axis z normal to the surface), the polar angle ϕ (around the scattering direction) and the deflection angle ψ from the specular scattering direction [10].

In the rotated system like Fig. 4.15, the specular wave vector \vec{k}_s and the inelastically scattered wave vector \vec{k}' have simple representations:

$$\vec{k}_s = k \begin{pmatrix} 0 \\ 0 \\ 1 \end{pmatrix} \text{ and } \vec{k}' = k' \begin{pmatrix} -\sin\psi\cos\phi \\ \sin\psi\sin\phi \\ \cos\psi \end{pmatrix} \quad [4.42]$$

Their representation in the coordinate system of Fig. 4.15, is obtained by a rotation around y axis using the rotation matrix:

$$R = \begin{pmatrix} \cos\theta & 0 & \sin\theta \\ 0 & 1 & 0 \\ -\sin\theta & 0 & \cos\theta \end{pmatrix} \quad [4.43]$$

For specular and scattered waves:

$$\vec{k}_s = k \begin{pmatrix} \sin\theta \\ 0 \\ \cos\theta \end{pmatrix} \quad [4.44]$$

$$\vec{k}' = k' \begin{pmatrix} -\sin\psi\cos\phi\cos\theta + \cos\psi\sin\theta \\ \sin\psi\sin\phi \\ \sin\psi\cos\phi\sin\theta + \cos\psi\cos\theta \end{pmatrix} \quad [4.45]$$

Combining [4.41] with [4.44] and [4.45] and considering the energy conservation ($k' = k(1 - \hbar\omega/E)^{1/2}$) it is possible to obtain:

$$\vec{k}' - \vec{k} = \begin{pmatrix} q_x \\ q_y \\ \Delta k_z \end{pmatrix} = k \left[\begin{pmatrix} \sin\theta \\ 0 \\ -\cos\theta \end{pmatrix} - \sqrt{1 - \frac{\hbar\omega}{E}} \begin{pmatrix} \cos\psi\sin\theta - \sin\psi\cos\varphi\cos\theta \\ \sin\psi\sin\varphi \\ \sin\psi\cos\varphi\sin\theta + \cos\psi\cos\theta \end{pmatrix} \right] \quad [4.46]$$

In energy loss experiment θ determine the angle of incidence of primary beam, and the position of entrance aperture to the energy analyzer is described by the angles ψ and φ . In the case of planar scattering ($\varphi = 0, \pi$) the equation [4.46] can be simplified and the wave vector parallel to the surface ($q_{\parallel} = q_x$) is then given by:

$$q_{\parallel} = k \left[\sin\theta + \sqrt{1 - \frac{\hbar\omega}{E}} (\sin\psi\cos\theta - \cos\psi\sin\theta) \right] \quad [4.47]$$

If the diffused beam is analyzed in the specular direction ($\psi = 0$) and the energy E is large compared to the loss energies ($\hbar\omega/E \ll 1$), eq. [4.47] becomes:

$$q_{\parallel} \cong k \frac{\hbar\omega}{2E} \sin\theta \quad [4.48]$$

The case of small values of $\hbar\omega/E$ and specular diffusion is relevant when low energy electrons are diffused by a long range potential.

The detailed description of a scattering process needs the knowledge of the nature of interaction between incident electrons and vibrating atoms at the surface; this is very difficult because of the strong interaction of the electrons with the substrate. However it is very useful to distinguish two limit cases (only for mathematical simplification) *dipole scattering* and *impact scattering*. If we describe the periodic crystal as a fixed charge distribution and time independent, the electric field outside the crystal is very weak and highly localized at the surface [11]. The inelastic scattering due to this short range potential is the *impact scattering*. However the crystal charge fluctuates because of the zero point motion related to excitation like plasmons, surface phonons or single particle excitations. This fluctuation of charge density, also possibly made by dynamic dipole moments of atoms or molecules adsorbed at the surface, generate a time dependent electric dipole field that extends outside the surface; this field interacts with incoming electrons and a long range scattering occurs, the *dipole scattering*. The long range field generates small angles scattering processes that are very intense and it is possible to obtain a simple formula for cross section, contrary to large angle scattering that needs a microscopic treatments. Ours

experimental apparatus is at fixed geometry and permits to analyze the electron diffused around specular direction and *dipole scattering* prevails.

4.4.1. Small angle inelastic scattering (*dipole scattering*)

The cross section per unity solid angle Ω and per energy loss $\hbar\omega$ is given by the following expression [11 - 14]:

$$\frac{\partial^2 S}{\partial(\hbar\omega)\partial\Omega} = \frac{m^2 e^2 v_{\perp}^2}{n\pi\hbar^5 \cos\theta} \left(\frac{k'}{k}\right) \frac{|v_{\perp} q_{\parallel} (R_s \mp R_l) + i(R_s - R_l)(\omega - \vec{v}_{\parallel} \cdot \vec{q}_{\parallel})|^2}{[q_{\parallel}^2 v_{\perp}^2 + (\omega - \vec{v}_{\parallel} \cdot \vec{q}_{\parallel})^2]^2} \frac{P(\vec{q}_{\parallel}, \omega)}{\vec{q}_{\parallel}^2} \quad [4.49]$$

where v_{\perp} and v_{\parallel} are the velocity component of incoming electrons, R_s and R_l are the reflectivity coefficients of scattered and incoming electrons and $P(\vec{q}_{\parallel}, \omega)$ is the correlation function of the surface charge density fluctuation. Assuming for simplicity, because of the low energy losses, $R_s = R_l = R$ the [4.49] become:

$$\frac{\partial^2 S}{\partial(\hbar\omega)\partial\Omega} = \frac{m^2 e^2 v_{\perp}^2}{\pi\hbar^5 \cos\theta} \left(\frac{k'}{k}\right) \frac{2v_{\perp}^2 R^2}{[q_{\parallel}^2 v_{\perp}^2 + (\omega - \vec{v}_{\parallel} \cdot \vec{q}_{\parallel})^2]^2} P(\vec{q}_{\parallel}, \omega). \quad [4.50]$$

Actually the component R is less than unity because of the loss of energy in inelastic processes. In the expression [4.50] the crucial term is the correlation function, all the other terms depend on kinematic diffusion. Otherwise the function $P(\vec{q}_{\parallel}, \omega)$ contains all physics of surface and corresponds to [11, 16]:

$$P(\vec{q}_{\parallel}, \omega) = \frac{2\hbar q_{\parallel}}{\pi} n(\omega) \text{Im} \left[\frac{-1}{1 + \tilde{\varepsilon}(\omega, \vec{q}_{\parallel})} \right] \quad [4.51]$$

where $n(\omega) = \frac{1}{e^{\hbar\omega/kT} - 1}$ is the Bose occupation coefficient and $\tilde{\varepsilon}(\omega, \vec{q}_{\parallel})$ is a efficace dielectric function that depends on transferred momentum \vec{q}_{\parallel} . In the case of isotropic crystal $\tilde{\varepsilon}(\omega, \vec{q}_{\parallel})$ is the dielectric tensor $\varepsilon(\omega, \vec{q}_{\parallel})$, whereas for anisotropic system efficace dielectric function has the dielectric tensor and momentum transferred components. Substituting [4.51] in [4.50] it is possible to obtain:

$$\frac{\partial^2 S}{\partial(\hbar\omega)\partial\Omega} = \frac{4m^2 e^2 v_{\perp}^4}{\pi^2 \hbar^3 \cos\theta} \left(\frac{k'}{k}\right) \frac{2v_{\perp}^2 R^2}{[q_{\parallel}^2 v_{\perp}^2 + (\omega - \vec{v}_{\parallel} \cdot \vec{q}_{\parallel})^2]^2} n(\omega) \text{Im} \left[\frac{-1}{1 + \tilde{\varepsilon}(\omega, \vec{q}_{\parallel})} \right].$$

[4.52]

This is the probability that electrons gain energy; but we are interested in the loss energy so we substitute $1 - n(\omega)$, instead $n(\omega)$, that is about 1 in the case of no so low losses. So it is possible to write:

$$\frac{\partial^2 \mathcal{S}}{\partial(\hbar\omega)\partial\Omega} = A(\vec{k}', \vec{k}) f(\omega, \vec{q}_{\parallel}) \quad [4.53]$$

$A(\vec{k}', \vec{k})$ is the kinematic factor and depends on energy loss $\hbar\omega$ but doesn't depends on medium properties, whereas the *loss function* $f(\omega, \vec{q}_{\parallel}) = \text{Im} \left[\frac{-1}{1 + \varepsilon_{eff}(\omega, \vec{q}_{\parallel})} \right]$ contains information on the medium like electronics and vibrationals surface properties. The calculation of the dielectric matrix needs the knowledge of all many body states, so an important simplification is to treat the problem in the *Random Phase Approximation (RPA)* [15] that describes a homogenous electron system with a diagonal matrix (actually this method doesn't take care of local field effects).

In the two mediums model, we consider a truncated solid, simulated by an interface vacuum-solid ($\varepsilon = 1$; $\varepsilon(\omega)$). This case is used when the surface does not has reconstruction and also when the surface has a simple buckling. The solution of the loss function can be found solving the Poisson equation imposing the contours conditions on the interface potential. For brevity it is reported only the final formula, the details can be found in [16]. If the dielectric tensor is the diagonal matrix (**RPA** simplification) $\varepsilon_{\alpha\beta}$ with α and β the components x, y and z , the loss function becomes:

$$f(\omega, \vec{q}_{\parallel}) = \text{Im} \left[\frac{-1}{1 + \frac{1}{q_{\parallel}} \left[\varepsilon_{zz}(\omega) \left(q_x^2 \varepsilon_{xx}(\omega) + q_y^2 \varepsilon_{yy}(\omega) \right) \right]^{1/2}} \right]. \quad [4.54]$$

In a isotropic crystal it is possible to obtain a great simplification because $\varepsilon_{zz}(\omega) = \varepsilon_{xx}(\omega) = \varepsilon_{yy}(\omega) = \varepsilon(\omega)$. In this case $\varepsilon_{eff}(\omega, \vec{q}_{\parallel}) = \varepsilon(\omega)$ and so:

$$f(\omega) = \text{Im} \left[\frac{-1}{1 + \varepsilon(\omega)} \right]. \quad [4.55]$$

This is the same result obtained with the dielectric theory [7] for a two mediums system with $\varepsilon(z, \omega) = \{1 \ z > 0, \varepsilon(\omega) \ z < 0\}$.

In the more general case of reconstructed surface, it is necessary to add a layer between vacuum and bulk. In this case we have:

- vacuum with $z > 0$ and $\varepsilon(\omega) = 1$;
- surface layer with $-d < z < 0$ and dielectric tensor $\varepsilon_{\alpha\beta}(z, \omega)$;
- bulk with $-\infty < z < -d$ and assumed isotropic with scalar dielectric function $\varepsilon_b(\omega)$.

In this case the ε_{eff} becomes:

$$\varepsilon_{eff} = \frac{q_{\parallel} \varepsilon_b q_{\parallel} \sinh \gamma d + \gamma \varepsilon_{zz} \cosh \gamma d}{\gamma \varepsilon_{zz} \varepsilon_b q_{\parallel} \cosh \gamma d + \gamma \varepsilon_{zz} \sinh \gamma d} \quad [4.56]$$

with $\gamma = \pm \frac{1}{\varepsilon_{zz}} [\varepsilon_{zz} (q_x^2 \varepsilon_{xx} + q_y^2 \varepsilon_{yy})]^{1/2}$.

Assuming that the scattering takes place in the xy plane, $\varepsilon_{xx} = \varepsilon_{yy} \neq \varepsilon_{zz}$, $q_{\parallel} = q_x$ and consequently $|\gamma| = q_x \sqrt{\frac{\varepsilon_{xx}}{\varepsilon_{zz}}}$. Calling $\gamma = -i\tilde{q}$, it is possible to write:

$$\varepsilon_{eff} = \varepsilon \frac{\varepsilon_b \cos \tilde{q} d - \varepsilon \sin \tilde{q} d}{\varepsilon_b \sin \tilde{q} d + \varepsilon \cos \tilde{q} d} \quad [4.57]$$

with $\frac{q_x}{\tilde{q} \varepsilon_{zz}} = \frac{1}{\varepsilon}$. This result is the same obtained with Mills [11] theory and it is applicable in the case of surface with weak anisotropy like *GaAs*(001) reconstructions.

In order to compare quantitatively theory and experiment one has to include the finite size and the angular aperture of the spectrometer. Furthermore, when loss spectra are observed in the direction of specular reflection, as we did, a considerable momentum transfer is involved at high energy loss energies. One therefore has to introduce the kinematic of the scattering into equation [4.52]. We consider circular and rectangular slits in front of the analyzer. The kinetic factor in [4.52] can be written as $\frac{q_{\parallel}}{|q_{\parallel}^2 + (\nabla k_z)^2|^2}$

with $\nabla k_z = \frac{(\omega - \vec{v}_{\parallel} \cdot \vec{q}_{\parallel})}{v_{\perp}}$. If we write q_{\parallel} in the form [4.46] and integrating the kinetic factor it

is possible to obtain:

$$F_{circ} = \int_{d\Omega} d\Omega \frac{q_{\parallel}}{|q_{\parallel}^2 + (\nabla k_z)^2|^2} = \int_0^{2\pi} d\varphi \int_0^{\Delta\psi} \sin\psi d\psi \frac{q_{\parallel}}{|q_{\parallel}^2 + (\nabla k_z)^2|^2} \quad [4.58]$$

where $\Delta\psi$ is the angular aperture of the detector and F_{circ} is the finite aperture size correction. For the rectangular aperture it is convenient to choose the coordinates of figure 4.16. \vec{q} is written as:

$$\vec{q} = k \left[\begin{pmatrix} \sin\theta \\ 0 \\ \cos\theta \end{pmatrix} - \sqrt{1 - \frac{\hbar\omega}{E}} \begin{pmatrix} \cos\varphi \sin(\psi+\theta) \\ -\sin\varphi \sin(\psi+\theta) \\ \cos(\psi+\theta) \end{pmatrix} \right]$$

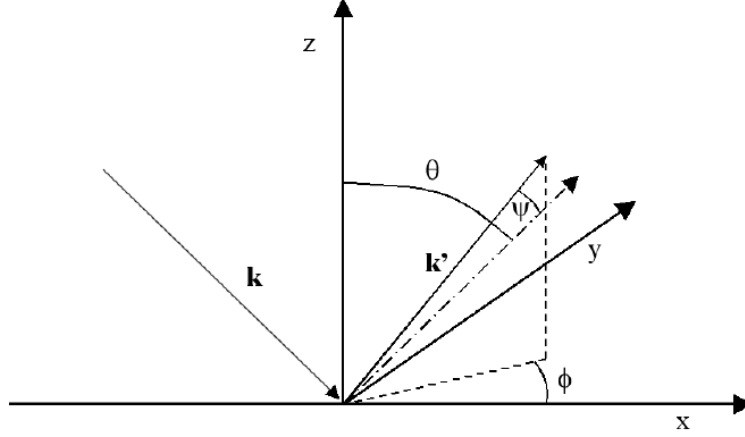


Fig. 4.16. Schematic representation of inelastic scattering as a function of azimuthal angle θ (between the scattering direction and the axis z normal to the surface), the angle φ (between the projection of scattering direction on xy axis and the x axis) and the deflection angle ψ from the specular scattering direction.

We obtain:

$$F_{rect} = \int_{d\Omega} \frac{q_{\parallel}}{|q_{\parallel}^2 + (\nabla k_z)^2|^2} = \int_{-\Delta\varphi/2}^{\Delta\varphi/2} d\varphi \int_{-\Delta\psi/2}^{\Delta\psi/2} \sin\psi d\psi \frac{q_{\parallel}}{|q_{\parallel}^2 + (\nabla k_z)^2|^2} \quad [4.59]$$

F_{circ} and F_{rect} for different values of the parameter $\alpha = \hbar\omega/2E$ taking $\theta = 45^\circ$, $\Delta\psi = 1^\circ$ for the circular aperture and $\Delta\psi = \Delta\varphi = 2^\circ$ for the square aperture has been calculated.

The values of F_{circ} and F_{rect} for values of α ranging from 0.05 to 0.5 are reported below.

α	$F_{circ} (\times 10^{-5})$	$F_{square} (\times 10^{-5})$
0.02	52.25	65.79
0.03	18.61	23.43
0.05	4.410	5.581
0.10	0.5362	0.6819
0.15	0.1463	0.1862
0.20	5.587×10^{-2}	7112×10^{-2}
0.25	2.550×10^{-2}	3247×10^{-2}
0.30	1.291×10^{-2}	1.645×10^{-2}
0.40	3.799×10^{-3}	4.838×10^{-3}
0.50	6.420×10^{-4}	8.174×10^{-3}

4.5. Scanning Tunneling Microscopy (STM)

Scanning Tunneling Microscopy (**STM**) is a peculiar technique to resolve the electronic states energetically as well as spatially with sub-nanometer resolution (17, 18). In Fig. 4.17 it is reported a schematic description of the microscope.

If a conducting metal that terminates ideally with one atom (the tip) is placed within a few atomic distances (some nm) from the sample surface, quantum mechanics allows for transmission of an electron from the tip to the sample through the potential barrier of the vacuum. This process is called tunneling and in general is determined by the spatial overlap between electronic surface states of the tip and the sample at the same energy.

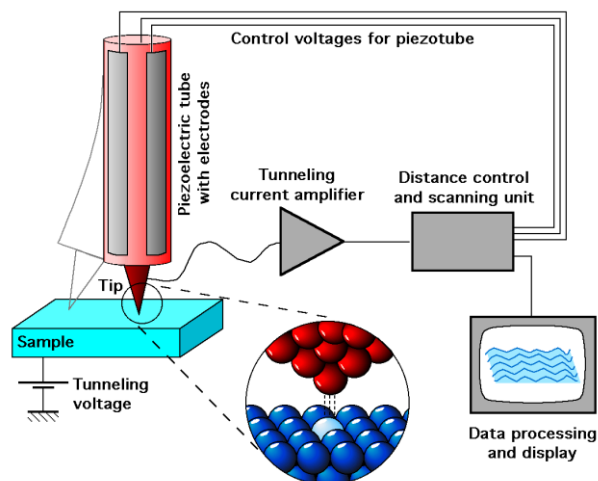


Fig. 4.17. Schematic description of scanning tunneling microscope. The approach tip-sample is driven by electronics and stops the movement when a tunneling current is detected..

The tunnel current is determined by the convolution of the electronic tip and sample states according to Bardeen's formula:

$$I = \frac{4\pi e}{\hbar} \int_0^{eV} \rho^S(E_F^S - eV + \varepsilon) \rho^T(E_F^T + \varepsilon) |M|^2 d\varepsilon \quad [4.60]$$

where eV is the Fermi energy difference between the tip and sample levels, being V the applied voltage; M is the tunneling matrix, determined by the overlap between the tip apex wave-function and surface states of the sample surface. Usually the tip made of tungsten or other transition metals has a d state on the apex. The magnitude of the matrix element is

usually assumed not to change significantly in the energy range of interest and may be treated as a constant. Indeed, it cannot be put constant when the size of the surface features are smaller than that of the tip state. In fact in this case (for example, when no atomic resolution is achieved) or in the case when the density of states varies considerably within the area of interest, it is convenient to describe the electronic contrast in terms of varying the sample density of states $\rho_s(x, y)$ (**LDOS**), i.e. the amount of energy levels per energy window and a surface unit. However, ρ does not contain the spatial structure of the wave functions corresponding to each energy level, but only describes the variation of the amount of levels on the surface. It is the matrix element that determines the spatial resolution of the surface states and contains information about the shape of the wave-function associated with the state localized on the sample surface.

The wave function of a localized state in the sample (for example, of a shallow acceptor and p -type tip state) is given by the product of the envelope function $\Phi(r)$ and Bloch states of the valence band top $\psi(r)$. Then the measured charge density [19]:

$$|\Phi^{ST}(r)|^2 \propto |M|^2 \propto \left| \frac{\partial \psi(r)}{\partial r} \Phi(r) + \frac{\partial \Phi(r)}{\partial r} \psi(r) \right|^2 \approx \frac{\partial \psi(r)}{\partial r} \Phi(r) \quad [4.61]$$

still contains the envelope function in its original form if $\Phi(r)$ is a slowly varying function of r as compared to $\psi(r)$. Then, taking into account the exponential decay of the sample wave-functions into the vacuum, for the localized state on the (x, y) surface the equation [4.60] may be written in the following form:

$$I(x, y, eV) \propto \int_0^{eV} \rho^S(\varepsilon) |\Phi(x, y)|^2 e^{-2k(\varepsilon)z(x, y, eV)} d\varepsilon \quad [4.62]$$

where $k(\varepsilon) = \frac{\sqrt{2m\xi}}{\hbar}$. Here $z(x, y, eV)$ is an absolute distance between the tip and the sample; ξ is the height of the vacuum potential barrier; m is the electron mass. For simplicity, the tip density of states is assumed to be a constant value in the whole energy range. The strong exponential dependence of the tunnel current on the tip-sample displacement is utilized in the **STM**. In constant-current mode the tunneling current I is kept constant at a certain set point value (usually $I_{sp} \sim 0.05 \div 1$ nA). If there is a local change in an electronic structure or the tip-sample distance, the tip will retract or approach the sample surface in order to compensate for the current change and keep the current at a constant

set point value. This is done by implementation of the feedback system that maintains the tunnel current by regulating the distance between the sample and the tip with picometer precision (see Fig. 4.17). In this way, the movements of the tip (x, y and z displacements) compose the so-called "constant-current" image of the surface containing information about both electronic and topographical variations. If the momentum k in equation [4.62] is a slowly varying function of energy, then integration results in a constant factor I_0 and equation [4.62] can be written as:

$$I(x, y, eV) \propto I_0 e^{-2kz(x, y, eV)} |\Phi(x, y)|^2 \quad [4.63]$$

whence the electronic profile recorded in the constant-current mode with the current set point I_{SP} depends logarithmically on the charge density of the surface states:

$$z(x, y, eV) = \frac{1}{2k} \ln \left[\frac{I_0}{I_{SP}} |\Phi(x, y)|^2 \right] \quad [4.64]$$

The same logarithmic dependence one can obtain if the tunneling element is assumed to be a constant and the local density of states is varying as a function of surface coordinates.

STM is a powerful surface investigation tool because allows also to probe the charge density distribution of a sample surface; this is the so called Scanning Tunneling Spectroscopy (**STS**). This measurement is performed acquiring the tunneling current $I(V)$ as a function of V keeping constant the tip sample distance; when the tip scans the surface a $I(V)$ curve is acquired for each point of scanning line. In order to keep the tip-sample separation constant, $I(V)$ spectra are acquired with the feedback signal switched off. Otherwise, the sample DOS does not have a definitive relation to the tunneling spectrum. If the tip DOS and the tip-sample separation are constant, then equation [4.60] implies:

$$\frac{dI}{dV} \sim \rho^S (E_F^S - eV + \varepsilon). \quad [4.65]$$

One of the major problems in doing tunneling spectroscopy with **STM** is that the tunneling current exhibits a strong dependence on the tip-sample separation, which means that the tunneling current varies approximately by one order of magnitude per one angstrom. Therefore, the measured spectroscopic data need a normalization of an intensity quantity with respect to energy, rather than it's absolute value. Feenstra et al. [20] proposed a parameter, the normalized dynamic conductance:

$$g(V) = \frac{d \ln I}{d \ln V} = \frac{dI}{dV} \frac{V}{I} \quad [4.66]$$

which is a dimensionless quantity. Spectroscopic maps with high energy resolution are time consuming due to long integration times. This makes it difficult to implement these techniques at room temperature due to the thermal drift of the piezo-drivers. As was first demonstrated by Feenstra and coworkers [21], **STM** is capable of performing a chemical identification of atomic species based on their electronic contrast. Moreover, spin polarized **STM** have been implemented by Wiesendanger and coworkers to analyze ferromagnetic structures with the resolution beyond the exchange length (22); for a recent review, see the reference 23). Cross sectional (**X-STM**) employs the same principles of operation as a conventional **STM**. The only difference between these two techniques is that for **X-STM**, the sample surface is prepared by cleaving the sample. In this way, an absolutely clean atomically flat surface can be achieved without additional thermal treatments (except of a pre-cleavage annealing to obtain impurity and water desorption). Moreover, the structures that are covered by the capping layers can be reached (for example multilayers sample). The **X-STM** was pioneered by Salemink, Feenstra and coworkers. Johnson et al. were the first to observe charged impurities in *III – V* semiconductors [24]. The most important fundamental limitation is the limited amount of natural cleavage planes of materials and the surface contains a lot of terraces. For example, for the *III – V* semiconductors, such as *GaAs*, the **X-STM** experiments can be carried out on the {110} surfaces only.

4.6. Photoemission Spectroscopy (*PES*) and Photoelectron Diffraction (*PED*)

Photoemission spectroscopy (*PES*) is a useful technique to investigate the occupied electronic states in solids [25]. The *PES* utilizes the photoelectric effect when a solid is illuminated by photons and, if the necessary energy is transferred to the sample, the electrons are emitted from the solid. *PES* spectra are provided by measuring kinetic energy distribution of photo-electrons which escape from the solid through the surface and overcome the vacuum level E_V . Assuming that when light with photon energy $h\nu$ is illuminated on a solid, an electron with the binding energy E_B , which is referenced to the Fermi level E_F , is emitted with the kinetic energy E_V^{kin} , which is referenced to E_V . In this case, we can describe the relationship between E_B and E_V^{kin} using the energy conservation law:

$$E_V^{kin} = h\nu - \phi - E_B \quad [4.67]$$

where $\phi = E_F - E_V$ is the work function of the solid. The kinetic energy E^{kin} which is referenced to E_F is practically observed in *PES* measurements, thus the notation is rather simplified by:

$$E^{kin} = h\nu - E_B. \quad [4.68]$$

Schematic diagram of *PES* is shown in Fig. 4.18.

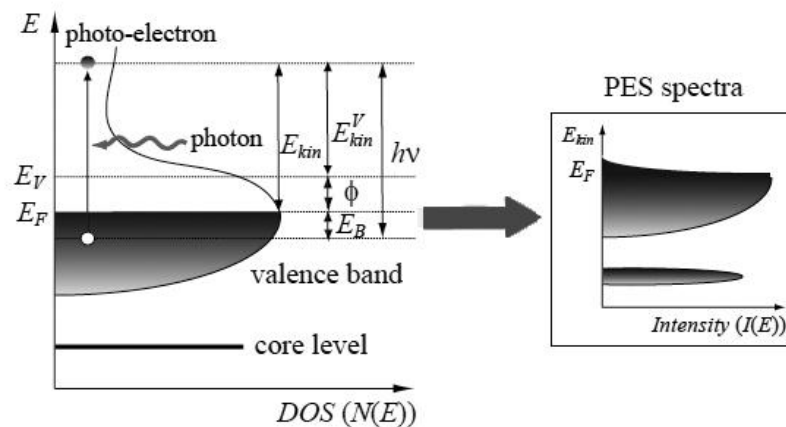


Fig. 4.18. Schematic diagram of photoemission spectroscopy. The density of states $N(E)$ is obtained by measuring the photoemission spectra $I(E)$.

The density of states (**DOS**) $N(E)$ is obtained by measuring the photoemission spectra $I(E)$, which are broadened by the resolution of light source and electron energy analyzer. In one electron approximation, the binding energy is equal to the negative Hartree-Fock orbital energy with Bloch wave number k :

$$E_B = -\epsilon_K \quad [4.69]$$

Here, *Koopmans' theorem* is used [26]. This assumption is valid when the wave functions of both the initial and final states can be expressed by the single Slater determinants of the n and $(n - 1)$ electron systems, respectively, and the one electron wave functions do not change by the removal of the electron. If we apply this approximation, the photoemission spectrum $I(E_B)$ can be expressed as:

$$I(E_B) \propto \sum_k \delta(E_B - \epsilon_K) \propto N(-E_B). \quad [4.70]$$

Thus, when the one-electron approximation is valid, the photoemission spectrum is proportional to the density of states of the occupied one-electron states $N(E)$. If the electron correlation effect is taken into account, one can no more consider the electron system within the one-electron picture, because the relaxation of the electron system influences the photoemission final state screening the generated holes by valence electron. Thus, the energy difference between the n electrons initial state energy E_n^i and the $(n - 1)$ electrons final state energy E_{n-1}^f provides the binding energy E_B , that is:

$$E_B = E_{n-1}^f - E_n^i. \quad [4.71]$$

Using Fermi's golden rules, the **PES** spectrum, which now corresponds to the single-particle excitation spectrum of the electron system, is expressed as:

$$I(E_B) \propto \sum_k |\langle \psi_{n-1}^f | a_k | \psi_n^i \rangle|^2 \delta[E_B - (E_{n-1}^f - E_n^i)], \quad [4.72]$$

where ψ_{n-1}^f and ψ_n^i denote the final and initial states, respectively, a_k is the annihilation operator of the electron occupying orbital k . Considering electron correlation effect, the finite lifetime of quasi-particle also contributes to the spectral broadening.

From the data reporting in Fig. 4.8, it is possible to note that around the electron energy of $2 - 1000 \text{ eV}$, typical of *PES* measurement, the escape depth is $5 - 10 \text{ \AA}$. This suggests that *PES* measurement is quite surface-sensitive.

4.6.1. Photoelectron Diffraction (*PED*)

Photoelectron diffraction is a method to determine the adsorption geometry of molecules or atoms which are physisorbed or chemisorbed on single crystal surfaces [27, 28]. The principle of photoelectron diffraction (Fig. 4.19) is comparable to the principle of optical holography: a "reference" electron wave and different "object" electron waves (which emerge from the reference wave being scattered at atoms in the substrate or the adsorbate) interfere in a suitable detector (analyzer). The electron source is an atom in the adsorbate: the electron wave is created by exciting a core hole electron with *X-ray* radiation. Part of it will reach the detector directly ("reference" wave) and other parts will get there after being scattered off other atoms ("object" waves). In the analyzer these different parts of the same electron wave interfere with each other. The intensity of the photoelectrons for a certain peak is determined as a function of azimuthal and polar angle.

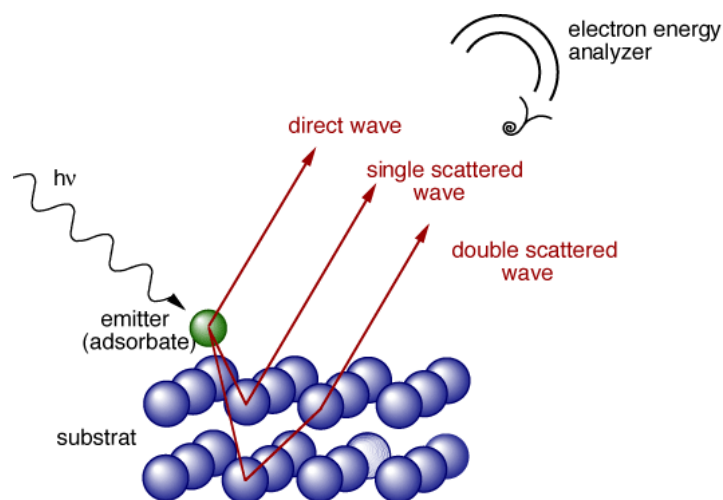


Fig. 4.19. Schematic picture of a photoelectron diffraction.

The intensity of the photoelectron peak can also be studied as a function of electron kinetic energy by changing the incident photon energy in synchrotron radiation experiments. The photoelectrons diffraction by the neighboring atoms can provide

information on the surface crystallographic structure. **PED** is a powerful tool to investigate a specific element; in fact the diffraction pattern corresponds to the element which emits the photoelectron. Therefore the nature of the surroundings of each element can be investigated in turn and depends on the energy of incoming photons.

A consideration of diffraction phenomena associated with the wave character of the emitted photoelectrons will prove essential for understanding the observed angular distributions. It is thus useful to introduce the appropriate non-relativistic relationship between photoelectron wavelength λ_e and kinetic energy E_{kin} :

$$\lambda_e = \frac{h}{\sqrt{2mE_{kin}}} \Rightarrow \lambda_e (\text{\AA}) = \sqrt{\frac{150}{E_{kin} (eV)}}. \quad [4.73]$$

The magnitude of the associated electron wave vector \vec{k} is in turn given by $k = 2\pi/\lambda_e$, and $\hat{k} = \vec{k}/k$. To describe the photoelectron diffraction it is useful to use the three steps model:

1. Photoemission;
2. Scattering;
3. Refraction.

In the first step when a photon strike the sample surface, it is produced the primary wave. In the photoemission we now use three approximation: dipole for radiation interaction ($\Delta l = l \pm 1$), central field for electronic interaction and frozen-core for excited ion final state. Then the generated wave encounters the neighbor atoms and a scattering phenomena occurs (in the simplest case a single scattering):

$$\psi(\vec{r}, \vec{k}) = \phi_0(\vec{r}, \vec{k}) + \sum_j \phi_j(\vec{r}, \vec{r}_j - \vec{k}) \quad [4.74]$$

where $\phi_0(\vec{r}, \vec{k})$ is the primary wave reaching the detector directly and ϕ_j are the amplitudes after several scattering processes. The wave function of the outgoing electron without any scatters is described applying the standard optical selection rules for the angular distribution ($l' = l \pm 1$ and $m' = m, m \pm 1$). The ϕ_j contains an important term the scattering factor $f_j(\vartheta_j)$; in fact it is possible to write:

$$\phi_j \propto f_j(\vartheta_j) \frac{e^{ik(\vec{r}-\vec{r}_j)}}{\vec{r} - \vec{r}_j} \quad [4.75]$$

where:

$$f_j(\vartheta_j) = \frac{1}{k} \sum_{l=0}^{\infty} C_l \sin \delta_l P_l(\cos \vartheta_j) \quad [4.76]$$

with $C_l = (2l + 1)\exp(i\delta_l)$, δ_l the phase shifts that determinate the scattering amplitude and $P_l(\cos \vartheta)$ the Legendre polynomials. In the third process, the refraction, we have the conservation of the component parallel to the surface of the wave vector ($k_{in}^{\perp} = k_{out}^{\perp}$). It is relevant also to take into account other two important effects: the electron inelastic scattering and the Debye-Waller effect. The first could be considered as a factor term $e^{-L/2\Lambda}$ where L is the path length and Λ is the inelastic mean free path. The Debye Waller correction is:

$$W_j(T) = e^{-\Delta k_j^2 \overline{U_j^2}(T)} = e^{-2k^2(1-\cos \vartheta_j) \overline{U_j^2}(T)} \quad [4.77]$$

where Δk_j^2 is the wave vector variation and $\overline{U_j^2}$ is the mean square displacement of atom j . Taking into account the above terms, it is possible to write the intensity detected by the analyzer (see Fig. 4.20 for the scattering geometry) [28]:

$$\begin{aligned} I(\vec{k}) \propto & \int \left| d\hat{\epsilon} \cdot \hat{k} e^{-L/2\Lambda} + \sum_j \frac{\hat{\epsilon} \cdot \hat{r}_j}{r_j} |f_j(\vartheta_j)| W_j e^{-L/2\Lambda} e^{i[kr_j(1-\cos \vartheta_j) + \psi_j(\vartheta_j)]} \right|^2 d\hat{\epsilon} + \\ & + \sum_j \int (\hat{\epsilon} \cdot \hat{r}_j)^2 \frac{|f_j(\vartheta_j)|^2}{r_j^2} (1 - W_j^2) e^{-L/2\Lambda} d\hat{\epsilon}. \end{aligned} \quad [4.78]$$

The first term is the primary wave, the second term is the scattered wave and the third term is a algebrical correction term for the Debye Waller factor obtained expanding the absolute value squared.

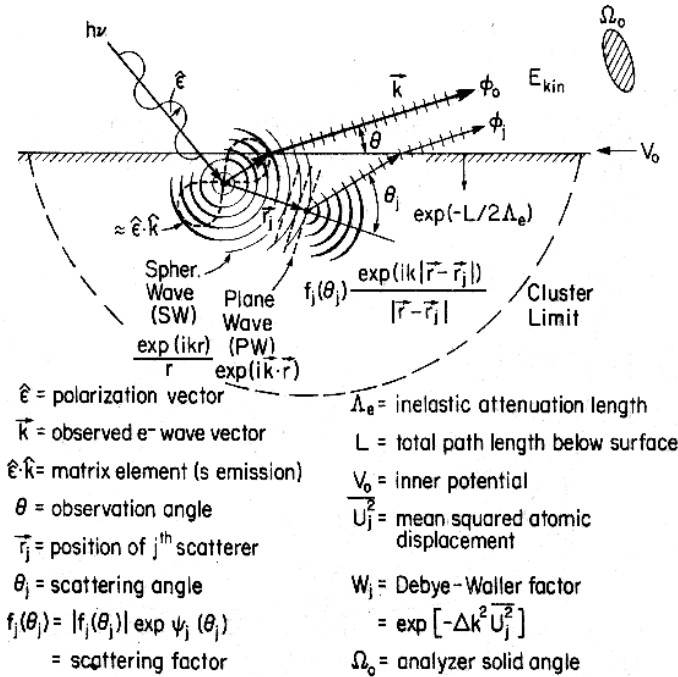


Fig. 4.20. Schematic illustration of the assumptions used in the single scattering cluster (SSC) model, with various important quantities defined [28].

To obtain the diffraction information, it is possible to calculate the surface anisotropy:

$$\chi = \frac{I(\vec{k}) - I_0}{I_0} \quad [4.79]$$

where I_0 is the background contribution. With the graphic of χ as a function of the polar angle we obtain the anisotropy of the surface and so the information of the surrounding of a specific element. Comparing the experimental result with calculated models, it is possible to verify the morphological structure of the sample.

4.7. Reflectivity Anisotropy Spectroscopy (*RAS*)

Optical methods are non destructive probes of solid surfaces and provide good energy resolution and the possibility of investigating the symmetry of the electronic states by using polarized light [29]. Within this class of techniques, Reflectivity Anisotropy Spectroscopy (***RAS***) is widely used to investigate the optical properties of solid surfaces in the visible and soft ultraviolet [30]. Typically, visible light penetrates 500 Å in the solid. If one considers a surface layer 5 Å, 0.1% of the signal is ascribed to the surface. In the ***RAS*** technique a light beam, alternatively polarized along two orthogonal directions (usually corresponding to high symmetry directions) is focused on a clean surface and the reflectivity change is measured. Two basic assumptions are made:

- the reflectivity difference originates solely from the anisotropy of the surface;
- the bulk is isotropic and does not contribute to the signal.

The *RAS* signal is given by

$$\left(\frac{\Delta R}{R}\right)_{RAS} = 2 \frac{R_x - R_y}{R_x + R_y} \quad [4.80]$$

where R_x and R_y are the reflectivity along the two directions of polarization.

A ***RAS*** experiment is performed using the apparatus schematically shown in Fig. 4.21. A monochromatic and linear polarized light beam crosses the photoelastic modulator (PEM), which rotates periodically the polarization plane, and is reflected by the sample on a photomultiplier. If the surface is anisotropic, the reflected signal has twice the modulation frequency of PEM and is measured by a lock in amplifier. The amplitude of the complex reflectivity change is given by the real part of the relative reflectivity change ($Re \frac{\Delta R}{R}$). It is also possible to measure the imaginary part of $\frac{\Delta R}{R}$ by using a second photomultiplier.

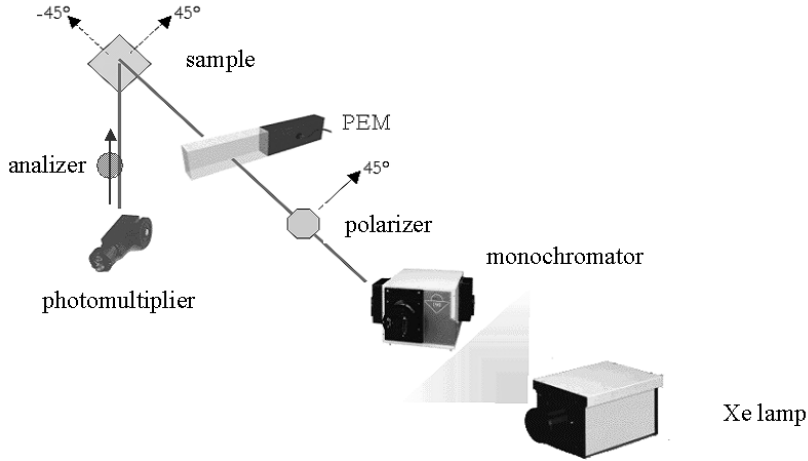


Fig. 4.21. Experimental RAS apparatus.

The differential reflectivity of a system consisting of a bulk (of complex dielectric function $\varepsilon_b = \varepsilon'_b + i\varepsilon''_b$), a surface layer (of thickness d and complex dielectric function $\varepsilon_s = \varepsilon'_s + i\varepsilon''_s$) and vacuum (McIntyre-Aspnes model) [32] is given by:

$$\frac{\Delta R}{R} = \frac{R_d - R_0}{R_0} = -\frac{8\pi d}{\lambda} \operatorname{Im} \frac{1 - \varepsilon_s}{1 - \varepsilon_b} = -\frac{8\pi d}{\lambda} \frac{(1 - \varepsilon'_b)\varepsilon''_s + \varepsilon''_b \varepsilon'_s}{(1 - \varepsilon'_b)^2 + (\varepsilon''_b)^2} \quad [4.81]$$

where R_d is the reflectivity with the surface layer, R_0 is the reflectivity without the surface layer, and λ is the wavelength of the light.

When applied to **RAS**, formula [4.81] gives:

$$\left(\frac{\Delta r}{r}\right)_{RAS} = 2 \frac{r_x - r_y}{r_x + r_y} = \frac{8\pi d n_m i}{\lambda} \frac{\varepsilon_{sx} - \varepsilon_{sy}}{\varepsilon_b - \varepsilon_m} \quad [4.82]$$

where r_x and r_y are the Fresnel coefficients, ε_{sx} and ε_{sy} are the dielectric functions along the two directions of polarization, and ε_m and n_m are the dielectric function and the refractive index of the medium, respectively (usually air or vacuum). By separating the real and imaginary parts one gets:

$$\operatorname{Re} \left(\frac{\Delta r}{r}\right)_{RAS} = -\frac{8\pi d n_m}{\lambda} \frac{\Delta\varepsilon''_s (\varepsilon_m - \varepsilon'_b) + \Delta\varepsilon'_s \varepsilon''_b}{(\varepsilon_m - \varepsilon'_b)^2 + (\varepsilon''_b)^2} = \frac{4\pi d n_m}{\lambda} (A\Delta\varepsilon''_s - B\Delta\varepsilon'_s) \quad [4.83]$$

$$\operatorname{Im} \left(\frac{\Delta r}{r}\right)_{RAS} = -\frac{8\pi d n_m}{\lambda} \frac{\Delta\varepsilon''_s \varepsilon''_b + \Delta\varepsilon'_s (\varepsilon_m - \varepsilon'_b)}{(\varepsilon_m - \varepsilon'_b)^2 + (\varepsilon''_b)^2} = \frac{4\pi d n_m}{\lambda} (B\Delta\varepsilon''_s - A\Delta\varepsilon'_s)$$

where $\Delta\varepsilon'_s$ and $\Delta\varepsilon''_s$ are the real and imaginary parts of the difference between the dielectric functions along the two directions of polarization.

The measured reflectivity is related to [4.83] by means of relation:

$$\frac{\Delta R}{R} = 2\text{Re}\left(\frac{\Delta r}{r}\right) \quad [4.84]$$

Knowing the bulk dielectric function, ε_b , and measuring $\text{Re}\left(\frac{\Delta r}{r}\right)$ and $\text{Im}\left(\frac{\Delta r}{r}\right)$ one obtains the surface dielectric function $\Delta\varepsilon_s$ from the solution of a linear system of equations. The A and B coefficients depend on ε_b and are calculated in Fig. 4.22 for a few semiconductors. B is practically zero below a threshold which depends on the material.

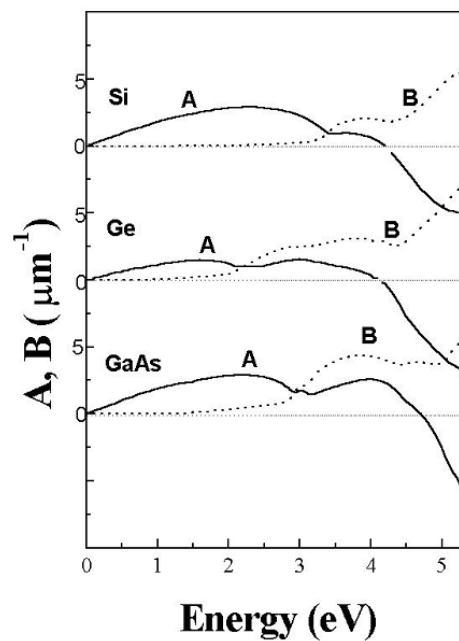


Fig. 4.22. A and B coefficients as a function of the photon energy. The threshold energy of B is about 3.2 eV for Si , 2.0 eV for Ge , 2.8 eV for $GaAs$ and 2.7 eV for GaP [31].

References.

- [1] M.A. Herman, H Sitter: *Molecular Beam Epitaxy-Fundamentals and Current Status* Springer Verlag, 1989; E.H. Parker *The Technology and Physics of Molecular Beam Epitaxy*, Plenum Press, 1985.
- [2] John R. Arthur *Surface Science* **500**, **189–217** (2002).
- [3] C.T. Foxon, B.A. Joyce: *Surf. Sci.* **50**, **434** (1975); *Surf. Sci.* **64**, **293** (1977).
- [4] P.A. Maki, S.C. Palmateer, A.R. Calawa, B.R. Lee *J. Electrochem. Soc.* **132**, **2813** (1985).
- [5] J.J. Harris, B.A. Joyce, P.J. Dobson *Surf. Sci.* **103**, **L90** (1981).
- [6] C.E.C. Wood *Surf. Sci.* **108**, **L441** (1981).
- [7] H. Luth *Solid Surfaces, Interfaces and Thin Films* Springer (2001).
- [8] J.B Pendry *Low Electron Energy Diffraction* Academic Press Inc, London 1974.
- [9] M. De Crescenzi and M.N. Piancastelli *Electron Scattering and Related Spectroscopies* World Scientific, Singapore (1996).
- [10] E. Placidi *PhD thesis (2002) Physics Department University of Rome Tor Vergata*.
- [11] D.L. Mills *Surf. Science* **48**, **59** (1975).
- [12] A. A. Lucas and M. Sunjic *Phys. Rev. Lett.* **26**, **229** (1971).
- [13] E. Evans and D.L. Mills *Phys. Rev. B* **5**, **4126** (1972).
- [14] E. Evans and D.L. Mills *Phys. Rev. B* **7**, **853** (1973).
- [15] F. Wooten *Optical properties of solids* Academic Press (1972).
- [16] H. Ibach, D. L. Mills *Electronic Energy Loss Spectroscopy and Surface Vibrations*, Academic (1982).
- [17] T. Hanaguri, C. Lupien, Y. Kohsaka, D. -H. Lee, M. Azuma, M. Takano, H. Takagi, and J. C. Davis *Nature* **430**, **1001** (2004).
- [18] E. W. Hudson, K. M. Lang, V. Madhavan, S. H. Pan, H. Eisaki, S. Uchida, and J. C. Davis *Nature* **411**, **920** (2001).
- [19] P. K. Hansma and J. Tersoff *J. Appl. Phys.* **61**, **R1** (1987).
- [20] J. A. Stroscio, W. J. Kaiser *Scanning Tunneling Microscopy* Vol. **27** Method of Experimental Physics Academic Press, Inc. (1993).

- [21] R. S. Goldman, R. M. Feenstra, B. G. Briner, M. L. Osteen, and R. J. Hauenstein *Appl. Phys. Lett.* **69**, **3698** (1996).
- [22] K. von Bergmann, M. Bode, A. Kubetzka, M. Heide, S. Blügel, and R. Wiesendanger *Phys. Rev. Lett.* **92**, **046801** (2004).
- [23] R. Wiesendanger, M. Bode, A. Kubetzka, O. Pietzsch, M. Morgenstern, A. Wachowiak, and J. Wiebe *J. Magn. Magn. Mater.* **272**.
- [24] M. B. Johnson, O. Albrektsen, R. M. Feenstra, and H. W. M. Salemink *Appl. Phys. Lett.* **63**, **2923** (1993).
- [25] S. Hüfner, *Photoelectron Spectroscopy* (Springer-Verlag, Berlin, 2003).
- [26] T. A. Koopmans *Physica* **1**, **104** (1933).
- [27] C. S. Fadley *Basic Concept of X – ray Photoelectron Spectroscopy* School on Synchrotron Radiation and Applications, Miramare – Trieste, Italy (2004).
- [28] C. S. Fadley *Prog. Surf. Sci.* **16**, **275-388** (1984).
- [29] G. Chiarotti, G Del Signore and S. Nannarone *Phys. Rev. Lett.* **16**, **1170** (1968); G. Chiarotti, S. Nannarone, R. Pastore and P. Chiaradia *Phys. Rev. B* **4**, **3398** (1971).
- [30] I. Kamiya, D.E. Aspnes, L.T. Florez, J. P. Harbison *Phys. Rev. B* **46**, **15894** (1992).
- [31] H. Luth, M. Buckel, R. Dorn, M. Liehr, R. Matz *Phys. Rev. B* **15**, **865** (1977); H. Ibach and J.E. Rowe *Phys. Rev. B* **9**, **1951** (1975).
- [32] J. D. E. McIntyre, D. E. Aspnes *Surf. Sci.* **24**, **417** (1971).

Chapter 5

Growth and characterization of $GaAs$ and $Ga_{1-x}Mn_xAs$

5.1. Introduction

The $Ga_{1-x}Mn_xAs$ electronic and morphological surface structure have not yet been well understood and the first stage of growth has to be studied for a better comprehension of this compound. Our attention was focused on the study of $GaMnAs$ surface and the aspects of the Mn interaction with $GaAs$ structure, because of the large improvement that this kind of material could bring to the spin injection, as pointed out in the introduction. We pointed our attention starting from the $GaAs(001)c(4 \times 4)$ reconstruction as it is widest one used in the industrial semiconductor production for its simple reproducibility. Therefore we studied the electronic and structural properties of $GaMnAs(001)(1 \times 2)$ surface, simultaneously performing **RAS**, **HREELS**, **XPS** and **STM** measurements on high quality samples, grown on $GaAs(001)c(4 \times 4)$ substrate by **MBE** and measured in **UHV** to avoid exposure to contamination.

In order to study the Mn interaction with $GaAs$, a clean $GaAs(001)c(4 \times 4)$ sample was grown by **MBE** and a post growth Mn deposition was performed with a further low temperature annealing ($250^\circ C$), replying the $GaMnAs$ **MBE** growth conditions; then **XPS**, **PED**, **XAS** measurements at the synchrotron facility in Trieste (Aloisa beamline - Elettra) and a further **STM** investigation were carried out.

In this section **MBE** $GaAs$ and $GaMnAs$ growth is described with a further structural and magnetic characterization by **XRD**, **TEM**, **EXAFS** and **MOKE**.

5.2. *GaAs* preparation

The reactor used for samples preparation was a commercial *MBE 32 RIBER* system (Fig. 5.1). It consists of a vacuum chamber equipped with a manipulator, a *RHEED* system and 7 effusion cells for evaporation of: *Ga*, *As* (2 cells), *In*, *Mn*, *Al* and *Si*. The inner chamber is surrounded by a cryogenic pumping system that increases the pumping speed from 500 *l/s* (ionic pump) up to 50000 *l/s*. Liquid nitrogen (*LN*₂) reduces, by means of cold panels, the heat exchange between the cells held at different temperatures. The temperature of a single cell is controlled by a *PID* controller that drives the power supply on the basis of the feedback signal coming from the thermocouples placed on the cell. The same controlling system is used to control the manipulator heater placed under the sample holder.

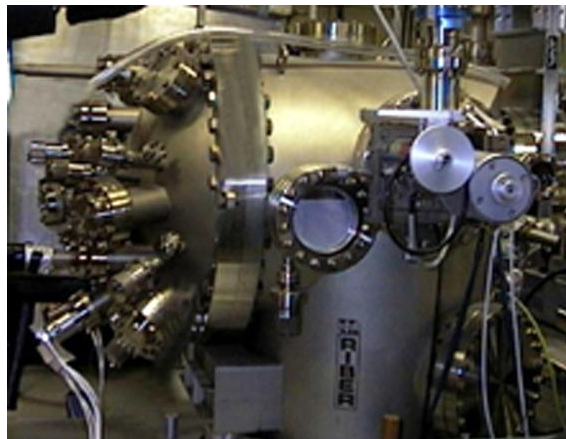


Fig. 5.1. The *MBE* reactor where it is possible to see the effusion cells, the manipulator and the fluorescent screen of *RHEED*.

As explained in Chapter 3 the *GaMnAs* grows in registry with *GaAs* substrate. For this reason we had to start the growth from a highly ordered *GaAs* surface. To obtain this kind of surface it is very important to produce a high quality *GaAs* film with *MBE*; we used a commercial epitaxial *n*-doped (*Si* doped $n = 10^{18} \text{ cm}^{-3}$) *GaAs*(001) substrate 600 μm thick that has been glued with *In* on a molybdenum holder (*moly-block*). The substrates are first inserted in an introduction chamber which is baked at 150 °C, they are subsequently degassed for about one hour at a temperature of 400 °C, in order to minimize the surface

contamination. Before placing the samples in the **MBE** chamber, the effusion cells are heated for a few hours with all the shutters closed (typically at a higher temperature than that used for the growth) in order to make them free from contaminants: usually $T_{Ga} = 1070\text{ }^{\circ}\text{C}$, $T_{Mn} = 680\text{ }^{\circ}\text{C}$ and $T_{As} = 270\text{ }^{\circ}\text{C}$. Before the growth of the samples, the oxide layer on the substrate surface was removed by heating the sample at $T_s = 630 \div 650\text{ }^{\circ}\text{C}$ under *As* flux. This de-oxidation procedure was monitored by **RHEED**, that showed a progressive transition from an amorphous diffraction pattern (oxidized surface) to a weak (2×4) pattern (completely deoxidized surface).

The *GaAs* growth parameters have been determined by measuring the **RHEED** oscillations as described in section 4.2.3. This calibration procedure is repeated every time the **MBE** chamber is opened for maintenance purposes; it is performed by positioning the video camera in front of the **RHEED** fluorescent screen and starting the recording of the **RHEED** spots intensity as a function of time (Fig. 5.2), contemporary to the opening of the *Ga* shutter. This has been done for several temperatures of *Ga* cell giving a calibration curve (Fig. 5.3).

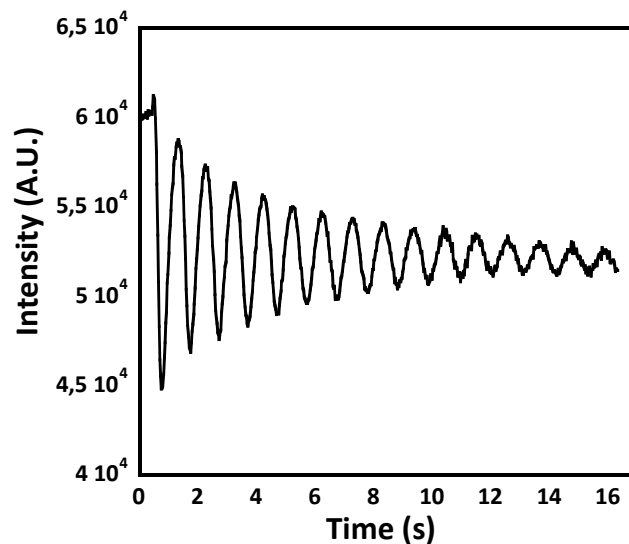


Fig. 5.2. **RHEED oscillation** with *As* cell at $T = 260^{\circ}$ and *Ga* cell at $T = 930^{\circ}$.

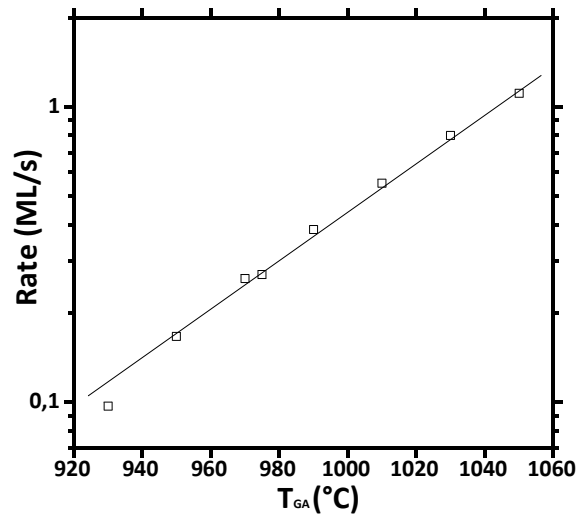


Fig. 5.3. *GaAs* growth rate in function of several temperatures of *Ga* cell.

Before starting the growth, the effusion cells temperatures were stabilized at a few degrees above the growth temperature values. After this procedure, *Ga* and *As* cells were set at $T_{Ga} = 1030$ °C and $T_{As} = 260$ °C; the temperature was stabilized for a few minutes, then the shutters were opened and the growth started. The pure *GaAs* films were grown with a substrate temperature T_s in the range $580 \div 600$ °C (the growth in this temperature range is referred to in the following as *High Temperature* growth), and flux ratio, J_{As}/J_{Ga} , \sim of 10. To obtain a good surface quality, a reduction of growth rate is recommendable as well as a rapid quenching. In this way an optimal (2×4) reconstruction is obtained improving the quality compared to a deoxidized surface as demonstrated by the **RHEED** patterns shown in Fig. 5.4, where it is possible to note the $\times 4$ periodicity in the $[\bar{1}10]$ azimuth direction (Fig. 5.4 (a)) and the $\times 2$ periodicity in the $[110]$ azimuth direction (Fig. 5.4 (b)).

The procedure for obtaining the $c(4 \times 4)$ surface, utilized as a starting surface for *GaMnAs* growth described in Chapter 3, is now illustrated: a layer with thickness of 400 nm was grown keeping the substrate at 660 °C, and the cells at $T_{Ga} = 1030$ °C and $T_{As} = 260$ °C. Cooling down the sample and keeping it at 500 °C under *As* flux, the sample undergoes a surface transition from (2×4) to $c(4 \times 4)$ as it was checked by **RHEED** in the $[100]$ surface direction (Fig. 5.5).

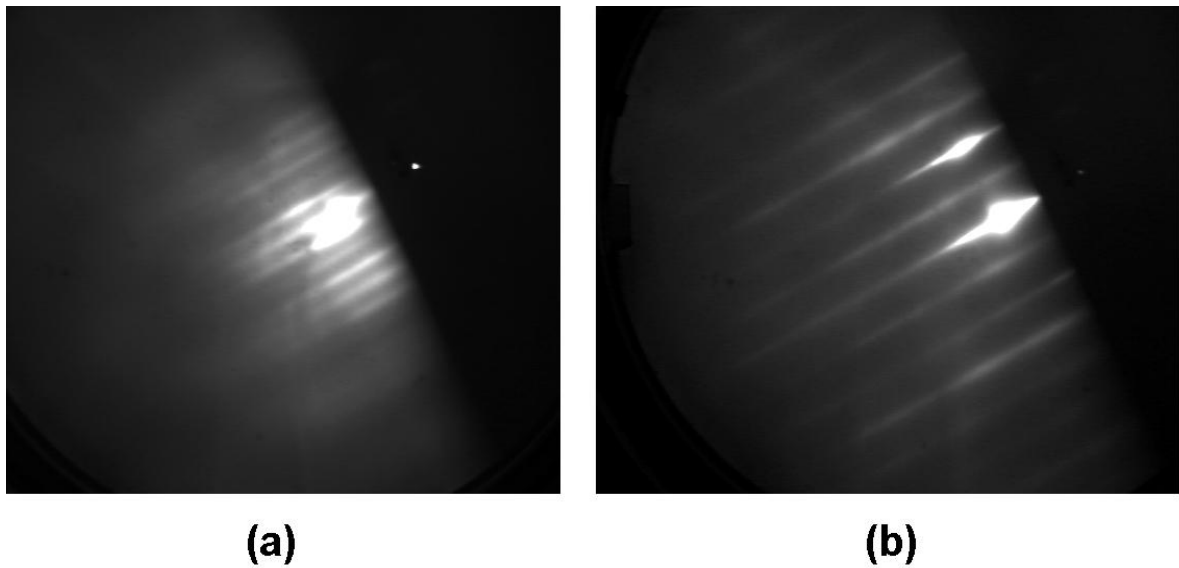


Fig. 5.4. **RHEED** pattern of $GaAs(001)(2 \times 4)$ surface in the $[\bar{1}10]$ azimuth direction (a) and in the $[110]$ azimuth direction (b).

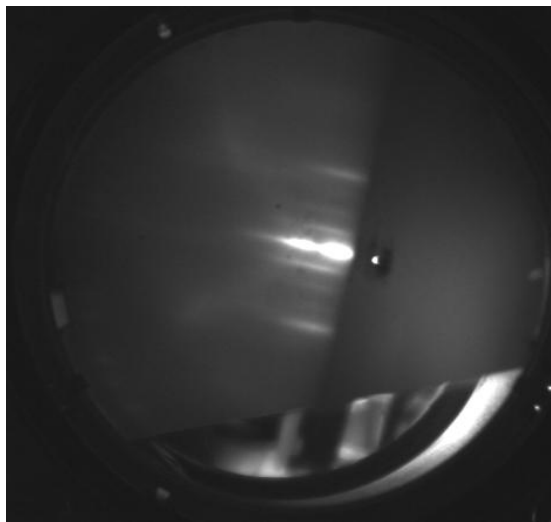


Fig. 5.5. **RHEED** pattern of $GaAs(001)c(4 \times 4)$ surface in the $[100]$ azimuth direction.

For the **STM** experiment³, both in the case of $GaMnAs(001)$ sample and $GaAs(001)$ sample with a post-growth Mn evaporation and annealing, a rectangular sample of substrate was glued on a **STM** sample holder (Omicron) and then mounted in a special *moly-block* which was modified in order to accept this sample holder (the growth procedures

³ The **STM** measurements were performed at Institute of Material Structure at National Council of Research (ISM - CNR) with an Omicron LT-STM.

was the same as the one described above). For this scope we realized a specifically designed mobile *UHV* chamber equipped with a ionization pump and a mechanical arm were Omicron system for sample holder transfers were mounted (Fig. 6.3). We used this special chamber to transfer the samples from the *MBE* apparatus to *STM* chamber avoiding air contamination and maintaining the sample in a background pressure in the order of 10^{-10} mbar. This procedure is much cleaner than the *As* capping as shown below.

Unfortunately at the synchrotron facility of Trieste, it was not possible to utilize the mobile chamber for the measurements. So it was necessary to protect the surface against oxidation with a capping layer. This has been done by growing a $0.5 \mu\text{m}$ thick cap of amorphous *As* using the following procedure: after the *GaAs* growth, the sample temperature was lowered to $T_s \approx -20^\circ\text{C}$ with *As* cell maintained opened; at this temperature the sticking coefficient drastically increases and *As* atoms are adsorbed on the sample surface starting the amorphous layer growth.

5.3. *GaMnAs* preparation

Before the $\text{Ga}_{1-x}\text{Mn}_x\text{As}$ growth, a *GaAs* buffer layer of approximately 400 nm was grown on a *GaAs*(001) substrate, in As_4 overflow at $\approx 590^\circ\text{C}$, and at a rate of $0.8 \mu\text{m}/\text{h}$. After 10 minutes of post-growth annealing under As_4 flux a $c(4 \times 4)$ reconstruction was obtained, then the substrate temperature was lowered to 270°C for $\text{Ga}_{1-x}\text{Mn}_x\text{As}$ deposition (*Low Temperature* growth); this growth conditions, as mentioned in Chapter 3, are necessary to avoid the formation of *MnAs* clusters (see Fig. 3.2) but, unfortunately, they favour the *As* antisites defects formation that degrade the magnetic properties of the material. $\text{Ga}_{1-x}\text{Mn}_x\text{As}$ layer was grown at the rate of $0.33 \text{ ML}/\text{s}$. The *Mn* amount in the compound is controlled by the effusion cell temperature T_{Mn} that varies in the range of $580 \div 620^\circ\text{C}$. During $\text{Ga}_{1-x}\text{Mn}_x\text{As}$ growth a clear two-dimensional asymmetric (1×2) reconstruction *RHEED* pattern was observed giving no indication of *MnAs* precipitates at the surface (no spotty *RHEED* pattern) (Fig. 5.6).

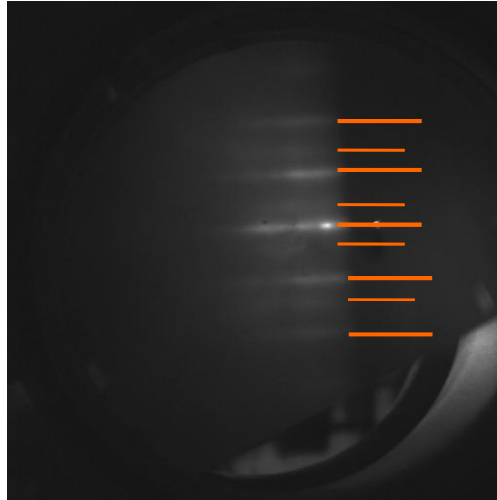


Fig. 5.6. **RHEED** pattern of $GaMnAs(001)(1 \times 2)$ surface in the $[110]$ direction.

Ga , Mn and As_4 fluxes were calibrated by an ion gauge placed at the substrate position. The *BEP* (beam equivalent pressure) for As_4 , Ga , and Mn was equivalent to a nominal Mn concentration of 1 %, which was estimated on the basis of fluxes ratios considering the sensitivity of each cell; we were forced to utilize this procedure as it was difficult to observe **RHEED oscillations** of $MnAs$ (for Mn rate calibration) in the case of growth with As_4 atoms (see section 4.2.1).

For the *in situ* electronic spectroscopies and **STM** measurements on the (001) surface, a special $GaMnAs$ sample was grown in *LT* growth procedure; this, unfortunately necessary for $GaMnAs$ growth, induces a lot of defects and the surface degradation increases proportionally to the sample thickness. In order to obtain the as best as possible surface quality, the thickness must be very small. For this reason we decided to grow 10 *ML* of $GaMnAs$ on a $GaAs$ buffer layer; this thickness value is the least necessary to observe the (1×2) reconstruction and to minimize the density of surface defects.

5.4. Magnetic characterization

The magnetic characterization of the $GaMnAs$ films was carried out by Magnetic Optical Kerr Effect (**MOKE**) measurements performed at the Max Plank Institute in Stuttgart (Germany) by the group leaded by Jan Honolka. **MOKE** consists of a rotation in the plane of

polarization of the light reflected from a magnetized material. In the longitudinal **MOKE** geometry, used in this measure, the field is parallel to both the reflecting surface and the plane of incidence. Linearly polarized light incident on the surface becomes elliptically polarized, with the change in polarization directly proportional to the component of magnetization; for our measure the magnetic field was parallel to the reflecting surface and to the plane of incidence. The **MOKE** technique allows also to study the magnetic anisotropy of the sample that is the energy dependence of the system which changes with the magnetization direction. Magnetic anisotropy is related to spin-orbit coupling, but it is often induced through mechanical stress (Magnetostrictive anisotropy). In *GaMnAs* compressive strain induces in plane easy axis, while tensile strain induces out of plane easy axis (like in the case of *InMnAs*) [1]. Within the plane there are two different observed anisotropies. The first one is a crystalline anisotropy according to the crystalline axis and the second one is a uniaxial anisotropy easy axis whose origins are still under debate. One theory states that it is due to the surface reconstruction of the *GaMnAs* layers during the growth [2]. The crystalline anisotropy has a four-fold symmetry with $[100]$ and $[010]$ being the easy axis while $[1\bar{1}0]$ and $[110]$ are the hard ones. The uniaxial anisotropy sets an easy axis in the $[1\bar{1}0]$ direction, while $[110]$ remains hard [2,3]. In these terms, the expression of the anisotropy energy of a *GaMnAs* single-domain magnet is:

$$E = (K_c/4)\cos^2 2\varphi + K_u \sin^2 2\varphi - MH\cos(\varphi - \varphi_H) \quad [5.1]$$

where φ is the angle between the magnetization (M) and a fixed crystallographic axes, φ_H the angle between the applied magnetic field and the same axis, H is the magnetic field, and K_c and K_u the crystalline and uniaxial anisotropy constants, respectively. For ferromagnetic *Ga_{1-x}Mn_xAs* in the range of $x = 0.02 \div 0.04$ the anisotropy constants depend on temperature in the following way [4]:

$$K_c \propto M^4(T); K_u \propto M^2(T) \quad [5.2]$$

This dependence implies that with increasing temperature (M becomes smaller approaching T_c), K_c will decrease much faster than K_u , allowing uniaxial anisotropy to become dominant at some determined temperatures. In Fig. 5.7 it is possible to observe the energy as a

function of the angle; the minima correspond to the magnetization easy axis; the curve is obtained qualitatively from the value of M measured in function of the angle φ . K_c and K_u have the dimension of erg/cm^3 .

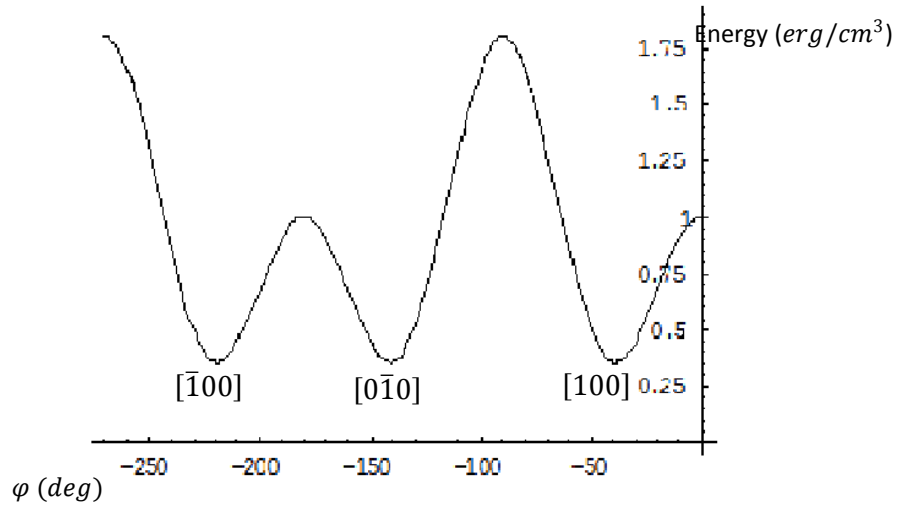


Fig. 5.7. Energy of a single magnetic domain as a function of the angle. The minima correspond to the easy axis of magnetization.

MOKE measurements at low values of magnetic field were used to investigate the shape of the hysteresis loop and coercive fields in function of temperature. With increasing temperature the thermal energy progressively disrupts the ferromagnetic order until it is completely lost at the Curie Temperature. Therefore the value of the coercive field, which reflects the extent of ferromagnetic order, is expected to decrease with increasing temperature. Fig. 5.8 shows the hysteresis loop for a sample with $x = 2\% \div 4\%$, measured at different temperatures.

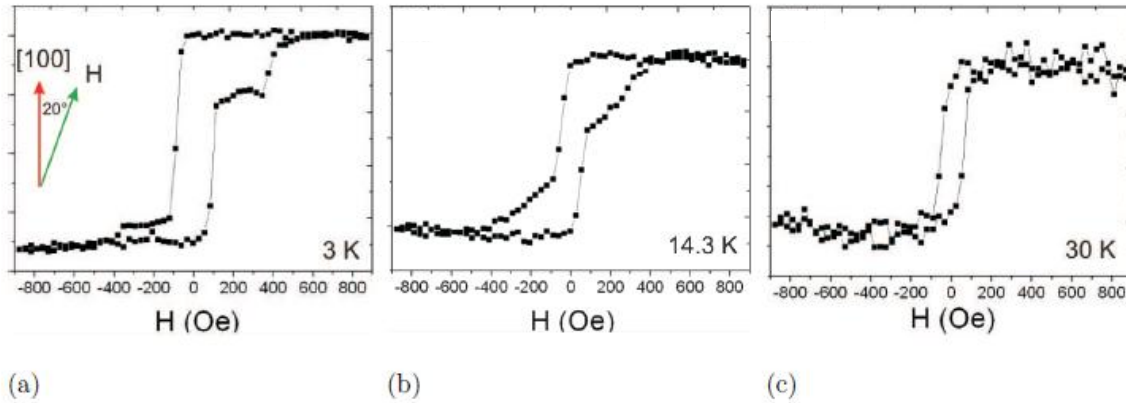


Fig. 5.8. Hysteresis loops for the magnetic field applied 20° with respect to the $[100]$ direction at (a) 3K , (b) 14.3K , (c) 31K in a sample with $x = 2 \div 4$.

Therefore the competition between uniaxial and crystalline anisotropies is well visualized, since the behavior of the system changes dramatically with increasing temperature. The two-steps reversal changes to a direct transition due to the increasing dominance of the uniaxial anisotropy. At 30K (Fig. 5.8(c)) the hysteresis loop starts to disappear indicating that the temperature is around the T_c .

On the same sample a magnetoresistive measurements were performed after the surface preparation for the ohmic contact (Fig. 5.9). The results, shown in Fig. 5.9, reveal a hump around 38K ; this behavior, that occurs at the T_c , is due to the critical scattering, in which carriers are scattered by magnetic fluctuation through exchange interaction [5]. *MnAs* compound has a room temperature T_c , so this value range of T_c confirms the absence of *MnAs* clusters.

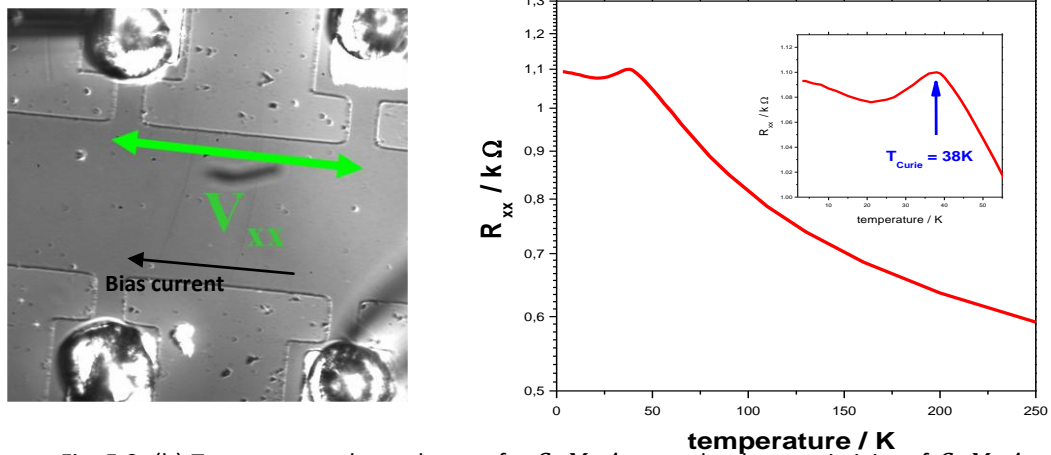


Fig. 5.9. (b) Temperature dependence of a *GaMnAs* sample plane resistivity of *GaMnAs*. The hump (marked by an arrow in the inset) is a characteristic at T_c transition. (a) The resistivity was measured by four contacts geometry acquiring the potential (V_{xx}) varying the bias current.

5.5. Structural characterization.

In order to directly measure the *Mn* content in the samples a *X-ray* Diffraction (*XRD*) characterization has been done. The determination of the *Mn* content is based on the fact that the lattice constant of *GaMnAs* depends on the *Mn* concentration (x) according to Vegard's law. The lattice constant of *GaAs* is smaller than the *GaMnAs* one; in the last compound a reduction of the plane and an expansion on the perpendicular direction of the cubic cell is generated and a consequent compressive strain occurs. This structural behavior corresponds to the presence of two peaks in the *X-ray* diffraction spectra as shown below, leading to the generation of a magnetic feature with a strong out of plane uniaxial hard axis. The diffraction pattern of the *GaAs* substrate (red) and the *GaMnAs* samples with different thickness ($40\mu\text{m}$ (black)– $200\mu\text{m}$ (green)– $400\mu\text{m}$ (blue)) are shown in Fig. 5.10.; if the sample is thin the interferences fringes are observed. In *GaMnAs/GaAs* systems the diffraction profiles typically show two peaks around the (004) reflection, which correspond to *GaAs* and *GaMnAs*, respectively. The spacing between these two peaks shown in Fig. 5.10 is a function of a_{GaMnAs} according to Vegard's law. These results confirm the high crystallographic quality of the deposited *GaMnAs*.

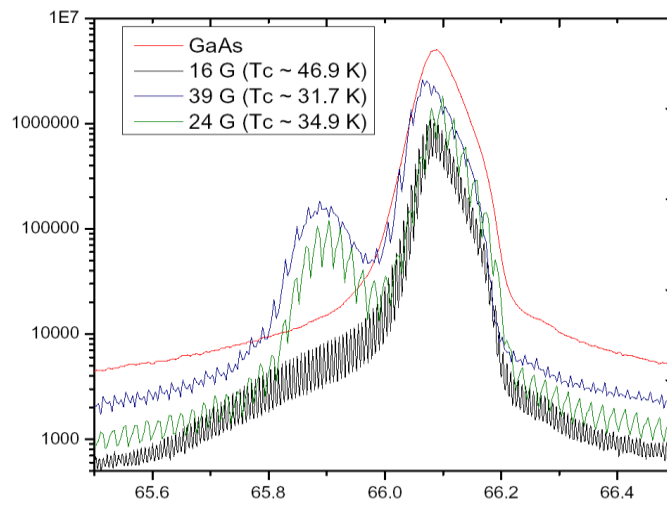


Fig. 5.10. Diffraction pattern of 3 *GaMnAs* samples and *GaAs* showing two distinctive peaks which correspond to *GaAs* and *GaMnAs*, respectively. The spacing between these two peaks is a function of the *Mn* content.

The crystalline quality of the *GaMnAs* samples used in this thesis work is also confirmed by a cross section **TEM** measurement⁴ performed in the *Mn* rich area of the sample. Fig. 5.11 shows the **TEM** image; it is possible to observe the atomic periodicity with oblique lines and the low presence of defects that confirms the high quality of the lattice. The brighter areas are typical of very thin sample prepared for **TEM** measurement.

⁴ Performed at Max Planck Institute – Stuttgart.

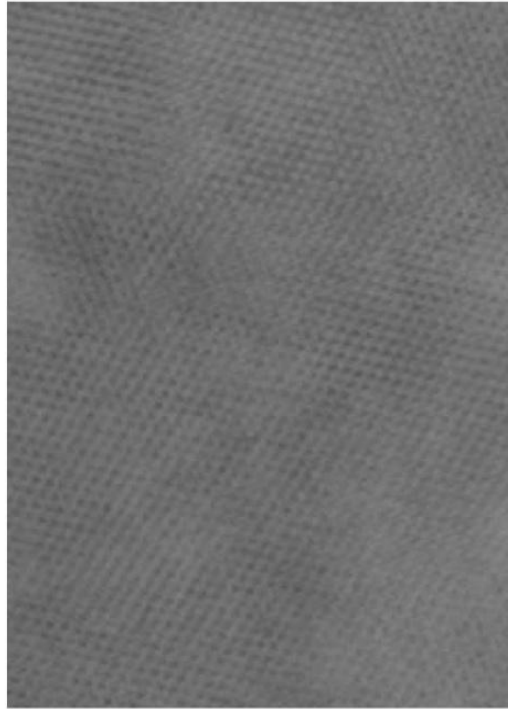


Fig. 5.11. **TEM** of *GaMnAs* sample with $T_c \approx 35K$ showing the high quality of crystalline structure.

Extended *X – ray* Absorption Fine Structure (**EXAFS**⁵) measurements were performed to characterize the *Mn* incorporation sites and exclude the presence of *MnAs* inclusions in a *GaMnAs* sample representative of the samples prepared in this work. In this particular case the sample used for measurement was the same of the one utilized in the **MOKE** measurement with a well defined T_c . **EXAFS** spectroscopy is a powerful investigation tool in this context characterized by a chemical selectivity and high resolution in the determination of the local structure around the absorbing element. In addition, the **EXAFS** spectroscopy is sensitive to ordered and disordered atomic structures, thus being complementary to *X – ray* diffraction.

⁵ **EXAFS** is the oscillating part of the X-ray Absorption Spectrum (**XAS**) that extends to about 1000 eV above an absorption edge of a particular element of a sample (*Mn* in our case). Electrons are knocked out of an atom when the energy value of incident X-rays surpasses the ionization threshold (the edge energy). The interference of these outgoing photoelectrons with the scattered waves from atoms surrounding the central atom causes **EXAFS**. The regions of constructive and destructive interference are respectively seen as local maxima and minima giving rise to the oscillations in **EXAFS**. **EXAFS** gives us information about distances between central and neighboring atoms; the number of neighboring atoms; the nature of neighboring atoms (their approximate atomic number) and changes in central-atom coordination with changes in experimental conditions

In the ideal $GaMnAs$ structure all Mn atoms occupy the Ga sites in a substitution configuration (Mn_{Ga}). However, due to the low growth temperature Mn could be incorporated in interstitial sites. Two possible interstitial sites are possible in the $GaAs$ structure: the octahedral site in the center of $GaAs$ fcc cell coordinated by four Ga atoms and the As coordinated tetrahedral site. However, as demonstrated by theoretical works, the tetrahedral site results energetically favored with respect to octahedral one, then we have not considered this last configuration in the **EXAFS** analysis [6]. The possible Mn sites in the $GaAs$ crystal structure are shown in Fig. 5.12.

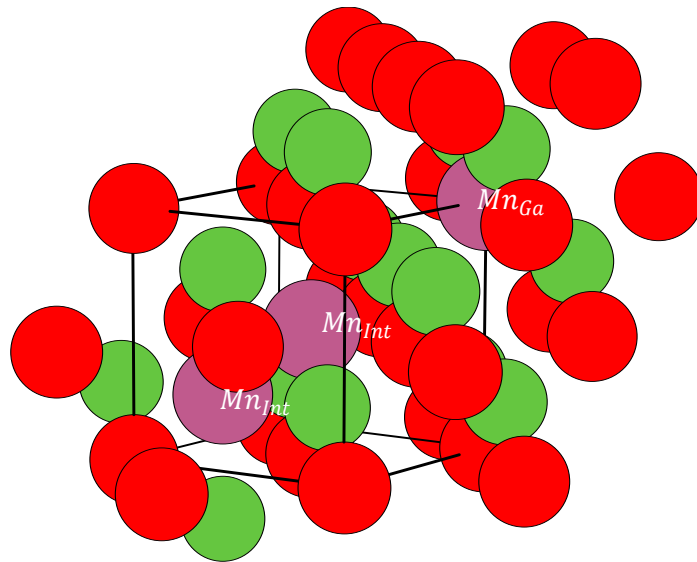


Fig. 5.12. $GaMnAs$ zincblende structure. The red balls are Ga atoms, the green ones are the As atoms with substitutional (Mn_{Ga}) and interstitials (Mn_{int}) Mn as labeled.

The **EXAFS** experiment was performed at the beam line Gilda at ESRF synchrotron (Grenoble – France) on a sample of $GaMnAs$. For the experimental setup the monochromator was equipped with a pair of $Si(111)$ crystals and was run in dynamical focusing mode. Harmonics rejection was achieved by using a pair of Pd –coated mirrors with incidence angle of 3.3 mrad and additionally by detuning the crystals at 80% of the rocking curve maximum. Data were collected in the fluorescence mode at the $Mn - K$ edge using a 13 –element hyper pure Ge detector and normalized by measuring the incident beam with an ion chamber filled with nitrogen gas. Measurements were carried out at 80 K

in order to minimize thermal disorder. For each sample each energy point was integrated for 15 s and six spectra were collected and averaged to improve the signal-to-noise ratio. In Fig. 5.13 is reported the average absorption spectrum before the background subtraction.

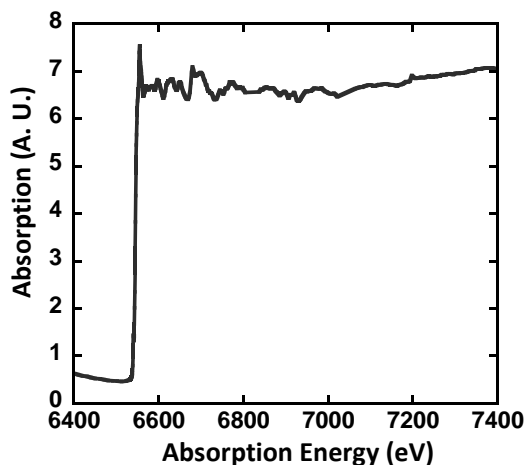


Fig. 5.13. Absorption of *GaMnAs* at *Mn* – *K* edge before background subtraction.

The **EXAFS** oscillations, $\chi(k)$, were extracted from the raw data with the *VIPER* code [7] and are reported in Fig. 5.14. The pre-edge background was subtracted with a polynomial function whereas for the post-edge background removal n cubic splines, with n a variable number of nodes, was used. The Fourier Transform (*FT*) of the $\chi(k)$ was performed in the range $k = 2.4\text{--}13 \text{ \AA}^{-1}$ using a Hanning window and a k^2 weight (Fig. 5.15). Three main peaks in the *FT* are present; each of these peaks is predominantly originating from the first three coordination shells around *Mn*. Sample of *Mn* in interstitial site exhibits a completely different *FT* line shape, with only one peak, which exhibits a slight asymmetry towards high values of the interatomic distance [8]. With this first qualitatively analysis it is possible to argue that in our sample we do not observe a shoulder at high values of R indicating *Mn* is mainly incorporated in the substitutional configuration.

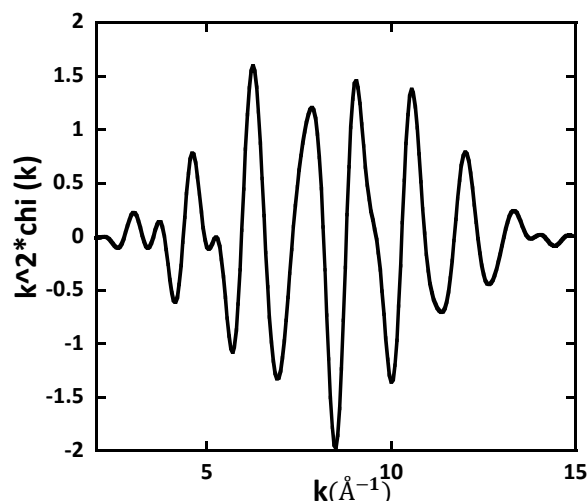


Fig. 5.14. *EXAFS* of *GaMnAs* at *Mn – K* edge after background subtraction.

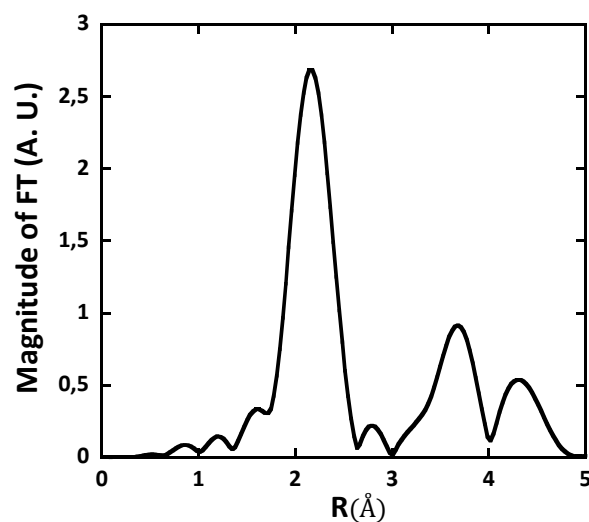


Fig. 5.15. Fourier transforms of the *EXAFS* spectra.

Data were quantitatively analyzed with the **ARTEMIS** program based on the **IFEFFIT** code [9]. Fitting was performed following a *FT* (the parameters of which have been described above) and in the *R* range $R = 1.65 - 4.5 \text{ \AA}$. The theoretical phase and scattering functions used in the fitting of the experimental data were calculated *ab initio* with the FEFF 8.1 code using muffin tin potentials and the Hedin-Lundqvist approximation for the energy-dependent part. We considered a cluster derived from the ideal *GaAs* structure (Spacegroup $FM\bar{3}M$, lattice parameter $a = 5.6537 \text{ \AA}$) and *Mn* was simply substituted to a *Ga* atom (tetrahedral substitutional) site coordinated by *As* (Fig. 5.12) and the related photoelectron scattering paths were calculated. The fit extends up to the third coordination shell.

Structural fitting parameters were the coordination number N_i , the bond length R_i , and the Debye-Waller factor σ_i^2 , i for each i – th coordination shell, whereas a common edge shift ΔE_0 and overall amplitude parameter S_0^2 were used. The coordination numbers were fixed ($N_1 = 4$, $N_2 = 12$, $N_3 = 12$). The experimental $\chi(k)$ and the related Fourier transform are reported in Fig. 5.16 along with the result of the fitting procedure. The numerical results of free parameters in the fit are reported in Tab. 1. From these results we observe an expansion of the first shell coordination distance of about 2% with respect the *GaAs* host structure whereas the second and third shells coordination distances are the same as the *GaAs* crystal structure within the experimental error. This behavior demonstrates that the structural deformation around the *Mn* impurities is limited to the first coordination distance as observed in previous **EXAFS** characterizations of the Mn_{Ga} sites in *GaAs* reported in literature [8, 10].

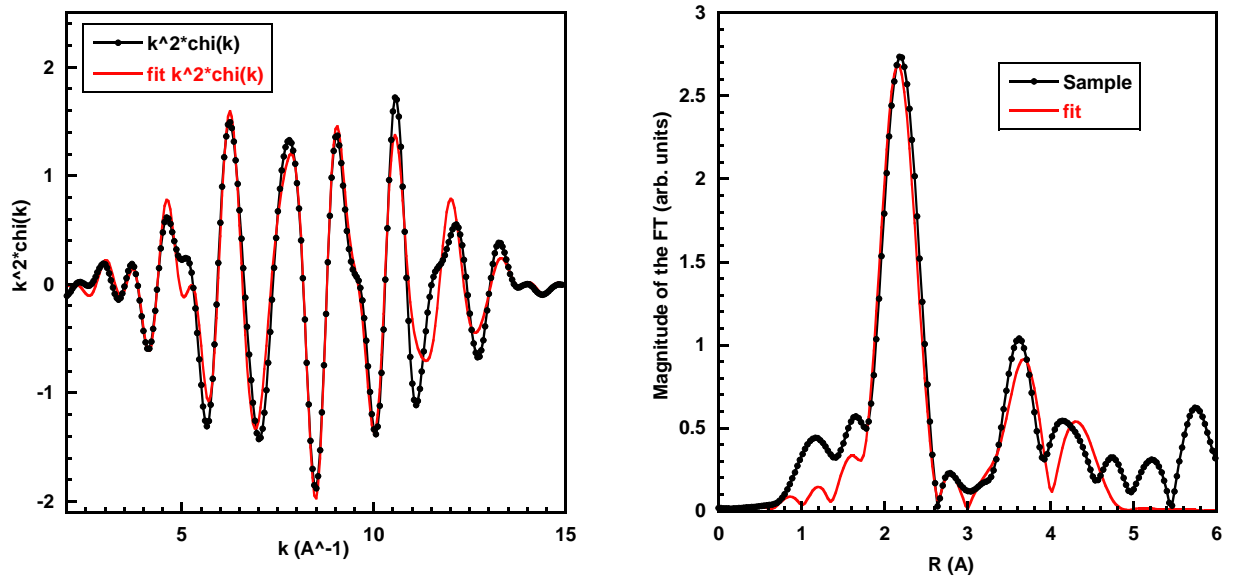


Fig. 5.16. [left] **EXAFS** spectra measurement and the best fit; the blue spectra is the residual between experimental data and fit; [right] Fourier Transform of the **EXAFS** data and relative best fit.

ΔE_0 (eV)	S_0^2	R_1 (\AA)	σ_1^2 (\AA^2)	R_2 (\AA)	σ_2^2 (\AA^2)	R_3 (\AA)	σ_3^2 (\AA^2)
± 0.5	± 0.2	± 0.01	± 0.001	± 0.01	± 0.003	± 0.02	± 0.006
2.5	0.9	2.49	0.004	4.02	0.011	4.65	0.012

Tab. 1. Fits parameters results for three coordination shells.

The fits results shown in Fig 5.19 and Tab. 1 reveal that the experimental data are nicely reproduced by the structural model of the *Mn* substitutional in the *GaAs* crystal structure. In particular, the high *R* side of the first coordination peak is perfectly reproduced by this model, indicating that the amount of interstitial *Mn* in the samples used in this work is far below the detection threshold of the **EXAFS** technique. It has to be noted that the third coordination shell is not well reproduced by the fit. Probably, this could happen because we do not consider multiple scattering and also because of the noise in the **EXAFS** spectra due to the low *Mn* concentration. The **EXAFS** characterization demonstrates that the transport and magnetic properties reported above are related to a pure diluted magnetic *GaMnAs* semiconductor alloy and are not biased by double donor *Mn* sites (interstitial) or ferromagnetic *MnAs* aggregates.

References.

- [1] H. Ohno, et al., *Proceedings of the 23rd. International Conference on the Physics of Semiconductors* (Berlin, Germany, July 21-26, 1996, Eds. M. Scheffler and R. Zimmermann, World Scientific, Singapore, 1996) **pp. 405-408.**
- [2] U. Welp, V. K. Vlasko-Vlasov, A. Menzel, H. D. You, U. Welp, V. K. Vlasko-Vlasov, A. Menzel, H. D. You, and T. Wojtowicz *Appl. Phys. Lett.* **85, 260 (2004).**
- [3] K.-Y. Wang, M. Sawicki, K. W. Edmonds, R. P. Campion, S. Maat, C. T. Foxon, B. L. Gallagher, and T. Dietl *Phys. Rev. Lett.* **95, 217204 (2005).**
- [4] H. B. Callen, E. Callen *J. Phys. Chem. Sol.* **27, 1271 (1966).**
- [5] Hideo Ohno *J. Magn. Magn. Mat.* **200, 110-129 (1999).**
- [6] K.W. Edmonds, P. Bogusławski, K.Y.Wang, R. P. Campion, S. N. Novikov, N. R. S. Farley, B. L. Gallagher, C.T. Foxon, M. Sawicki, T. Dietl, M. Buongiorno Nardelli and J. Bernholc *Phys. Rev. Lett.* **92, 037201 (2004).**
- [7] K.V. Klementev, *J. Phys. D: Appl. Phys.* **34, 209-17 (2001).**
- [8] F. d'Acapito, G. Smolentsev, F. Boscherini, M. Piccin, G. Bais, S. Rubini, F. Martelli and A. Franciosi *Phys. Rev. B* **73, 035314 (2006).**
- [9] M. Neville, B. Ravel, D. Haskel, J. J. Rehr, E. A. Stern, and Y. Yacoby, *Physica B* **208-209, 154 (1995).**
- [10] R. Bacewicz, A. Twaróg, A. Malinowska, T. Wojtowicz, X. Liu, J. K. Furdyna *J. Phys. Chem. Sol.* **66, 2004–2007 (2005).**

Chapter 6

GaMnAs(001) and *Mn/GaAs*(001) surface characterization

6.1. Introduction

Despite the importance of *GaMnAs* for its potential use in the field of spintronics, as described in Chapter 1, *in situ* surface optic and electronic measurements on this compound are almost lacking in literature. The study of the surface is important because the zincblende structure of *GaMnAs* favours the adsorption of *Mn* atoms in the interstitial site beneath the *As* surface dimers [1]; however the presence and the nature of surface dimers in *GaMnAs* has not yet been investigated. Comprehension of the interaction mechanism between *Mn* and the *GaMnAs* surface is of deep importance for the optimization of the growing process of the material itself. Furthermore, it has been observed that *GaMnAs* films obtained through the δ –doping technique, in which single layers of *Mn* are incorporated in the *GaAs* structure, presents magnetic properties comparable to the ones of the *GaMnAs* bulk material. The above remarks indicate that the interaction of *Mn* with the semiconductor surface leads to incorporation of the metal in the zincblende structure [2].

The *GaMnAs* bulk electronic structure is characterized, as clearly shown by transport and **ARPES** measurements [3, 4], by the presence of an impurity band having low *Mn* concentration⁶; it should be noted that *Mn* atoms interacts with *As* atoms producing a $p - d$ hybrid state⁷. The study of how the bulk electronic structure influences the surface electronic structure and the surface states of *GaMnAs* may be useful in the development of

⁶ The band is formed when *Mn* acceptors states expand over several unit cells and the number of unit cells is proportional to doping.

⁷ Hybridization explains the antiferromagnetism between *Mn* and *As* atoms [15] and the subsequent ferromagnetism between *Mn* atoms.

prototype devices based on *GaMnAs* in which it is necessary to form an interface between different semiconductors [5]. These observations are an essential pre-requisite for a more in-depth study of the morphology and of the electronic structure of the *GaMnAs* (001) surface growth. An accurate investigation may provide additional indications on the adsorption site of *Mn* in the matrix of *GaAs* and on possible electronic interactions with the matrix itself.

In the first part of this Chapter, the results of combined **RAS** and **EELS in situ** measurements and of photoemission and **STM** measurements performed on *GaMnAs*(001) films grown by **MBE** are described. Then a study of *Mn* deposited on the *GaAs* surface using photoemission with synchrotron radiation, photoelectron diffraction and morphological measurements with **STM** is reported. In the second part of this Chapter, to investigate the interaction between *Mn* and *GaAs*, a detailed study of *Mn* evaporated on the *GaAs*(001) surface under the same conditions of the **MBE** growth is presented.

6.2. Experimental results on the *GaMnAs*(001) surface

The **MBE** chamber (RIBER 32), for the growth of *III – V* compounds, described in the previous chapter is a vacuum chamber connected to an analysis chamber for **XPS** and **HREELS** measurements (Fig. 6.1). The latter is equipped with an electron gun, an electron monochromator, a Concentric Hemisphere Analyzer (**CHA**) and a **LEED**. To allow **RAS** measurements, a Bomco window (strain-free to minimize spurious optical anisotropies) is installed on the analysis chamber

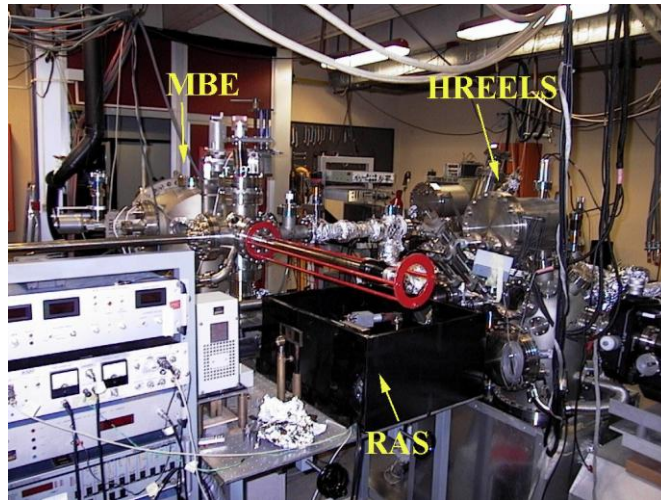


Fig. 6.1. Experimental set-up comprising the **MBE** reactor and, sectioned with valves, the **EELS**, **XPS** and **RAS** apparatuses for electronic and optical spectroscopy.

The **HREELS** apparatus (VG instrument) is installed in a *UHV* μ -metal chamber to reduce the strength of the earth magnetic field on the electron beam. The geometry is fixed, the electron monochromator and the analyzer (VG clam 100) forming an angle of 90° . Thus, in reflection geometry, the incidence angle between the beam and the sample is 45° (Fig. 6.2).

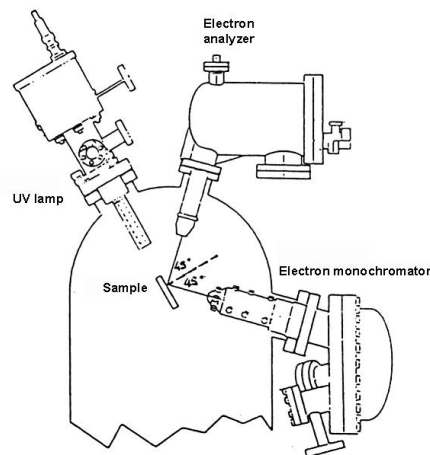


Fig. 6.2. **HREELS** apparatus.

The monochromator is a Concentric Hemispherical Analyzer (*CHA*) with a mean radius of $R_0 = 50 \text{ mm}$ that selects the electron energy with a resolution of about 10 meV in the $0 - 50 \text{ eV}$ range. A focusing system made of a quadrupole stage for the beam correction in the x and y directions, is coupled to the monochromator. Electrons of kinetic energy, E_k , at

the entry slit of the analyzer, undergo the voltage $-E_k + E_{pass}$ (E_{pass} stands for pass energy). After crossing the analyzer, the electrons are accelerated to E_k by means of a potential $E_k - E_{pass}$ and detected by a channeltron. The voltage V between the hemispherical electrodes is linked to the pass energy, E_{pass} , by the following equation [7]: $eV = E_{pass} (R_2/R_1 - R_1/R_2)$ where R_1 and R_2 are the internal and external radius of the hemispheres, respectively; varying V it is possible to select the energy of electrons to be analyzed. The relative resolution [7, 8] is given by the equation $\Delta E/E_{pass} = \Delta r/2R_0 + \alpha^2/4$, where Δr is the slit width (4, 2, 1 and 1/2 mm both for entrance and exit slits), R_0 is the mean radius of the hemispheres and α is the entry angle of electrons. Once fixed the geometry, the relative resolution is constant and the absolute resolution depends on the value of E_{pass} . The acquisition system is interfaced to a computer by means of two National Instrument boards: the counter board and the digital I/O board. The acquisition software controls all the scan parameters while the parameters related to the optimization of the signal (electrostatic lenses and magnetic trimmers) are set manually.

The **STM** experiments were carried out using a low temperature STM (Omicron LT-STM) housed in a vacuum chamber having 5×10^{-11} mbar base pressure equipped with a **LEED** and a mobile chamber (Fig. 6.3).

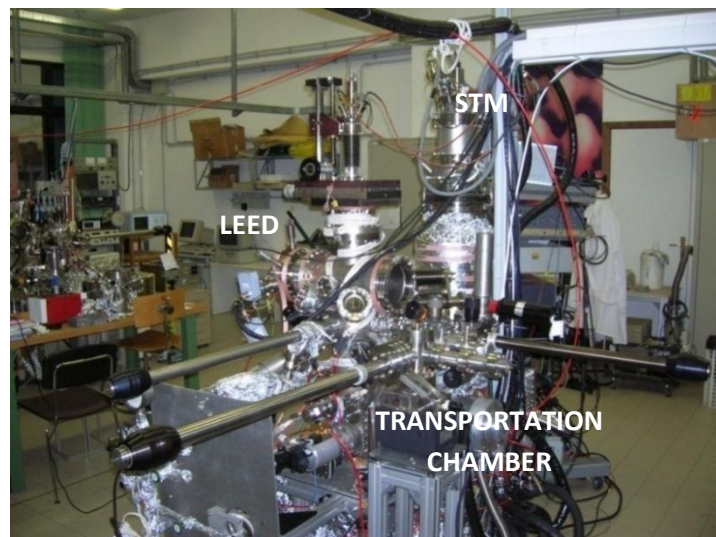


Fig. 6.3. Apparatus for **STM** measurements.

6.2.1. Experimental results

Firstly, in order to check the quality of the *GaMnAs* surface, **XPS** valence band spectra of *GaMnAs* (shown in Fig. 6.4) have been collected using the *Al K α* (1486.6 eV) line as X –ray source and the hemispheric CLAM 100 detector.

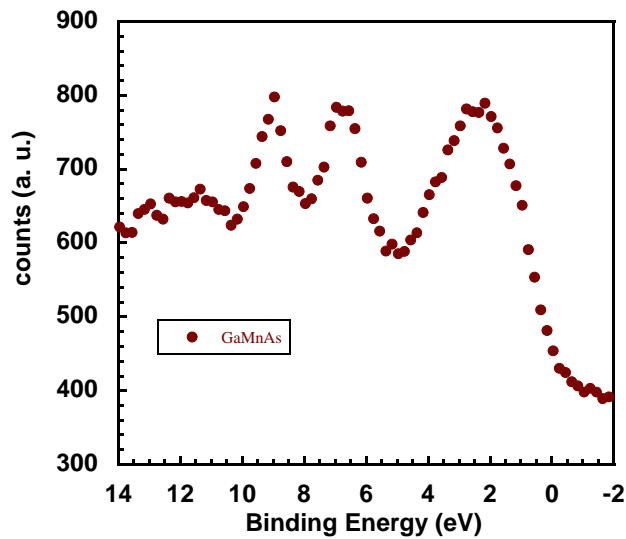


Fig. 6.4. **XPS** spectra of *GaMnAs*. The spectra is normalized to *Ga 3d* peak at 18.7 eV.

As explained in ref. [9], the intensity of the peak centred at 2 eV is attributed to the presence of hybrid (*p – d*) states confirming the presence of *Mn* and the high quality of *GaMnAs* layer [10].

In order to study the anisotropy of the *GaMnAs*(001) surface, in which the reconstruction is known (but not the structure of the reconstruction itself), a **RAS** spectrum in the 1.5 – 5.5 eV energy range is obtained. The **RAS** spectrum, measured *in situ* on the *GaMnAs*(001) sample immediately after the **MBE** growth, is shown in Fig. 6.5. From a preliminary analysis, it appears that the shape of the spectrum is similar to that of the **RDS** spectrum (reflectance difference spectroscopy) obtained on a clean *GaAs*(001) surface with (1 × 2) reconstruction [11]. This reconstruction is achieved after deposition of 1.75 *ML* of *As* on the surface of *GaAs*(001)*c*(4 × 4) and shows a disordered *c*(4 × 4) surface with the presence of *As – As* dimers.

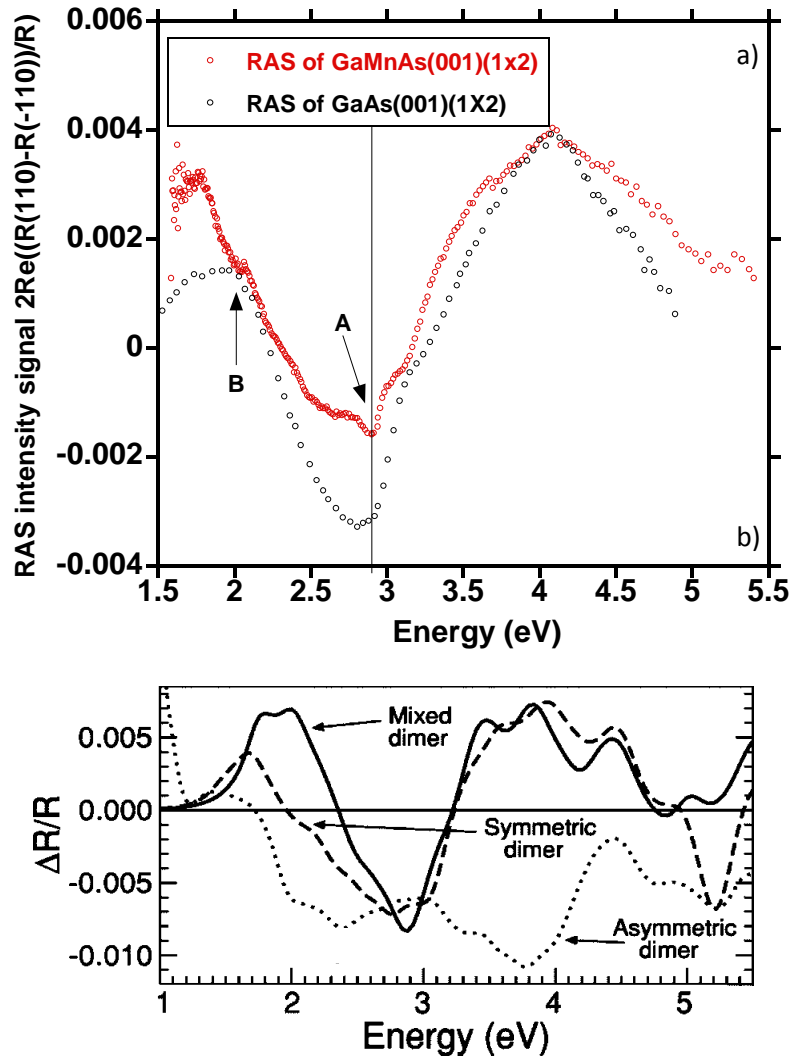


Fig. 6.5. (a) **RAS** spectrum of *GaMnAs* (in red) compared with that of *GaAs* (in black) [11]. The arrows mark the differences between the spectra. The vertical line represent the limit between bulk and surface areas. In (b) Theoretical *ab initio* *GaAs*(001) **RAS** spectra [14].

The similarity between the two spectra in Fig. 6.5 (a) suggests the presence of dimers on the *GaMnAs*(001) surface. Nevertheless there are several differences between the two spectra, e.g. the structure at 2.9eV (indicated by “A” in Fig. 6.5) which most likely is due to the interference of reflected beams from the interfaces *vacuum* – *GaAs* and *GaAs* – *GaMnAs*. Another difference is shown at $\sim 2\text{eV}$ (structure B) in which the **RAS** signal of *GaMnAs* is more intense and structured than that of *GaAs*. As said above, the comparison indicates the possible presence of dimers in the *GaMnAs*(001) surface. In order to confirm this hypothesis, the *GaMnAs* **RAS** spectrum is compared to a theoretical first-principle

calculation of the $GaAs(001)c(4 \times 4)$ surface [14] (Fig. 6.5(b)). Although the comparison is made between surfaces with different reconstructions, it is possible to extract information about the nature of the dimers. In particular, the simulation is done for asymmetric dimers ($As - As$ dimers with different bond length), mixed dimers ($As - Ga$) and symmetric dimers ($As - As$). The asymmetric dimer model is incompatible with our experimental result while the symmetric dimer one reproduces well the features around $2 eV$, the width of the negative peak at $2.9 eV$ and the broad structure centered at $4 eV$. So we conclude that the dimers present on the $GaMnAs(001)$ surface are probably symmetric $As - As$ dimers.

To better understand, although qualitatively, the features of the $GaMnAs$ spectra, we proceed to further comparative analyses. As the substrate on which the $GaMnAs$ film is grown is $GaAs(001)c(4 \times 4)$, it is plausible that some of $GaMnAs$ structures are similar to those of the substrate. To this purpose the **RAS** spectrum of $GaMnAs$ is compared to that measured on the $GaAs(001)c(4 \times 4)$ surface, concentrating on the low energy ($< 3eV$) region where surface contributions are located (Fig.6.6).

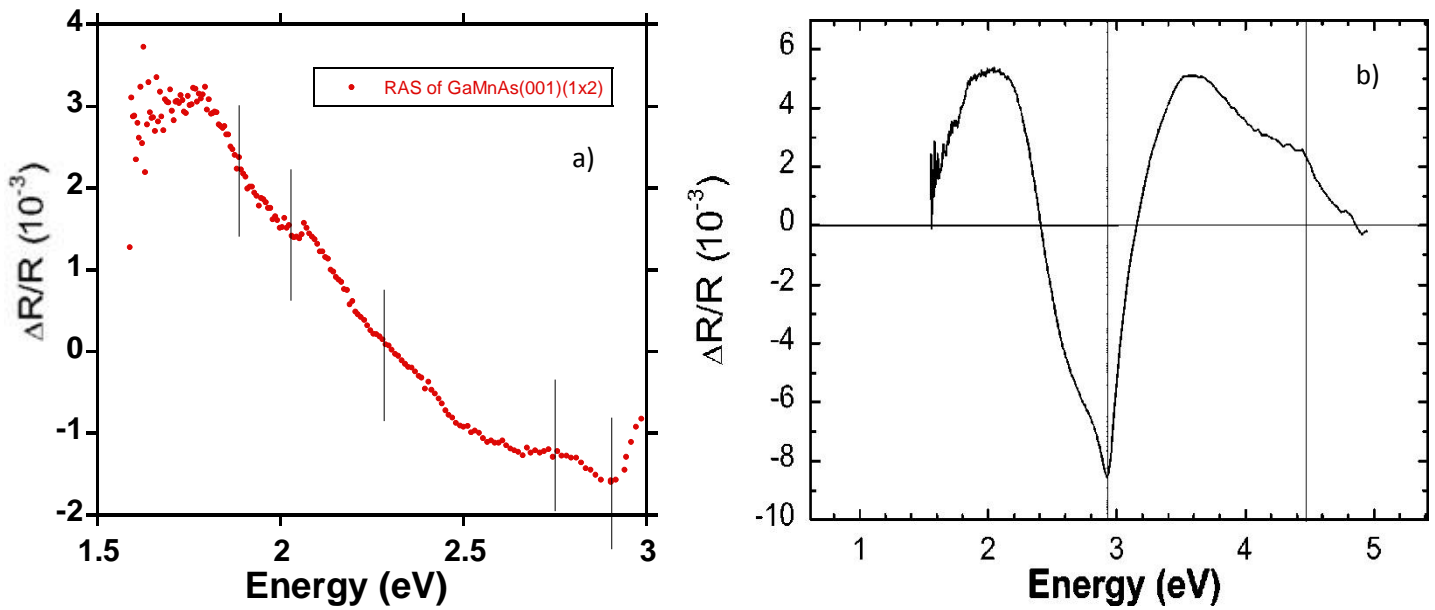


Fig. 6.6. (a) Zoom of the **RAS** spectrum of Fig. 6.4 of *GaMnAs*(001)(1 × 2) and (b) *GaAs*(001)*c*(4 × 4) spectrum taken from reference [12].

In the case of *GaAs* the spectrum consists of two peaks located approximately at 1.8 eV and 2.25 eV and forming a broad structure centered around 2 eV and a strong negative peak at 2.9 eV with a shoulder at 2.7 eV. In the case of *GaMnAs* there is a structure located around 2 eV and, at a higher energy, a shoulder at 2.75 eV and a negative peak at 2.9 eV. The main difference is the shape of the structure at approximately 2 eV, which seems to contain more contributions than in the *GaAs* spectrum. In comparison with *GaAs* [13], a contribution at 1.8 eV, assuming the presence of As – As dimers on the surface, can be attributed to transitions from the electronic states of the As atoms of the second layer along the high symmetry direction $\Gamma - J$ of the surface Brillouin zone to the As dimer states, while the peak at 2.25 eV can be attributed to transitions at localized sites along the direction $\Gamma - J'$. The latter have mixed nature – surface and bulk – since they include both the transitions between surface states and surface valence states and bulk conduction states [13, 14] (in the case of *GaAs* the transitions are due to the asymmetrical dimers of As – Ga). The peak at 2.9 eV coincides with the critical point (*L*) in the density of states and is explained in terms of transition between bulk states modified by the surface in agreement with the **EELS** measurements discussed below.

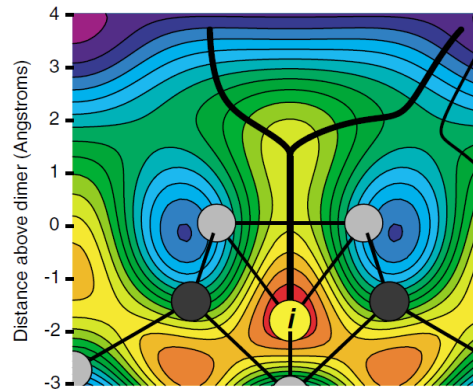


Fig. 6.7. Potential-energy surface for Mn adsorption on $GaAs(001)$, plotted in a plane normal to the surface and containing the As surface dimer (white spheres). The minimum energy adsorption site is the subsurface interstitial site labeled i . The gray spheres represent Ga atoms [1].

In the $GaMnAs$ spectrum, besides the peaks at 1.8 eV and 2.25 eV , another surface contribution is present which originates from the interaction between the d state of Mn and p states of As . In Fig. 6.7 a possible adsorption site for Mn below a symmetric As dimer is presented [1]. The strong anisotropy observed at low energy could originate from As dimers oriented along the $[110]$ direction, the same direction of the mixed $As - Ga$ dimers on $GaAs$ (the existence of such dimers will be checked by *in-situ STM* measurements presented later). $p - d$ hybridisation in subsurface layers may be the source of additional low-energy anisotropy, as suggested by resonant photoemission spectra performed on $GaMnAs$ [9], where a peak at about 2 eV was attributed to a strong hybridisation between $Mn\ 3d$ states and $GaAs$ valence bands around the van Hove singularity at the L point of the Brillouin zone (L_3 state). Magnetic circular dichroism (**MCD**) measurements on $GaMnAs$ in the visible and ultraviolet ranges[16] confirm this hypothesis. These results suggest antiferromagnetic coupling between the $3d$ states of Mn and the $2p$ binding states of As on a strongly hybridised and anisotropic surface state. Fig. 6.8 shows schematically the formation of bonding (opposite Mn and As spins) and anti-bonding states (parallel Mn and As spins) before and after hybridisation for an isolated impurity and a system of several Mn atoms forming an impurity band.

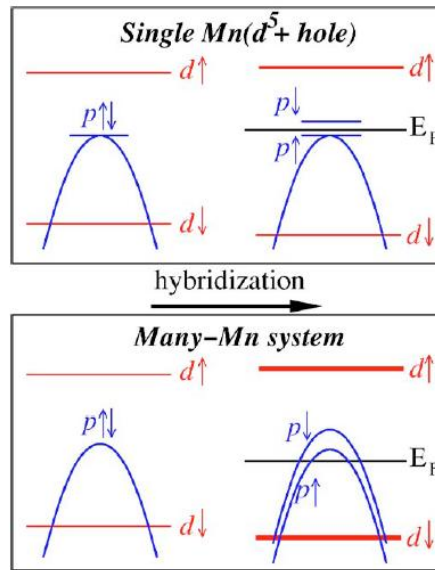


Fig. 6.8. Schematic electron diagram before and after hybridisation: splitting of the acceptor level of a single atom of Mn (upper) and of a system of many atoms of Mn (lower) due to $p - d$ hybridisation [17].

In order to deepen insight into the electronic structure of the $GaMnAs$ surface, electron energy loss spectroscopy (**EELS**) in conjunction with reflectance anisotropy spectroscopy (**RAS**) [8] was used. As proved on $GaAs(001)c(4 \times 4)$ and $GaAs(001)\beta 2(2 \times 4)$ surfaces [13, 18, 19]. **EELS** permits the study surface states and surface atomic bonding with a sensitivity approximately two order of magnitude higher than optical techniques. Specular reflectance energy loss spectra were acquired at room temperature with a total scattering angle of 90° . The angle of incidence of the primary electronic beam (15 eV) was 45° with respect to the sample normal and the acceptance angle was approximately 2° . In these conditions $q \sim 0.25 \text{ \AA}^{-1}$ at a loss energy of 5 eV ; the energy resolution, measured at full width at half maximum (FWHM) of the elastic peak, was approximately 30 meV (Fig. 6.9).

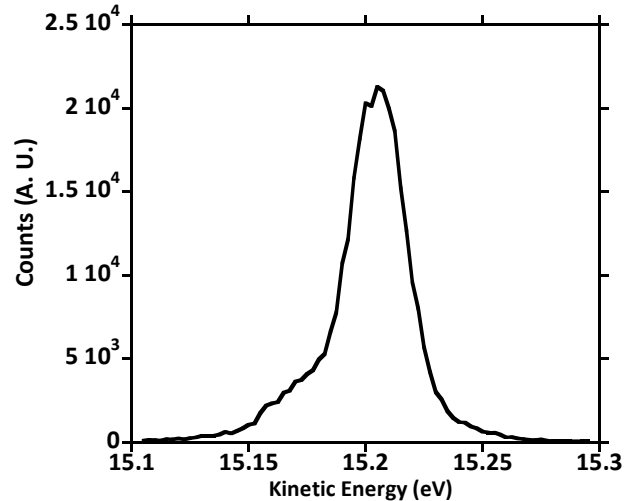


Fig. 6.9. Elastic peak measured with a primary electron beam energy of 15eV.

In order to compare the results of two different surfaces (along the $[110]$ and $[\bar{1}10]$ directions), loss spectra were measured on a buffer layer of $GaAs(001)c(4 \times 4)$ (the growth conditions were discussed in section 5.1) and on a $GaMnAs(001) (1 \times 2)$ layer doped with approximately 1% of Mn . The results for the $GaMnAs$ surface are shown in Fig. 6.10 and 6.11. The intense peak centred at approximately 4 eV is typical of $GaAs$ transitions. The energy loss spectrum along the $[\bar{1}10]$ direction is very similar to that along the $[110]$ direction. Actually, in both spectra there are structures at approximately 2 eV, 2.25 eV, and 2.7 eV, those in the $[110]$ direction being more intense. In the $[-110]$ direction some features are less intense, except the one at 2.7 eV. For sake of comparison the **RAS** structures found on $GaMnAs$ in the 1 – 3 eV loss energy range are shown in the inset of Fig. 6.10. Although the anisotropy observed with **RAS** does not show up in the **EELS** spectrum, the intensity difference between the two directions comes probably from the different electronic density associated with As dimers aligned along the $[110]$ direction. Besides, the minimum at 2.9 eV, clearly visible in the **RAS** spectra, it is not present in any of the two directions of the **EELS** spectrum. In this regard, the fact that this peak is due to electron transitions between bulk-like states and that electrons penetrate less than photons confirm that the 2.9 eV transition actually involves bulk states. Moreover, as shown in Chapter 4, the **EELS** cross section depends on the kinematic factor which is inversely proportional to energy; as such, the energy loss intensity at 2 eV is approximately 5 times larger than that at 2.9 eV.

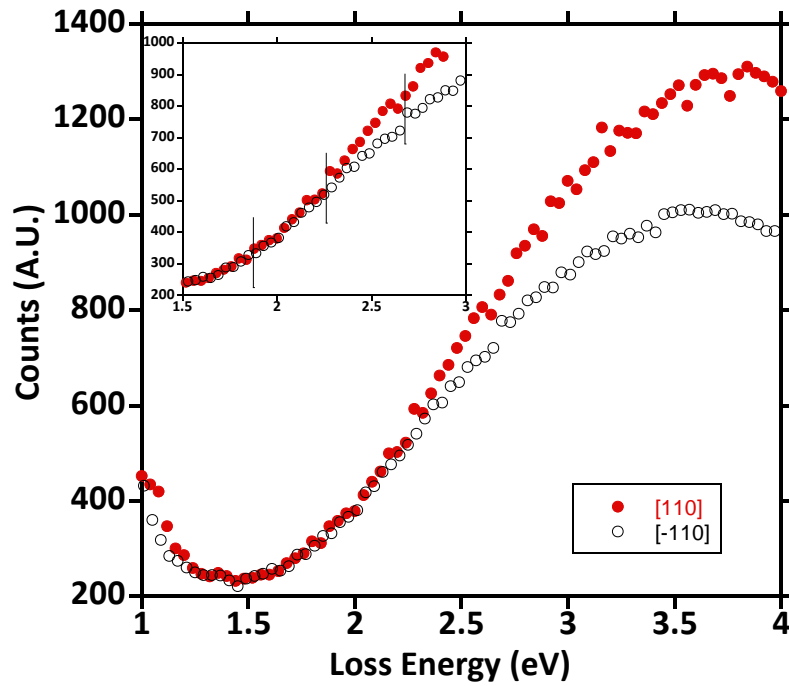


Fig. 6.10. *EELS* of *GaMnAs* in the [110] and $[\bar{1}10]$ directions with 10 eV primary energy. In the inset the presence of three weak peaks (at 1.9 eV, 2.25 eV and 2.7 eV) can be noted. The vertical lines mark the peaks observed in the *RAS* measurements.

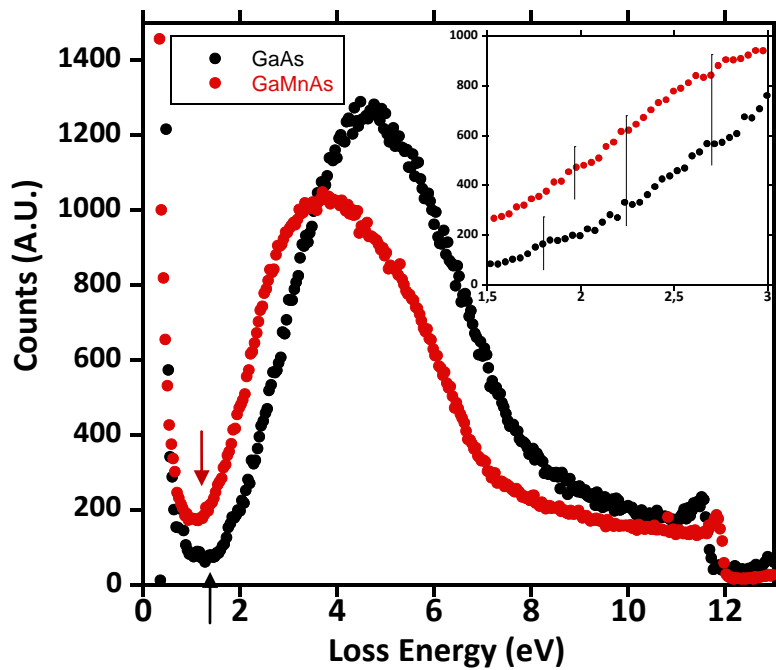


Fig. 6.11. *EELS* of *GaAs* and *GaMnAs* spectra along the [110] direction. The primary energy is 15 eV. The arrows mark the gap reduction in *GaMnAs*. In the inset the presence of three peaks at 1.8 eV, 2.25 eV and 2.7 eV can be noted. In *GaMnAs*, the peak at 1.8 eV is lacking and a new peak appears at 1.9 eV.

Further analysis can be performed to compare the **EELS** spectrum of *GaMnAs*(001) in the [110] direction to that of *GaAs*(001)*c*(4 × 4) obtained before *Mn* deposition (Fig. 6.10). The gap of *GaMnAs* is smaller than that of *GaAs*, as indicated by the arrows in Fig. 6.11. This is a well known fact [20] (the gap of the *GaAs* is approximately 1.45 eV and that of *GaMnAs* is approximately 1.25 eV) that testifies the high quality of our *GaMnAs* film. Moreover, the peaks observed at 2.25 eV and 2.7 eV, shown by full lines, coincide with those of *GaAs*, as evident in the inset of Fig. 6.11, while the *GaAs* peak at 1.8 eV, attributed to transitions between surface band states [12, 13], disappears in *GaMnAs* where instead a feature is observed near 2 eV. This phenomenon, observed previously in **RAS** spectra and explained in photoemission and **MCD** measurements [9, 16], confirms the presence of *p* – *d* hybridisation between *d* states of *Mn* and *p* states of *As*.

The above results are a first characterization of the *GaMnAs*(001) surface obtained with the **RAS** and **EELS** techniques, and give clear evidence that the surface is characterized by the presence of *As* – *As* dimers. The exact structure of this surface is unknown even if it is plausible to assume, as suggested by our **EELS** measurements, that a distribution of *As* dimers with an *As* – *As* bond parallel to the [110] direction exists [11]. Our measurements confirm that *p* – *d* hybridisation is due to an impurity band present on the surface, even at low *Mn* concentrations. This might support the hypothesis that ferromagnetism on diluted magnetic semi-conductors is due to the interaction between delocalized holes in the valence band and the holes in the impurity band.

In order to confirm the presence on the surface of *As* – *As* dimers and measure the composition of these dimers, **STM** images of the *MBE*-grown *GaMnAs* surface, were obtained. To this purpose, the mobile chamber was used for the **STM** measurements. Constant current **STM** images of the *GaMnAs*(001) surface are shown in Fig. 6.12 (50 × 50 nm) and Fig. 6.13 (20 × 20 nm). The images display a highly disordered surface on which, in contrast to cross sectional measurements [20], identification of *Mn* atoms is difficult, as also evident from the asymmetry of the **RHEED** lines (Fig.5.6). As a result of *Mn* reactivity, the *GaMnAs* surface appears disordered. The nature of the (1 × 2) reconstruction, observed immediately after the growth without exposing the surface to the ambient, is not yet clear and no previous papers in literature report on the *in situ* topography of such surface.

Nevertheless, the characteristic bricks of the $GaAs(001)c(4 \times 4)$ reconstructed surface, oriented along the $[110]$ direction, are still present, even in disordered fashion, similar to those found on the $GaAs$ surface after deposition of 1.75 ML of As [11]. The authors of Ref. [11] attribute these bricks to a random distribution of As dimers. As previously mentioned, the existence of such dimers supports the picture of a possible adsorption site of Mn below the dimer site [1]; therefore, the position of Mn makes its identification difficult. It is also possible that the strong surface disorder is caused by a post-growth annealing (see Chapter 5) not sufficient to remove all As impurities.

In conclusion, all the above techniques have contributed to clarifying the (1×2) surface reconstruction of $GaMnAs$ as well as the interaction between Mn and $GaAs$. The later aspect is relevant also in view of potential applications of $GaMnAs$. For this reason, additional research was pursued by depositing Mn on $GaAs$ surface under conditions similar to those of the **MBE** growth and analysing the $Mn-As$ bonds formed in the first stage of growth.

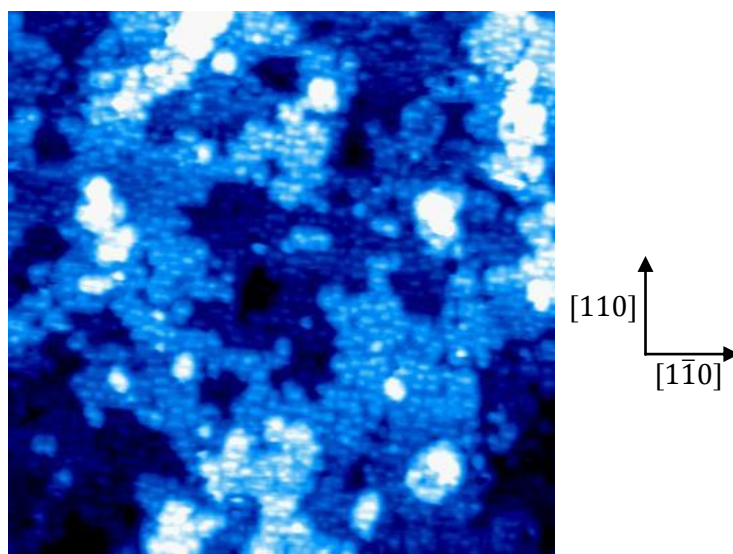


Fig. 6.12. **STM** image of the *GaMnAs*(001) sample. The size is $50 \times 50 \text{ nm}$ at $V = -2V$ and $I = 1 \text{ nA}$.

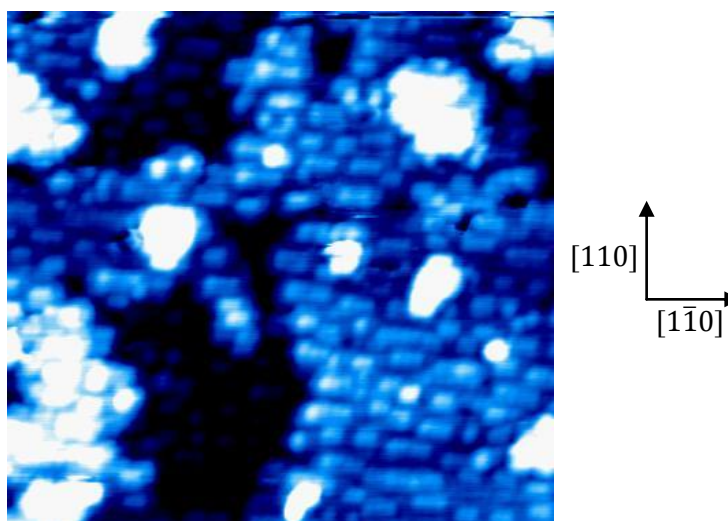


Fig. 6.13. **STM** image of the *GaMnAs*(001) sample. The size is $20 \times 20 \text{ nm}$ at $V = -2V$ and $I = 1 \text{ nA}$.

6.3. Experimental results on the *Mn/GaAs(001)* surface

From the results of the previous section it clearly appears the interest in the investigation of the *Mn* interaction with the *GaAs(001)* surface, which calls for a study of the *Mn/GaAs(001)* interface. To this end **XPS**, **XAS**, **PED** and **STM** measurements were performed.

The synchrotron radiation **XPS**, **XAS** and **PED** measurements were carried out at the Aloisa beamline at the ELETTRA synchrotron facility (Trieste, Italy) [22]. The *As* –cap (see section 5.2) was removed in the analysis chamber by fast annealing at about 350 °C under **RHEED** monitoring. After removal of the cap layer a sharp $c(4 \times 4)$ **RHEED** pattern appeared demonstrating that the underlying high-quality surface was preserved (Fig. 6.10a). The sample temperature was measured by a thermocouple mounted directly on the sample holder. Photoemission spectroscopy measurements were performed using an *X* – ray beam ($h\nu = 765$ eV) at grazing incidence (about 3° off the surface) and collecting the electrons along the surface normal by a hemispherical analyzer. After deposition of 1ML (1ML = 0.8 Å relative to the *GaAs(001)* bulk-terminated surface) of *Mn* the **RHEED** pattern is characterized by a (1×1) periodicity with a weak (1×2) reconstruction over imposed (Fig. 6.10b). After annealing at 250 °C, the **RHEED** pattern converts to the (1×2) symmetry of a less disordered surface (Fig. 6.10c). The very interesting result is that this reconstruction is the same as that of the *GaMnAs* growth at 250 °C.

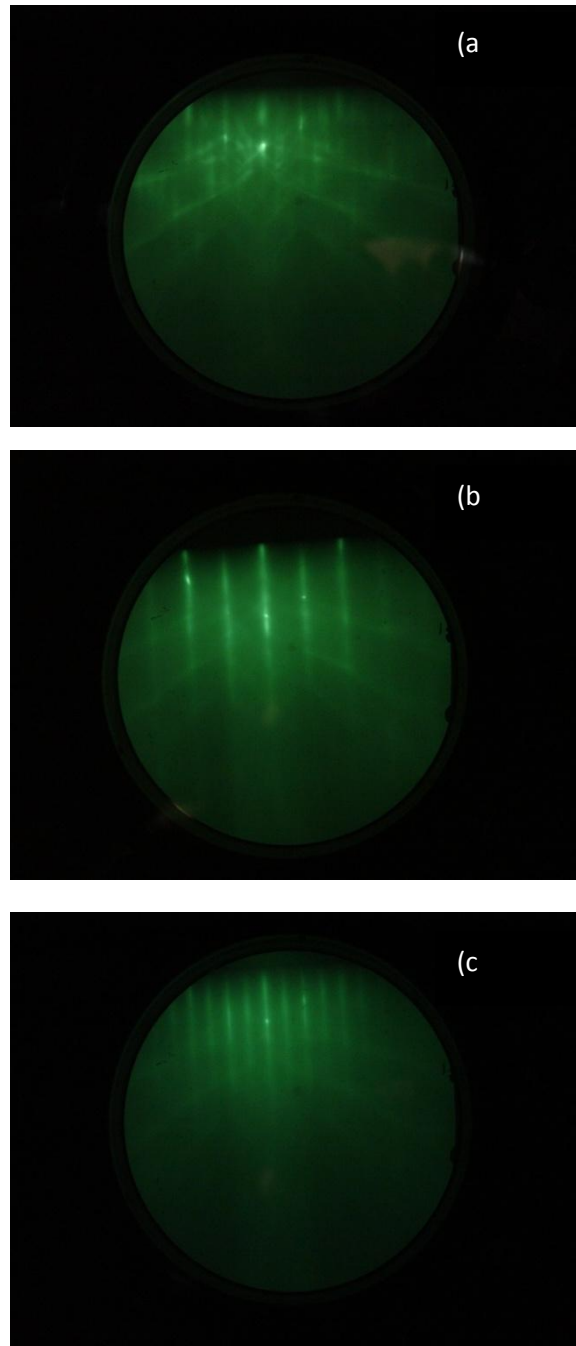


Fig. 6.10. **RHEED** patterns of *GaAs* just after decapping procedure (a), after *Mn* deposition (b) and after LT annealing.

For each step (*GaAs* clean, *Mn* deposition and subsequently low temperature annealing) we performed **XPS** analysis of *As 3d* core level, *Ga 3d* core level and, when present, *Mn 2p* core level. Before each run, a complete spectrum with *C*, *In*, *Mo* and *O* core levels has been collected to verify the complete absence of contamination. Fig. 6.11a shows the *As – 3d* core level **XPS** spectra of *GaAs* as decapped. After deposition of 1 *ML* of *Mn* a rigid shift

(0.7 eV) of the whole spectrum towards higher binding energies is observed (Fig. 6.11b) which can be attributed to surface band bending (Fermi level pinning) [23]. After annealing, a relaxation of the Schottky barrier energy of about 0.3 eV takes place (Fig. 6.11c), suggesting that a modification of the surface occurred, in agreement with the **STM** data. Extensive work made on *GaAs*(110) and *GaAs*(001) surfaces [24, 25] covered with submonolayer-thick metal overlayers have shown that transition metals tend to pin the Fermi level and to disrupt the interface structure within about 3 *MLs* from the surface at a few *MLs* coverages. Increasing temperature, E_F move towards midgap. This implies interaction between the metal atoms and the substrate in the subsurface region. A similar behavior is found here in the case of *Mn*. A more detailed analysis of the underlying spectral components was performed by a fitting procedure using *Doniach-Sunijch* line shapes and setting the *3d* spin-orbit splitting and the branching ratio to 0.68 eV and 0.61 eV, respectively. The relevant fit results are listed in Table 1. The spectra consist of three distinct peaks with different intensities; the largest one is the bulk component (*B*) and the two lateral peaks are surface components; S_1 (at lower binding energy) is due to the *As – As* bonds and S_2 (at higher binding energy) is due to the *Ga – As* bonds (Fig. 6.11a) [26, 27]. After *Mn* deposition (Fig. 6.11b) and annealing (Fig. 6.11c), S_2 decreases in intensity, while the S_1 component increases (see Tab. 1). The decrease of S_2 could be an indication of the high reactivity of *Mn* with *GaAs* which destroys the surface structure. On the other hand, the S_1 increase could be explained by the formation of *Mn – As* bonds evidenced by a possible new spectral component (hereafter referred to as *M*) occurring at the same binding energy of S_1 [26, 27].

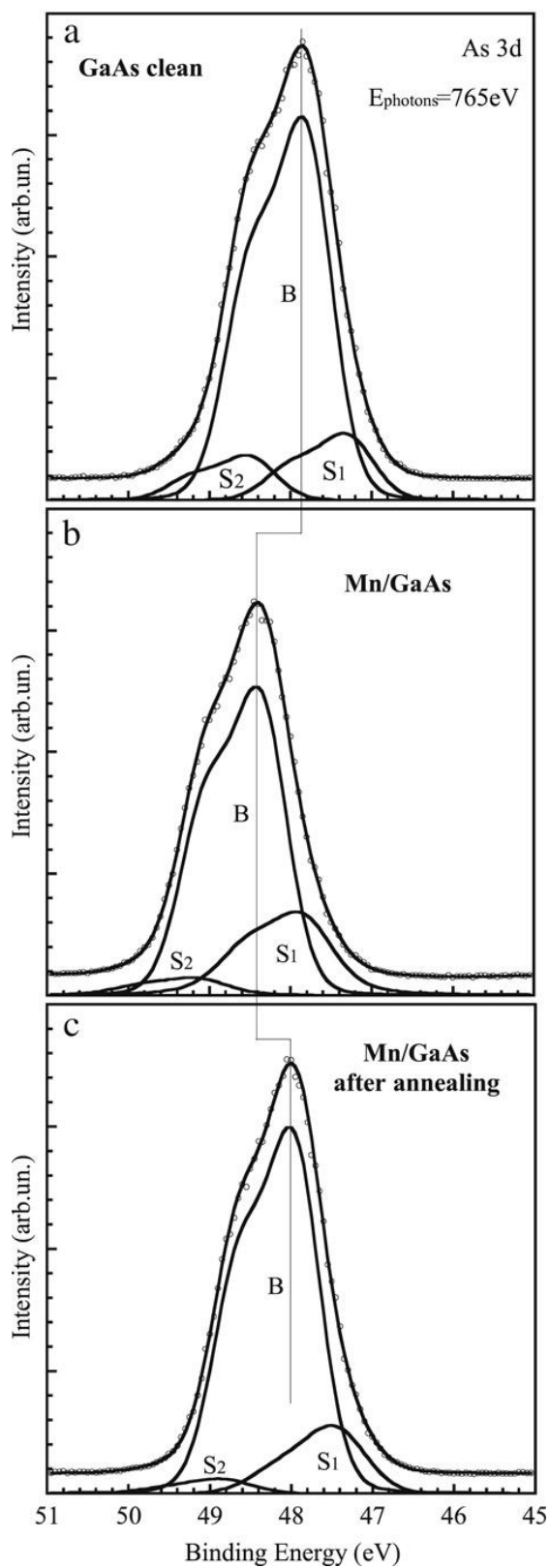


Fig. 6.11. As 3d core level spectra: (a) clean surface, (b) after 1 ML Mn deposition, and (c) after annealing at 250 °C. The primary photon energy is 765 eV, the energy is referred to the vacuum level.

In Fig. 6.12 the $Mn\ 2p$ core level spectra before and after annealing are shown. At first glance we note in the annealed spectrum the disappearance of a shoulder located at the peak onset as a result of the Mn reaction induced by the annealing. The $Mn\ 2p$ components were analyzed by a fitting procedure similar to that of the $As\ 3d$ edge and the results are summarized in Tab. 2. We found that the $Mn\ 2p$ core level can be decomposed in four contributions (referred to as $P_1 - P_4$) that are very similar to the deconvolution of $Mn\ 2p$ spectra on $MnTe$ [28]. So we can reasonably attribute the P_1 peak to Mn in the metallic state and/or in a $MnAs_x$ compound [26, 28] and the P_2 peak to Mn in $MnAs$ or $GaMnAs$ [26]. Accordingly, P_3 and P_4 are satellite peaks of P_1 and P_2 , respectively. After annealing, a strong decrease of the P_1 intensity is observed which is responsible for the change of the lineshape of the core level peak. The reduction of P_1 is interpreted as a reduction of the $MnAs_x$ component at the surface, in agreement with the reduction of the M component in the $As\ 3d$ peak after the thermal treatment. Hence, the **XPS** data point to a reduction of the Mn in the metallic state or in the $MnAs_x$ state after the annealing. It is probable that the $Mn - As$ bond of this sub-stoichiometric compound is broken by temperature thus allowing Mn atoms to diffuse into the $GaAs$ substrate.

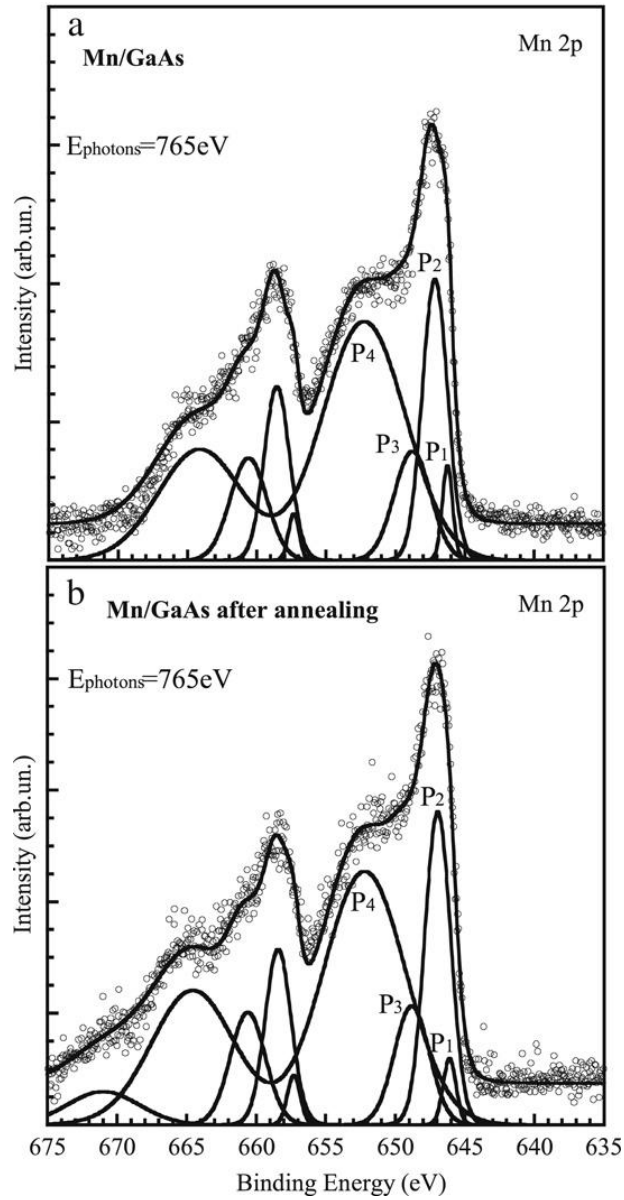


Fig. 6.12. *Mn 2p* core level spectra of: (a) 1ML *Mn* on *GaAs(001)c(4 × 4)*, and (b) after annealing. The primary photon energy is 765 eV, the energy is referred to the vacuum level.

As 3d	GaAs clean	GaAs + Mn	GaAs + Mn + annealing
Area S_1	204	327	207
Area S_2	136	69	43
$\Delta E(B - S_1)$	-0.52	-0.52	-0.52
$\Delta E(B - S_2)$	+0.74	+0.77	+0.78
Mn 2p			
Area P_1	-	28	12
Area P_2	-	201	115
Area P_3	-	157	72
Area P_4	-	633	349
$\Delta E(P_2 - P_1)$	-	0.9	0.9
$\Delta E(P_3 - P_1)$	-	2.5	2.7
$\Delta E(P_4 - P_1)$	-	6.0	6.1

Tab. 1. Results of the fitting procedure of the *As 3d* and *Mn 2p* core level peaks. Energies are in eV.

To investigate the nature of the $Mn - As$ bonding, the $Mn L_{II,III}$ absorption edge before and after the thermal treatment were measured [22] and the corresponding spectra are shown in Fig. 6.13. The $Mn L_{II}$ edge depends strongly on Mn coordination while final-state effects split the edge in a multiplet structure [29]. It is known that $Mn L_{II}$ edge is a doublet when measured in $GaMnAs$ alloys, while it is a single structure in $MnAs$ [31]. A similar behavior has been also observed in the $Mn - Ge$ diluted alloy obtained by ion implantation; the L_{II} edge appears as a broad structure in the as implanted sample and splits in a doublet when the sample is annealed due the Mn atoms diffusion in the substitution position of the alloy [31]. Since we observe a splitting of the L_{II} edge immediately after Mn deposition, it is plausible that an alloy involving both Ga and As has already been formed before annealing. Since **STM** data are compatible with the presence of $MnAs$ clusters, we cannot exclude that the spectra of Fig. 6.13 contain both contributions, i.e. the L_{II} peak of $GaMnAs$ and the L_{II} peak of $MnAs$ [29]. On the other hand, we observe a reduction of the high energy tail of the L_{III} edge after the thermal treatment which can be interpreted similarly to the $Mn - Ge$ system, as the diffusion of Mn atoms in the $GaAs$ matrix in substitutional position [30, 32]. Because, the L_{III} edge exhibits a narrower shape after the annealing which is interpreted as a diffusion of the Mn atoms in the $GaAs$ matrix we can argue that probably the $Mn - As$ bonds of sub-stoichiometric surface compounds are broken by temperature thus allowing Mn atoms to diffuse into the $GaAs$ substrate. In such a way the surface electronic state can be changed affecting also the band bending, giving a reasonable explanation of the observed energy shift of the $As 3d$ core level peak after the thermal treatment. On the other hand it is not possible to exclude that the defects induced by the Mn reaction with the surface could be responsible for the observed band bending in this case the thermal treatment, inducing a reduction of the surface defects, could reduce the band bending at the surface. The presence of more peaks under the $Mn 2p$ spectra and the result from absorption spectra that shows the presence of $GaMnAs$ immediately after growth, suggested us to investigate the surface morphology with **STM** and **PED**.

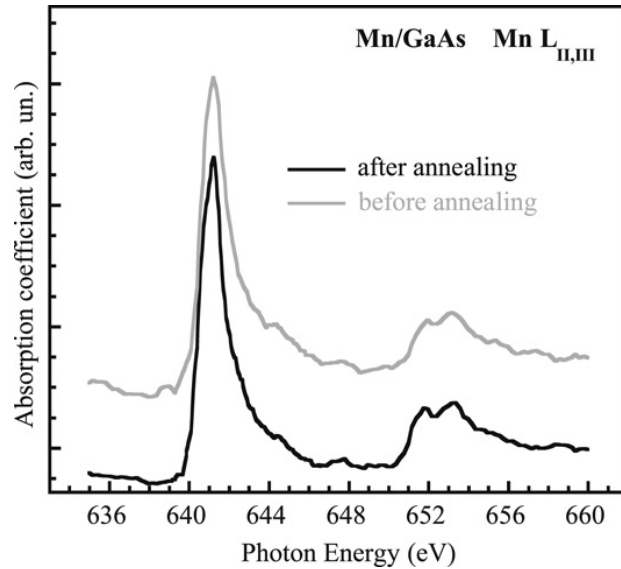


Fig. 6.13. $Mn L_{II,III}$ absorption edge of 1 ML of Mn on $GaAs(001)c(4 \times 4)$ before (dashed line), and after annealing at 250 °C (solid line).

In Fig. 6.14 filled electronic states constant current **STM** images (gap bias $-3 V$, tunneling current $0.1 nA$) are shown together with the **LEED** pattern collected on the same surfaces [22]. The clean surface (Fig. 6.14 (a)) shows a clear $c(4 \times 4)$ **LEED** patterns and the **STM** topography exhibits the typical three *As* – *Ga* hybrid dimer blocks characteristic of the $GaAs(001)c(4 \times 4)$ reconstruction [33]. After 1 ML ($1 ML = 0.8 \text{ \AA}$ relative to the $GaAs(001)$ bulk-terminated surface) *Mn* deposition, the **LEED** pattern is characterized by a (1×1) periodicity with a weak (1×2) reconstruction over imposed (Fig. 6.14 (b)). The related **STM** morphology is similar to that of *MnAs* clusters distributed randomly over the surface [34]. It is worthwhile to note that the $0.3 nm$ height of these aggregates is fully compatible with a submonolayer formation of *MnAs* aggregates [34]. This is a first evidence of the *Mn* high reactivity with *GaAs*. After annealing at 250 °C, the **LEED** pattern (Fig. 6.14(c)) converts to the (1×2) symmetry of a less disordered surface. Accordingly, the **STM** image shows larger structures partially ordered along the $[\bar{1}10]$ direction. A closer view $-(20 \times 20) nm^2$ - of the surface, is reported in Fig. 6.14(d), where a periodic corrugation of the surface is observable below the aggregates, indicating a possible sign of reconstruction after the thermal process. We argue that after annealing the surface tends to rearrange itself to form a *Mn*-induced (1×2) reconstruction and clusters of intermixed species (probably *MnAs*).

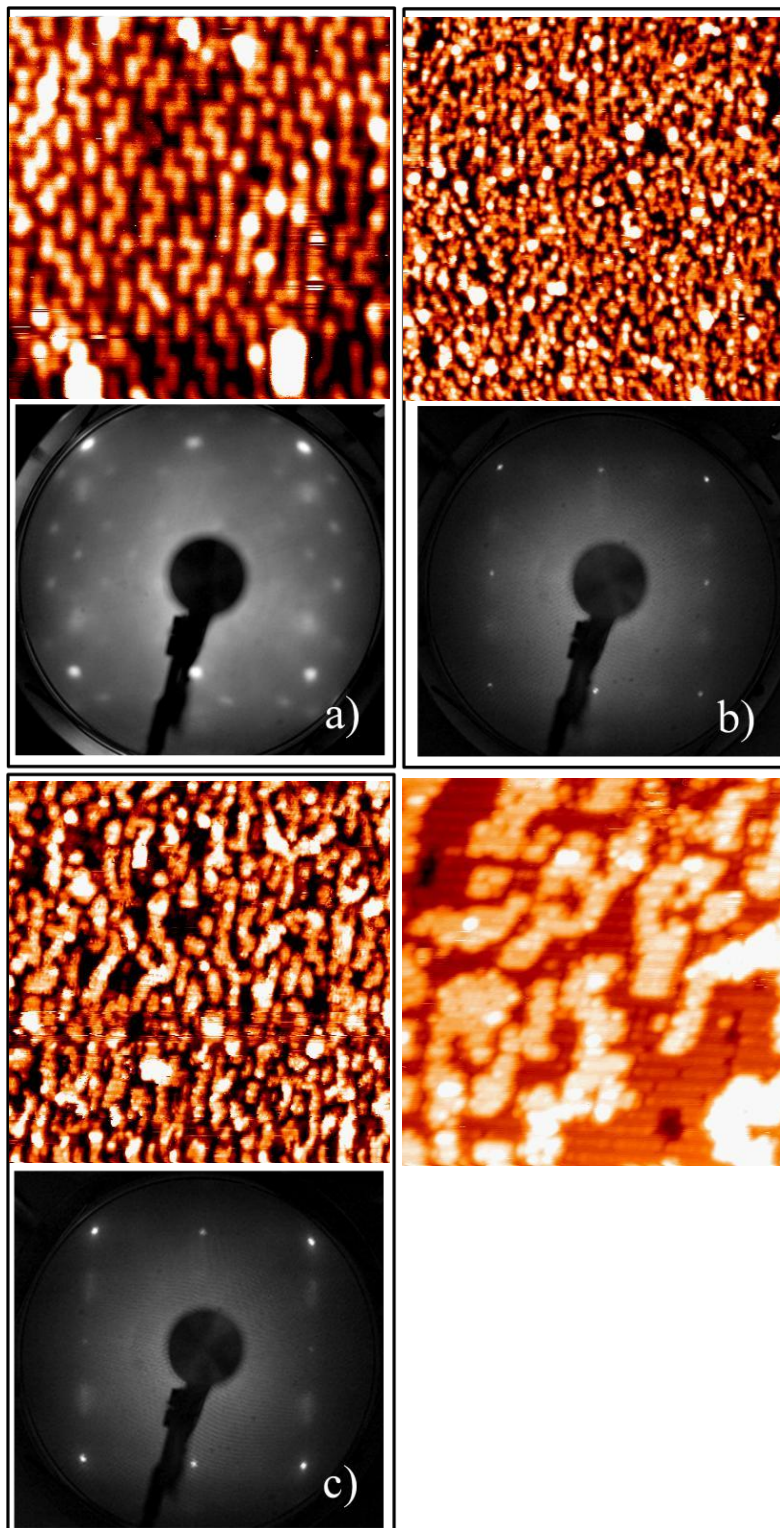


Fig. 6.14 **STM** images of the $GaAs(001)c(4 \times 4)$ surface with the related **LEED** patterns taken with beam energy $E_p = 37 \text{ eV}$: a) $(15 \times 15) \text{ nm}^2$ clean surface, b) $(50 \times 50) \text{ nm}^2$ surface covered with 1ML of Mn, and c) $(50 \times 50) \text{ nm}^2$ surface after annealing at $250 \text{ }^\circ\text{C}$. d) zoom $(20 \times 20) \text{ nm}^2$ of image c). The images were measured with -3 V bias voltage and 0.1 nA tunneling current.

PED measurements were performed on a sample annealed after *Mn* deposition; this measure could give important information concerning *Mn* bonding on the surface. As we said in Section 4.6.1, **PED** is a powerful technique able to investigate the surface coordination of the emitting atoms and, indirectly, to identify the adsorption site of a specific atom (*Mn* in our case) on the (*GaAs*) surface. The experimental setup is shown in Fig. 6.15.

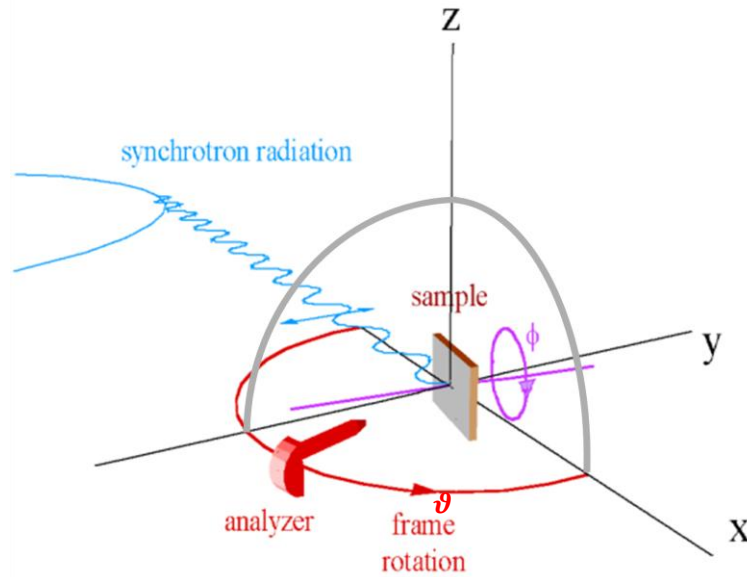


Fig. 6.15. Experimental setup for **PED** acquisition. Varying the angles ϑ and ϕ it is possible to acquire **XPD** spectra for a quarter of sphere. It is necessary to acquire only a eighth of the sphere because we have specular symmetry in the case of *GaAs*(001)*c*(4 × 4).

The experiment consisted in the acquisition of a photoemission spectrum varying the angle of the analyzer (ϑ) and the angle of the sample (ϕ) while maintaining the angle of the sample with respect to the beam small (about 3°) to maximize the signal coming from the surface (see Fig. 6.15). When the analyzer was positioned normal to the surface, the angle ϑ was at 90°; in the case of our sample the surface [100] direction was obtained when $\phi = 18^\circ$.

Actually to obtain information about our system, that has a square symmetry (*GaAs*(001)*c*(4 × 4)), it is sufficient to collect data from a eighth of sphere shown by the gray curves in Fig. 6.15. The photoemission spectra acquired from each point (850 in our

case) had a shape like the spectrum shown in Fig. 6.16 in the particular case of $\vartheta = 41.5^\circ$ and $\phi = 7^\circ$. The photon energy was 765eV .

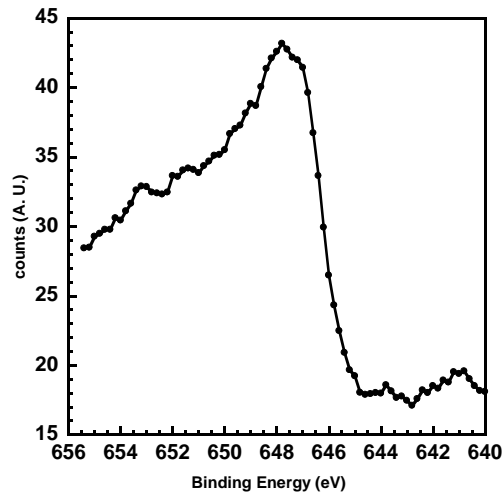


Fig. 6.16. Photoemission spectra acquired with $\vartheta = 41.5^\circ$ and $\phi = 7^\circ$.

To each photoemission spectrum was applied the same fit procedure that we used for the *XPS* analysis (6.17); as already said, the P_1 peak was associated to *Mn* in the metallic state and/or in a $MnAs_x$ compound, the P_2 peak to *Mn* in $MnAs$ or $GaMnAs$; the P_3 and P_4 are satellite peaks of P_1 and P_2 , respectively. Only one component of the spin orbit doublet was acquired thus we used a *Lorentian/Voigt* line shapes to fit the experimental data.

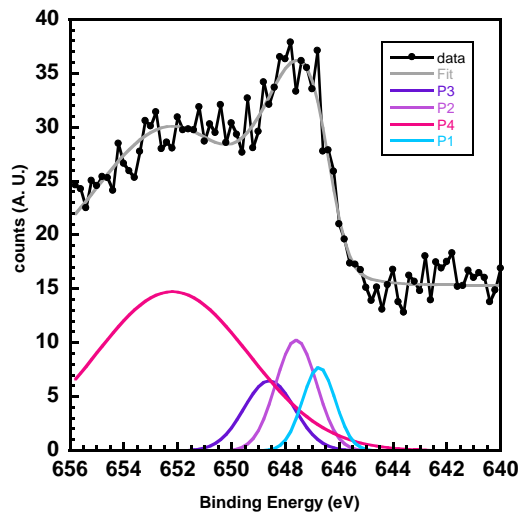


Fig. 6.17. Example of fit with *Lorentian/Voigt* line shapes of a photoemission spectrum acquired with $\vartheta = 39^\circ$ and $\phi = 7^\circ$.

Ideally, the energy position and the shape of the photoemission spectra (FWHM parameter) could remain the same for each (ϕ, ϑ) point; the only variable parameter being the area of the peaks versus ϕ, ϑ . This area describes the intensity I that changes as a function of polar angles. In the actual case several hours were necessary to acquire all the data; in this long time measurement it was possible to encounter energy instability of the beam and this aspect should be taken carefully in account during data analysis.

The anisotropy is described by $\chi = (I - I_0)/I_0$ where I_0 is a non diffractive intensity (see section 4.6.1). The I_0 term was obtained by fitting a polynomial curve to the acquired data. After the fit procedure of all the acquired (ϕ, ϑ) points for the P_1 peak and P_2 peak, we obtained the peaks area (I) versus the polar angles (ϑ) for each value of ϕ . In Fig. 6.18 a typical *area-angle* data is presented; the actual data are in the range of about $10^\circ - 90^\circ$ with $\phi = 37^\circ$; then a specular curve is constructed ($90^\circ - 170^\circ$) to permit a polynomial curve to fit the data (a *9 order* polynomial curve has been used). This procedure has been followed for each (ϕ, ϑ) point; then the specular data ($90^\circ - 170^\circ$) are removed and the anisotropy χ is obtained for the P_1 and P_2 peaks as a function of the k polar coordinates projection of the outgoing electron ($k_x = \cos\phi\sin\vartheta, k_y = \sin\phi\sin\vartheta$) (Fig.6.19).

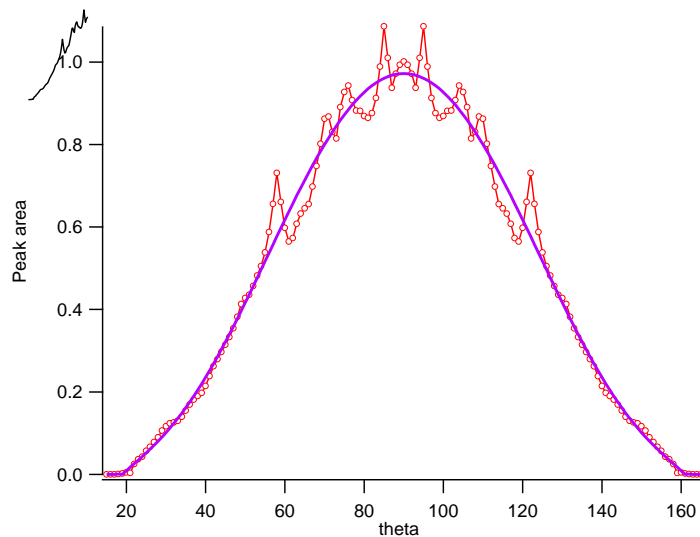


Fig. 6.18. Example of a *9 order* polynomial curve fit with the *area peak-angle* data. The actual data is in the range of about $10^\circ - 90^\circ$; then a specular curve is constructed ($90^\circ - 170^\circ$) to permit a polynomial curve to fit the data.

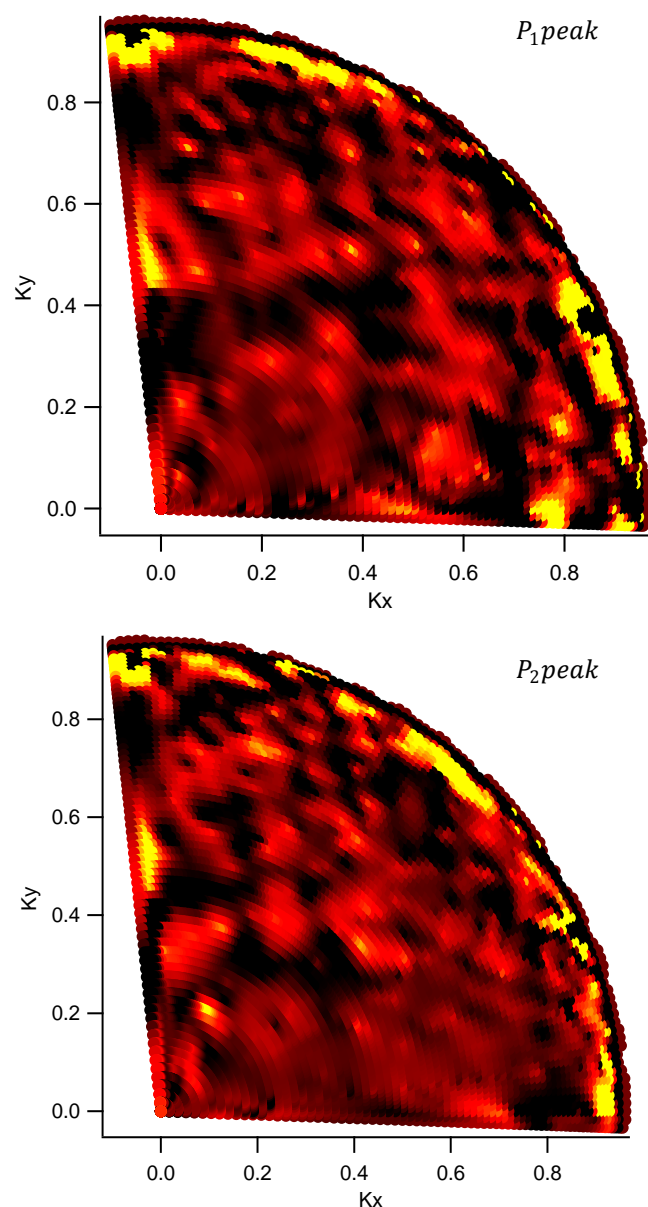


Fig. 6.19. Surface anisotropy function χ versus k_x and k_y for P_1 and P_2 peaks derived from **PED** measurements.

The resulting anisotropy **PED** patterns were more disordered than those on the prototype *Mn/Ge* system [35]. This was attributed to the high reactivity of *Mn* with the *GaAs* surface confirming the formation of several compounds revealed by **STM** and **XPS** measurements. However, some symmetry of the observed anisotropic features suggested that a more quantitative data analysis could supply information on the *Mn* adsorption site;

for this reason a simulation with *EDAC* software⁸ (Electron Diffraction in Atomic Clusters for core level photoelectron diffraction simulations) was done. A simple *GaAs* cluster of 58 atoms was built and a *Mn* atom was positioned on a tetrahedral site over a bulk terminated surface (Fig. 6.20(a)); a second simulation was done with *Mn* atom in the second layer *Ga* substitutional site (Fig. 6.21(a)); in both cases the *Mn* atom has been selected as the emitter point.

In the simulation procedures 8 orders of multiple shell scattering were used. To calculate the anisotropy χ , the zero order of multiple scattering has been taken as the non diffractive intensity I_0 . Therefore the anisotropy has been plotted as a function of polar coordinates to permit the comparison with experimental data (Fig. 6.20(a) and 6.21(b)). In the case of *Mn* atom positioned over the *GaAs* bulk terminated surface, the experimental data for the P_1 peak appear to have some similarity with the simulated data especially at the borders where dark areas and bright areas correspond. In the case of the P_2 peak the comparison with simulated data does not reveal significant similitude. A further simulation has been performed with *Mn* positioned at the *As* interstitial site (not shown) and the comparison of the simulated pattern was in complete disagreement with experiment.

These results confirm that the P_1 peak is associated to metallic *Mn* (or $MnAs_x$) and that *Mn* atomic clusters still reside on the surface after annealing. This conclusion agrees with the **XPS** analysis of *Mn 2p* spectrum (Fig. 6.12). This result is expected as the stoichiometry of *Mn* that diffuses inside the *GaAs* substrate is not yet known, and, as said above, *Mn* reacts with *GaAs* forming *GaMnAs* or *MnAs* forming a very disordered surface structure. We also have to consider that the simulation has been done on a bulk terminated surface while our actual surface was an initial $c(4 \times 4)$ and a successive asymmetric (1×2) after the *Mn* deposition and annealing.

⁸ <http://nanophotonics.csic.es/software/default.aspx>

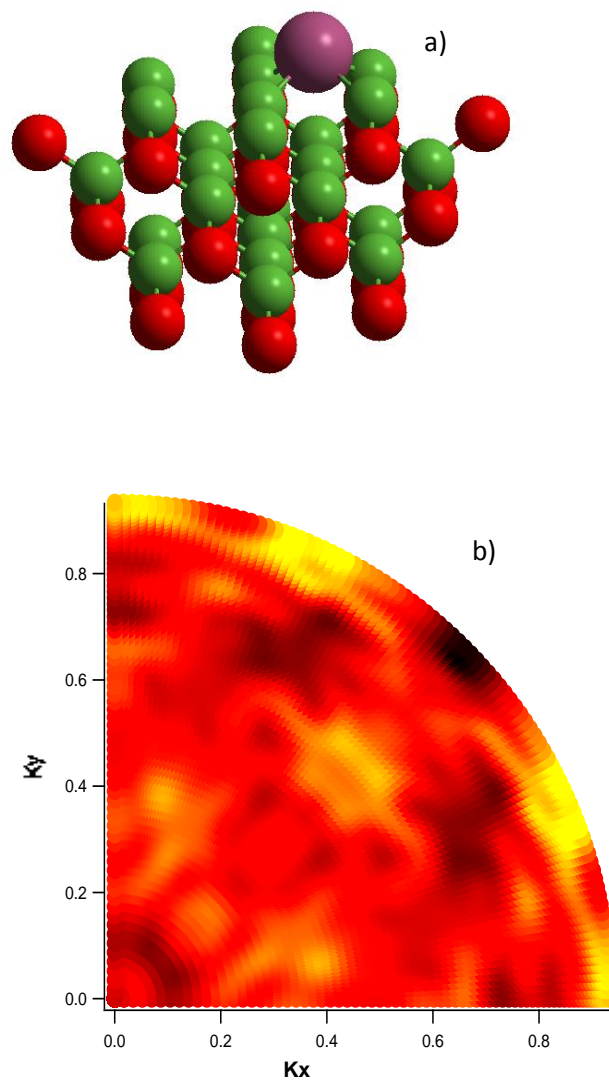


Fig. 6.20. Surface anisotropy in polar coordinates derived from **PED** simulation performed by **EDAC** simulation program with *Mn* atom positioned on the surface in a tetrahedral site (b). The atomic cluster used in the simulation is shown (*Ga* atoms are the red balls, *As* atoms are the green balls and *Mn* atoms is the violet ball) (a).

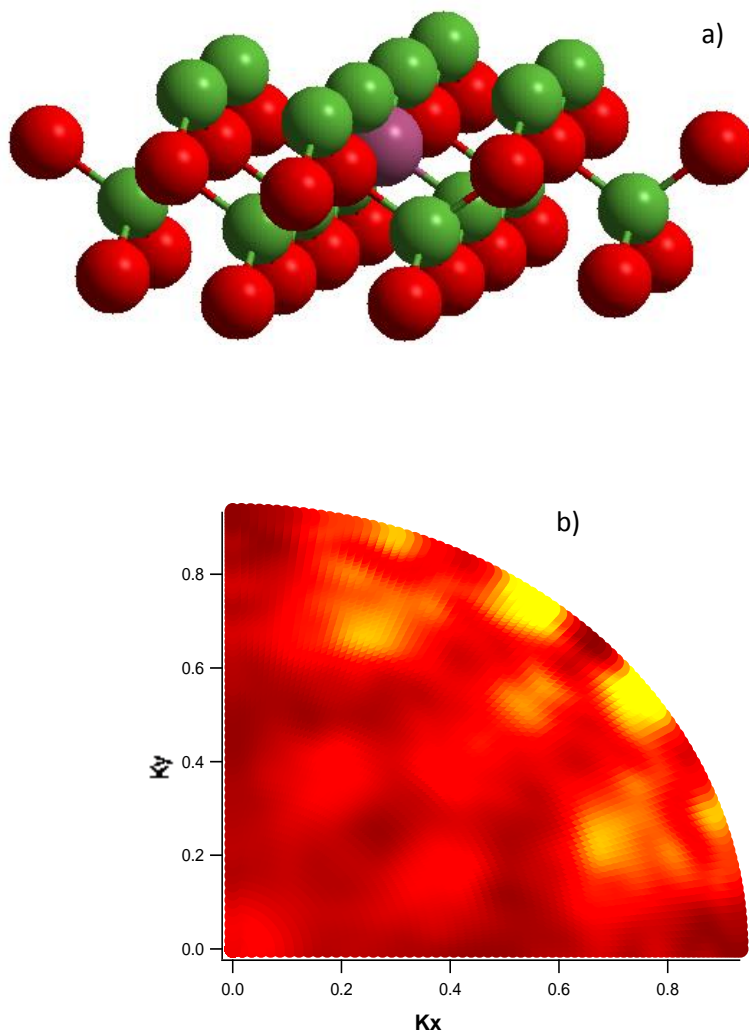


Fig. 6.21. Surface anisotropy in polar coordinates derived from *PED* simulation performed by *EDAC* simulation program with *Mn* atom positioned in a second layer *Ga* substitutional site (b). The atomic cluster used for the simulation is shown (*Ga* atoms are the red balls, *As* atoms are the green balls and *Mn* atoms is the violet ball) (a).

References.

- [1] S. C. Erwin and A. G. Petukhov *Phys. Rev. Lett.* **89**, **227201** (2002).
- [2] Y.L. Soo, G. Kioseoglou, S. Kim, X. Chen, H. Luo, Y.H. Kao, H.J. Lin, H.H. Hsieh, T.Y. Hou, C.T. Chen, Y. Sasaki, X. Liu, and J.K. Furdyna, *Phys. Rev. B* **67**, **214401** (2003).
- [3] J. Okabayashi, A. Kimura, O. Rader, T. Mizokawa, A. Fujimori, T. Hayashi and M. Tanaka *Phys. Rev. B* **64**, **125304** (2001).
- [4] L. P. Rokhinson, Y. Lyanda-Geller, Z. Ge, S. Shen, X. Liu, M. Dobrowolska and J. K. Furdyna *Phys. Rev. B* **76**, **161201(R)** (2007).
- [5] Y. Ohno, D. K. Young, B. Beschoten, F. Matsukura, H. Ohno and D. D. Awschalom *Nature* **402**, **709** (1999).
- [6] W. Monch, *Semiconductor Surface and Interface* Springer & Verlag (1993).
- [7] G.Ertl, J. Koppers *Low Electron Energy and Surface Chemistry* (1984).
- [8] Specification CLAM 100, VG Scientific LTD.
- [9] J. Okabayashi, A. Kimura, T. Mizokawa, A. Fujimori, T. Hayashi and M. Tanaka *Phys. Rev. B* **59**, **R2486 - R2489** (1999).
- [10] B. Kramer, G. Tomasch, J. E. Greene, L. Salvati, T. L. Barr, M. A. Ray *Phys Rev B* **46**, **1372 - 1376** (1992).
- [11] M. J. Begarney, L. Li, C. H. Li, D. C. Law, Q. Fu, and R. F. Hicks *Phys. Rev. B* **62**, **8092** (2000).
- [12] F. Arciprete, C. Goletti, E. Placidi, P. Chiaradia, M. Fanfoni, F. Patella, C. Hogan, and A. Balzarotti *Phys. Rev. B* **68**, **125328** (2003).
- [13] A. Balzarotti, M. Fanfoni, F. Patella, F. Arciprete, E. Placidi, G. Onida, R. Del Sole *Surf. Sci.* **524**, **L71–L76** (2003).
- [14] C. Hogan, E. Placidi and R. Del Sole *Phys. Rev. B* **71**, **041308(R)** (2005).
- [15] T. Dielt, H. Ohno *MRS Bull.* **28**, **714** (2003)
- [16] K. Ando, T. Hayashi and M. Tanaka *J. Appl. Phys.* **83**, **6548** (1998).
- [17] T. Jungwirth, J. Sinova, J. Mašek, J. Kučera and A. H. MacDonald *Rev. Mod. Phys.* **78**, **809** (2003).

- [18] F. Arciprete, C. Goletti, E. Placidi, C. Hogan, P. Chiaradia, M. Fanfoni, F. Patella, and A. Balzarotti *Phys. Rev. B* **69**, 081308 (2004).
- [19] A. Balzarotti, E. Placidi, F. Arciprete, M. Fanfoni, F. Patella *Phys. Rev. B* **67**, 115332 (2003).
- [20] A.M. Yakunin, A.Yu. Silov, P.M. Koenraad, W. VanRoy, J. De Boeck, J.H. Wolter *Phys. E* **21**, 947 – 950 (2004).
- [21] E. Placidi *PhD thesis* (2002) *Physics Department* University of Rome Tor Vergata.
- [22] S. D. Thorpe, F. Arciprete, E. Placidi, F. Patella, M. Fanfoni, A. Balzarotti, S. Colonna, F. Ronci, A. Cricenti, A. Verdini, L. Floreano and A. Morgante *Superlattices and Microstructures* **46**, 258-265 (2009).
- [23] *Metal-Semiconductor Contacts* Ed. by E.H. Rhoderick and R.H. Williams, Oxford Science Publications (1988).
- [24] S.P. Guo, A. Shen, H. Yasuda, Y. Ohno, F. Matsukura, H. Ohno *J. Cry. Gr.* **208**, 799 (2000).
- [25] Y. Ohno, D. K. Young, B. Beschoten, F. Matsukura, H. Ohno D. D. Awschalom, *Nature* **402**, 790 (1999).
- [26] S. A. Hatfield, T. D. Veal, C. F. McConville, G. R. Bell, K. W. Edmonds, R. P. Campion, C. T. Foxon, B. L. Callagher *Surf. Sci.* **585**, 66–74 (2005).
- [27] M. Oshima, M. Mizuguchi, K. Ono, H. Akinaga, M. Sugiyama *J. Elect. Spect. Rel. Phen.* **124**, 165-174 (2004).
- [28] R. J. Iwanowski, M.H. Heinonen, E. Janik *Chem. Phys. Lett.* **287**, 110-115 (2004).
- [29] H. A. Dürr, G. van der Laan, D. Spanke, F. U. Hillebrecht N. B. Brookes *Phys. Rev. B* **56**, 8156 (1997).
- [30] L. Ottaviano, M. Passacantando, A. Verna, F. D’Amico, R. Gunnella *Appl. Phys. Lett.* **90**, 242105 (2007).
- [31] F. Maccherozzi, G. Panaccione, G. Rossi, M. Hochstrasser, M. Sperl, M. Reinwald, G. Woltersdorf, W. Wegscheider, and C. H. Back *Phys. Rev. B* **74**, 104421 (2006).
- [32] P. De Padova, J.-P. Ayoub, I. Berbezier, P. Perfetti, C. Quaresima, A.M. Testa, D. Fiorani, B. Olivieri, J.-M. Mariot, A. Taleb-Ibrahimi, M.C. Richter, O. Heckmann, K. Hricovini *Phys. Rev. B* **77**, 045203 (2008).

- [33] A. Ohtake, J. Nakamura, S. Tsukamoto, N. Koguchi, and A. Natori *Phys. Rev. Lett.* **89**, 06102 (2002).
- [34] T. Arai, M. Suzuki, Y. Ueno, J. Okabayashi, J. Yoshino *Physica E* **40**, 332–334 (2007).
- [35] A. Verdini, A. Cossaro, L. Floreano, A. Morgante, A. Goldoni, D. Ghidoni, A. Sepe, S. Pagliara, and L. Sangaletti *Phys. Rev. B* **77**, 075405 (2008).

Chapter 7

Conclusions

The aim topics of this work were:

- morphologic and electronic properties of the $GaMnAs(001)$ surface investigation;
- interaction mechanism of Mn with $GaAs(001)$ substrate study.

Firstly, a high quality $GaMnAs$ surface was grown by **MBE**, characterizing the surface quality by in situ **RHEED** and performing a successive investigation of the magnetic and structural properties by **MOKE**, **XRD**, **TEM**, and **EXAFS** measurements. These techniques confirmed the good magnetic property with a well determined T_c variation as a function of Mn concentration and the high quality of the structural properties with almost all Mn atoms occupying the Ga substitutional site. Further and deeper investigation on the $GaMnAs$ surface was performed with *in situ* **RAS**, **EELS**, **XPS** and **STM** measurements. **RAS** spectra revealed the presence of a surface contribution at about 2 eV and 3 eV . Comparing this results with literature data, a clear indication was obtained. $GaMnAs(001)$ surface maintains some characteristics of the $GaAs(001)c(4 \times 4)$ surface, in which surface features at the same energy are present, the structures around 2 eV attributed to surface $As - As$ dimers and the ones around 3 eV to the dangling bonds contribution of the second layer As atoms. The shape of **RAS** spectrum is also very similar to the $GaAs(001)(1 \times 2)$ surface one, where random distribution of $As - As$ dimers was observed. A similarity of the experimental **RAS** spectrum of the $GaAs(001)c(4 \times 4)$ surface with the simulated one in which symmetric dimers are present has been found, confirming the nature $As - As$ of the $GaMnAs(001)$ dimers. **EELS** measurements showed less clear spectra because the surface was very disordered and this technique has higher surface sensitivity than **RAS**. An observed presence of contribution around 2 eV has been explained by $p - d$ hybridization. The $p - d$

hybridization was confirmed by **XPS** measurements. **STM** measurements on this surface revealed the presence of blocks on the $[1\bar{1}0]$ similar to the ones reported for the $GaAs(001)c(4 \times 4)$ surface, which are formed probably by $As - As$ dimers. These evidences, complementary to **EELS** and **RAS** results, suggested a probable surface configuration in which the Mn atoms are positioned in sites under $As - As$ dimers. This interpretation is confirmed by theoretical models.

In order to understand the Mn interaction with $GaAs(001)$ substrate at the first stages of growth, $GaAs(001)c(4 \times 4)$ samples were prepared by **MBE** and a subsequent Mn deposition (1 *ML*) with a further annealing at $250^\circ C$, replying the conditions of $GaMnAs$ **MBE** growth. After Mn deposition, the surface showed a transition to 1×1 periodicity and after annealing a further transition was observed by **RHEED** to 1×2 reconstruction, the same reconstruction obtained on $GaMnAs$ after **MBE** growth. Synchrotron radiation measurements were carried out to characterize the surface by **XPS**, **XAS** and **PED** techniques.

STM characterization has been performed before and after low temperature annealing on $Mn/GaAs$ surface. The **XPS** $As\ 3d$ core level results suggested that Mn reacts with the surface and that the annealing procedure favors Mn atoms diffusion inside the $GaAs$ bulk. Moreover, the **XPS** $Mn\ 2p$ core level results confirmed this behavior and suggested that, after Mn deposition, several compounds as $GaMnAs$, $MnAs$, $MnAs_x$ and Mn in metallic clusters are formed. The annealing process tends to reduce the metallic component at the surface; this feature was confirmed by **PED** measurement and the presence of $GaMnAs$ was confirmed by **XAS** spectra. Finally **STM** measurements revealed surface disorder after Mn deposition and a rearrangement after annealing with more ordered structure along the $[110]$ direction.

In conclusion, for the first time the $GaMnAs(001)$ surface was deeply investigated. Further measurements are required to get a better knowledge of the $GaMnAs$ structure and of the $Mn/GaAs$ interaction. These aspects could lead to important information regarding the $GaMnAs$ growth in order to improve the structural and magnetic properties of this compound, a promising material for forthcoming spintronic devices.

Appendix. Future developments

A. Cross sectional *STM* measurement of *GaMnAs*(001) surface

Enhancing ferromagnetism in semiconductors requires the study of the mechanisms for interaction between magnetic dopants and the identification of the circumstances that maximize ferromagnetic interactions between dopants (see Chapter 3). A recent work by the C. T. Foxon group [1] has confirmed that the enhancement of T_c is possible when increasing the quantity of *Mn* percentage in substitutional site of *GaMnAs* structure. This was achieved optimizing the growth parameters and post growth annealing demonstrating that for $x \approx 0.12$ the Curie temperature reaches about 185 K. The connection between T_c and *Mn* impurities concentration is related to the *Mn* wave function distribution in the *GaAs* lattice. Moreover the study of density of states on the growth surface could give important information. Unfortunately the study of the (001) surface, as we have seen, is very difficult and a possible technique to investigate the surface impurities in the *III – V* host is the Cross Sectional *STM* (*X-STM*). This technique is performed by a sample cleavage inside the measurement chamber where *UHV* is maintained to avoid sample contaminations to obtain a clean surface without any sputtering or annealing treatment. The inconvenient is that in this way it is possible to investigate only the (110) surface. This method has already been widely used in the case of $Ga_{1-x}Mn_xAs$ surface with low percentage of *Mn* ($\ll 1\%$) [2,3,4,5] and *Mn* evaporation after *GaAs* cleavage where the *Mn* distribution function on the *GaAs*(110) surface is observed [6,7,8]. It could be very interesting to investigate the behavior of *Mn* by increasing the percentage of *p* impurities and study the *Mn* distribution function in the case of many *Mn – Mn* interactions. For this reason we grew a $Ga_{1-x}Mn_xAs$ sample for *X-STM* measurement with the procedure described in section 5.3 with a high concentration of *Mn* ($3\% < x < 4\%$).

For *cross sectional STM* measurements (section 4.5) a thick layer was grown (about 2 μm) because the mechanical cleavage could destroy the first layers of the film. In addition

a layer of about 40 nm of *AlGaAs* was grown as a marker before the *GaMnAs* layer. In fact, because *AlGaAs* has a lower density of electronic states than *GaAs* and *GaMnAs*, in the **STM** images it appears darker so to act as a marker to recognize the different areas as, demonstrated in ref. [9] (Fig. A.3).

To obtain good adhesion and ohmic electrical contacts between sample and holder a sequence of different metallic layers have been deposited by thermal evaporation after growth: germanium, nickel and gold ($50\text{\AA} Au - 300\text{\AA} Ge - 200\text{\AA} Ni$), which act as an antioxidation layer; a subsequent annealing at 250°C has been performed to obtain a better interdiffusion of materials [10]. The ohmic contact was deposited on the back side of the sample because a simple mechanical contact between sample and holder is not sufficient to avoid the formation of a Schottky barrier due to a difference in the electron affinity of materials. The sample (*epi-ready* substrate + **MBE** growth) is normally 250 – 600 μm thick; from such thickness of the samples, it is hard to obtain very good surface by cleavage, which is absolutely necessary for the measurements of weak electronic structures in the case of *p-type* impurities in *GaAs*. Therefore the samples were polished down to a thickness of about 90 μm . In Fig. A.1 it is possible to observe the difference of the (110) cleaved surface obtained from samples of different thickness (500 μm and 90 μm) and how the amount of surface defects coming from cleavage decreases by reducing the sample thickness. The homemade **STM** sample holder (Fig. A.2) for cleavage was composed of two stainless steel bars that could be screwed together. A corner of the sample, in correspondence of the notch described below, was clamped between the two bars. One of these bars was fixed to a support plate that tightly fits in the **STM** unit. A thin slice of indium (*In*) was placed at the clamping point on both sides of the sample holder before the sample was clamped. The sample holder was then heated over the indium melting temperature (about 157°C) and the screws were tightened. The indium provided for an even pressure distribution on the sample as well as for a fixed electrical contact. Before the sample was clamped into the sample holder, a small scratch of about 0.5 mm, which extends to a small notch at the side of the sample, was applied to the epi-layer side of the sample, by using a diamond pen. The position of this scratch was chosen in such a way that after the sample was clamped into the holder, it would be located just above the clamping bars. This scratch acted as a nucleation

point for the (110) cleavage-plane of the sample later on in the *UHV* chamber. This procedure greatly enhances the quality of the cleavage plane. It is important to note that the scratch should be shallow enough to only nucleate the cleavage plane but not to determine the cleavage direction.

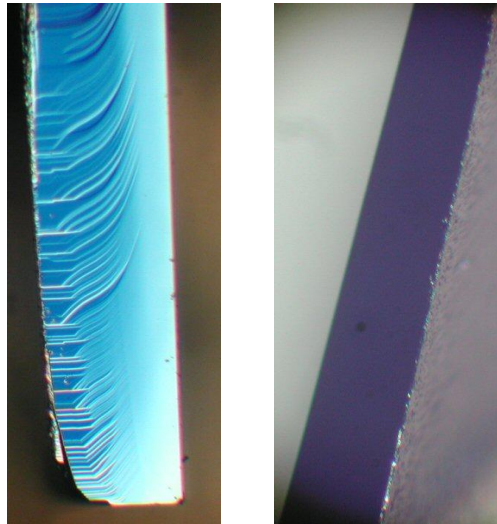


Fig. A.1. Cleavage of a *GaMnAs* sample before (left $500\mu\text{m}$) and after (right $90\mu\text{m}$) polishing procedure observed by an optical microscope. It is possible to observe the drastic decrease of defects amount.

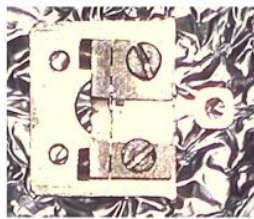


Fig. A.2. Sample holder for cross sectional STM.

After a degassing process performed in the preparation chamber at 250°C to remove the adsorbed impurities, the sample was cleaved in situ (base pressure of 10^{-10}mbar) by pressing the sample bar at one corner using the transfer arm of the vacuum chamber. Fig. A.3 (a) shows a wide area *STM* image ($2000 \times 2000\text{ nm}$). It is possible to recognize the three layers (A, B and C); the layer with the presence of *Mn* (A), the the dark strip of *AlGaAs* layer (B) and *GaAs* buffer layer (C); the thickness of *AlGaAs* layer is larger than 50nm

because the *Al* during the growth diffuse inside the *GaAs* substrate (it is possible to observe the diffusion in Fig. A.3 (b) where a lighter strip is observed on the left side of the *AlGaAs* layer). On the right of the dark strip it is possible to observe the thin layer of *GaAs* (10nm) grown before the *GaMnAs* layer. A spectroscopy of the surface was performed for each area (Fig. A.4). The results shows the typical gaps of each compound and in particular the reduction of *GaMnAs* gap with respect to *GaAs* gap (1.25 eV for *GaMnAs* and 1.45 eV for *GaAs*). The measurements were performed at room temperature.

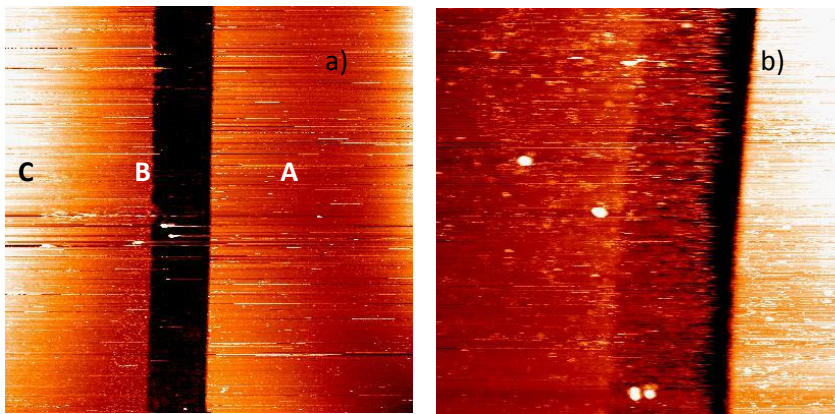


Fig. A.3. *X-STM* images of *GaMnAs*(110) surface of a sample formed by three layer: *GaAs* substrate (C) *AlGaAs* layer (B) used as a marker and *GaMnAs* layer (A). The images were taken at -2V and 0.1nA. The dimensions are 2000 × 2000 nm (a) and 1000 × 1000 nm (b).

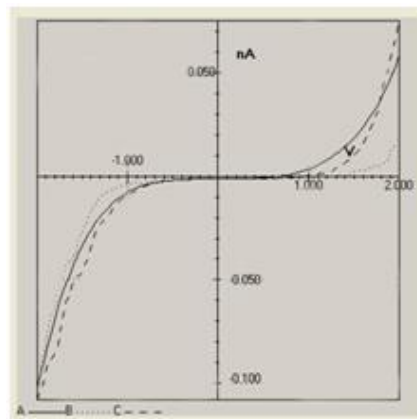


Fig. A.4. Spectroscopies acquired for each layer (A,B and C). The gap of *GaMnAs* layer (1.25 eV) results lower respect to the *GaAs* gap (1.45 eV). The *AlGaAs* layer has a gap greater than 2 eV.

We concentrate our attention on the *GaMnAs* layer trying to identify *Mn* atoms. The result is shown in Fig A.5; the measurement was performed in dual mode (empty and filled states) at $\pm 0.8 V$ and $0.2 nA$. Constant current images permit to observe the round structures in empty states and cross-like feature in the filled states [4,5] of *Mn* atoms. It has been suggested that **STM** images of subsurface impurities are mainly due to the hybridization of impurity states with intrinsic surface states ($p - d$ hybridization) [11]. Comparing our results with the ones of ref. [4,5] it is possible to argue that also in the case of high *Mn* concentration the shape does not change and so the *Mn* distribution function remains the same.

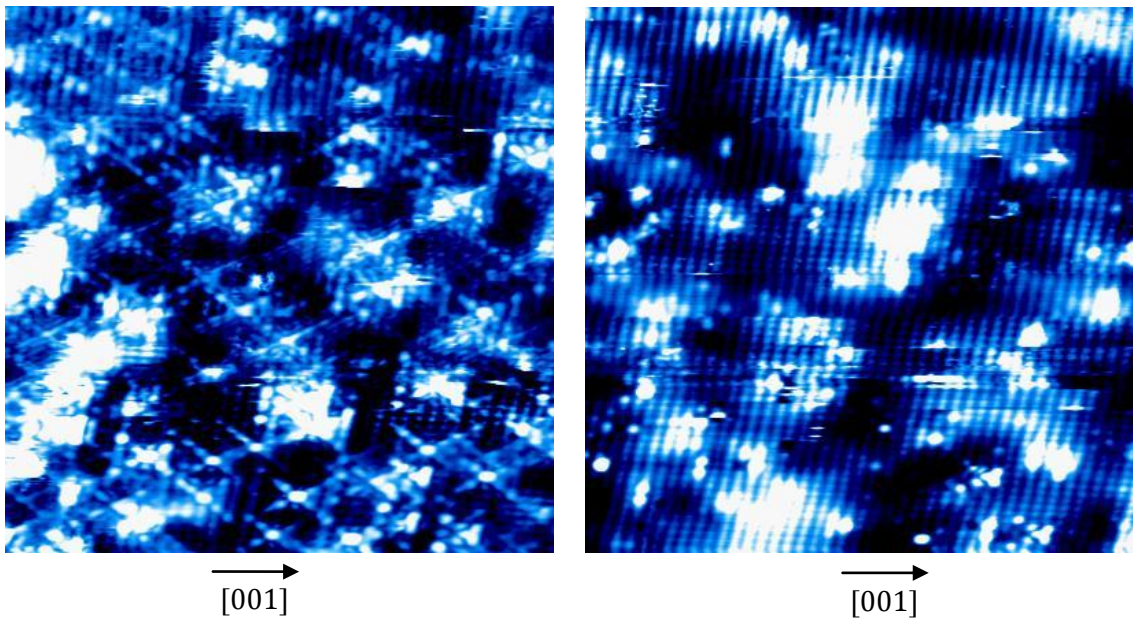


Fig. A.5. Filled (left) and empty (right) electronic **STM** images states of *GaMnAs*(110) surface. The images were acquired with $0.8 V$ and $0.2 nA$. The size is $20 \times 20 nm$.

These studies could be continued investigating the distribution function of *Mn* atoms as a function of higher dopant concentration and varying the sample temperature near T_c .

B. STM measurement on *Mn*: *GaAs*(001) $\beta 2(2 \times 4)$ surface

To obtain a deeper understanding about the interaction between *Mn* and *GaAs* surface, it is interesting to study the surface morphology as a function of *Mn* deposition and thermal treatment with a starting *GaAs*(001) $\beta 2(2 \times 4)$ surface; this surface is thermodynamically more stable than the $c(4 \times 4)$ one allowing annealing treatments at higher temperatures avoiding the surface degradation. For this reason a *GaAs*(001) $c(4 \times 4)$, more simple to prepare, was grown by *MBE* reactor with a consequent *As* capping layer deposition (see Chapter 5). The sample was mounted in the *STM* preparation chamber. After the decapping procedure of the sample (see Chapter 5), it was heated at about 450°C and a transition to $\beta 2(2 \times 4)$ occurred (Fig. B.1).

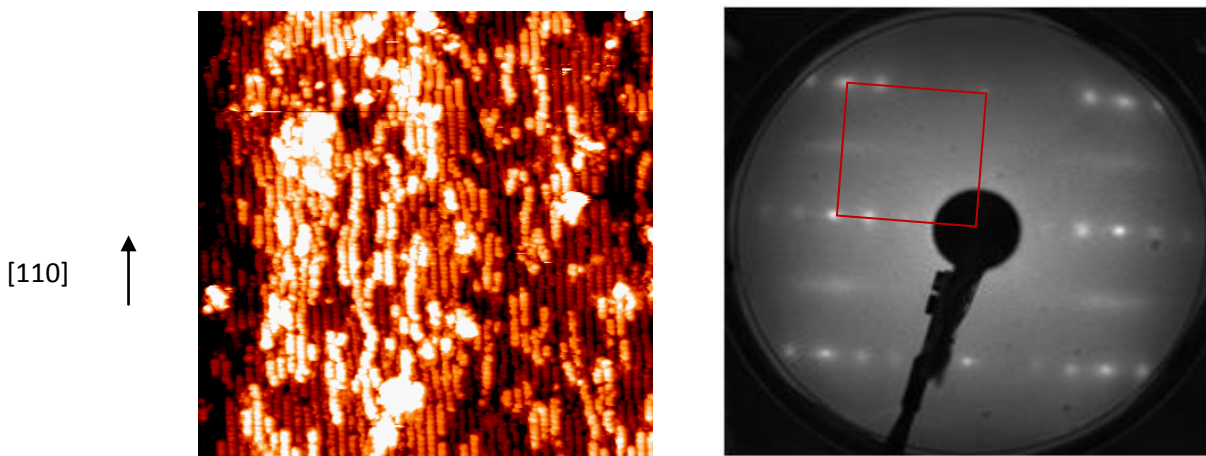


Fig. B.1. *STM* images of the *GaAs*(001) $\beta 2(2 \times 4)$ surface ($(100 \times 100) \text{ nm}^2$) after decapping and annealing at 450°C with the related *LEED* pattern taken with beam energy $E_p = 43 \text{ eV}$. For the *STM* image $V = -5 \text{ V}$ and $I = 0.1 \text{ nA}$.

After the deposition of 0.4 \AA of *Mn* ($1/2 \text{ ML}$) it is possible to observe a more disordered surface with a weaker 2×4 reconstruction in the *LEED* pattern (Fig. B.2).

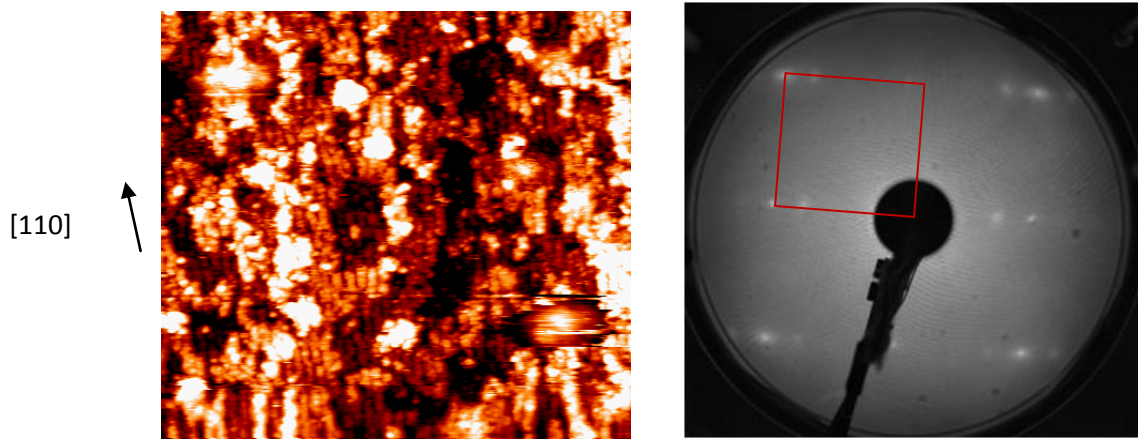


Fig. B.2. **STM** images of the $GaAs(001)\beta_2(2 \times 4)$ surface ($(100 \times 100) \text{ nm}^2$) after the deposition of 0.4 \AA ($1/2ML$) of Mn with the related **LEED** pattern taken with beam energy $E_p = 45 \text{ eV}$. For the **STM** image $V = -4 \text{ V}$ and $I = 0.05 \text{ nA}$.

After a further annealing at 390°C , the surface results more ordered with structures aligned along the $[110]$ direction and a 2×1 reconstruction (Fig. B.3) at variance with Mn : $GaAs(001)c(4 \times 4)$ that has a weak 1×2 reconstruction after annealing.

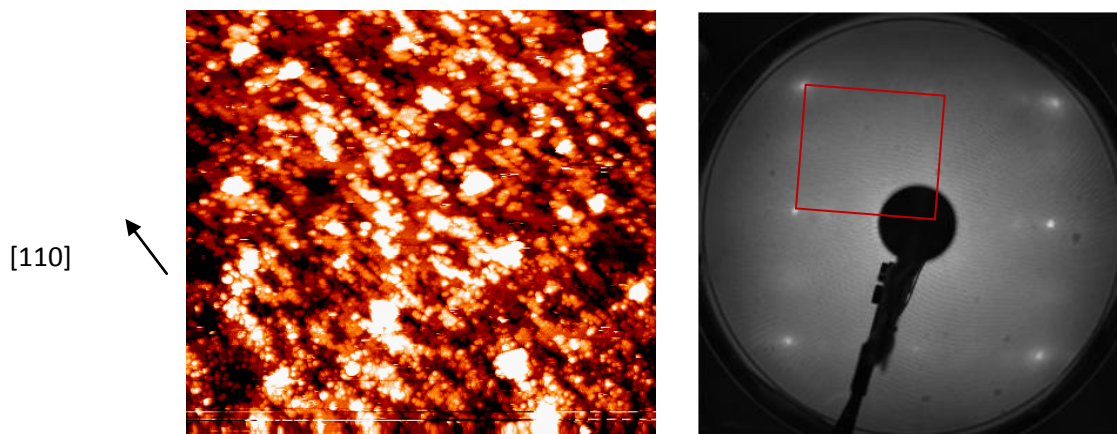


Fig. B.3. **STM** images of the $GaAs(001)\beta_2(2 \times 4)$ surface ($(100 \times 100) \text{ nm}^2$) after annealing at 350°C with the related **LEED** pattern taken with beam energy $E_p = 45 \text{ eV}$. For the **STM** image $V = -5 \text{ V}$ and $I = 0.1 \text{ nA}$.

Only after an annealing at about 440°C the surface shows a clear 2×1 reconstruction with more evidence of structures oriented in the $[110]$ direction (Fig B.4).

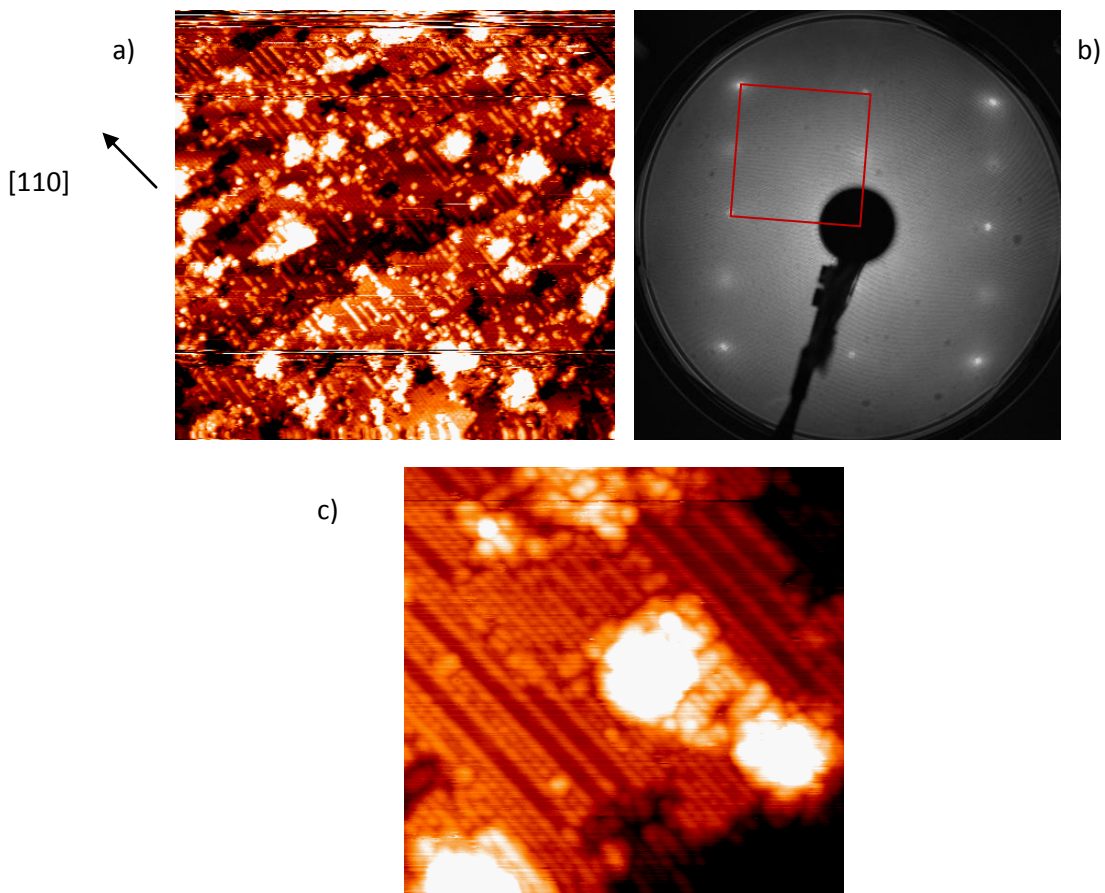


Fig. B.4. **STM** images of the $GaAs(001)\beta_2(2 \times 4)$ surface ($(100 \times 100)nm^2$ (a) and $(35 \times 35)nm^2$ (c)) after further annealing at $390^\circ C$ and $440^\circ C$ with the related **LEED** pattern taken with beam energy $E_p = 45 eV$. For the **STM** image $V = -5 V$ and $I = 0.1 nA$ (b).

These results give important information regarding the crucial role of the annealing to obtain high quality surface probably correlated to $Mn - As$ interaction. This indications lead us to perform a Mn deposition on $GaAs(001)\beta_2(2 \times 4)$ with the $GaAs$ substrate pre-heated at $390^\circ C$, in conditions more similar to **MBE** growth ones.

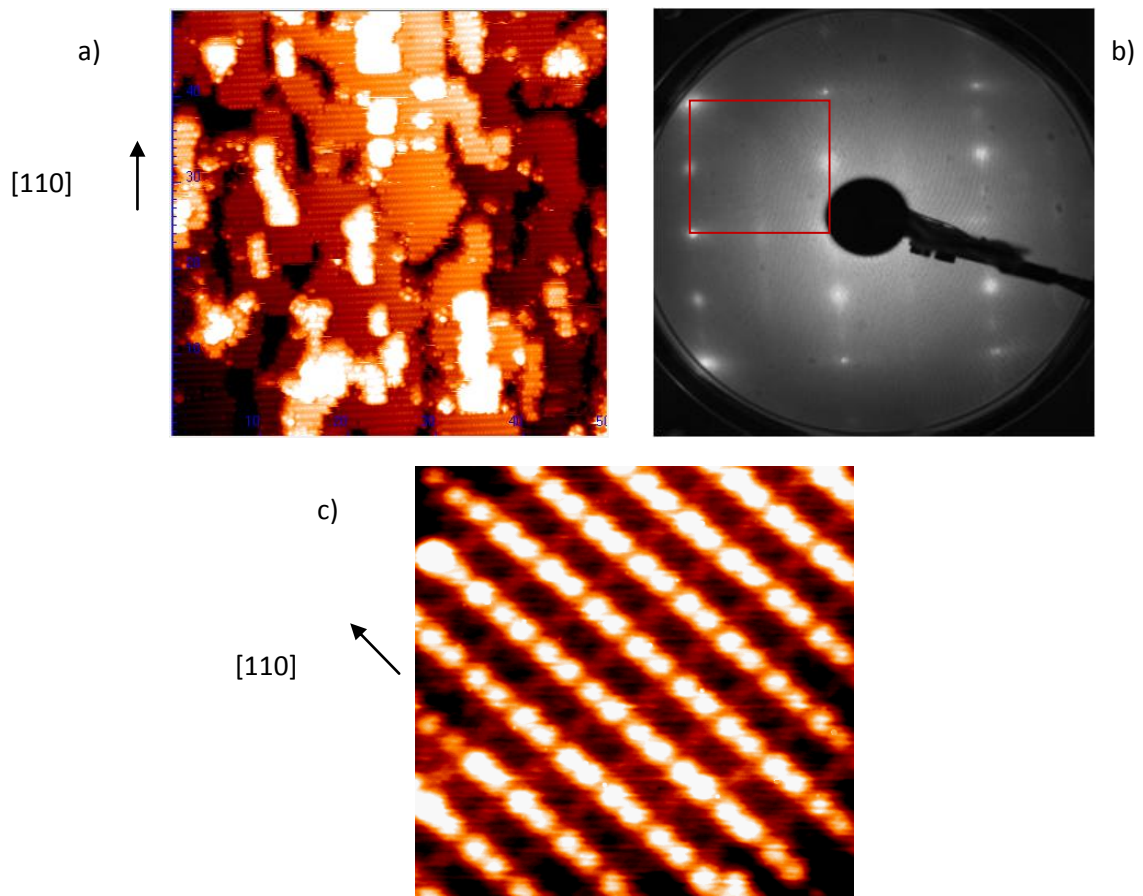


Fig. B.5. **STM** images of the $GaAs(001)\beta_2(2 \times 4)$ surface ($(100 \times 100)nm^2$ (a) and $(35 \times 35)nm^2$ (c)) after further annealing at $390^\circ C$ and $440^\circ C$ with the related **LEED** pattern taken with beam energy $E_p = 46 eV$. For the **STM** image $V = -5 V$ and $I = 0.1 nA$ (b)

In these preliminary results it is possible to observe the high quality of the surface obtained with the Mn deposition on heated sample, contrary to the surface obtained with Mn deposition and successive annealing. Moreover in the **STM** image in Fig. B.5(c) it is possible to observe the presence of atomic resolution and the presence of structures that could be related to dimers ($As - Ga$ or $As - As$). The presence of dimers could be related to the dimers observed in $GaMnAs$ even if the starting surface in this case is $GaAs(001)\beta_2(2 \times 4)$. This could be a very interesting point for studies concerning the interaction of Mn with $GaAs$ substrate which deserves a wider investigation.

References

- [1] M. Wang, R. P. Campion, A. W. Rushforth, K. W. Edmonds, C. T. Foxon, and B. L. Gallagher *Appl. Phys. Lett.* **93**, **132103** (2008).
- [2] J. M. Sullivan, G. I. Boishin, L. J. Whitman, A. T. Hanbicki, B. T. Jonker, and S. C. Erwin *Phys. Rev. B* **68**, **235324** (2003).
- [3] A. Stroppa, X. Duan, M. Peressi, D. Furlanetto, and S. Modesti *Phys. Rev. B* **75**, **195335** (2007).
- [4] A. M. Yakunin, A.Yu. Silov, P.M. Koenraad, J. H.Wolter, W.Van Roy, J. De Boeck, J.-M. Tang, and M. E. Flatté *Phys. Rev. Lett.* **92**, **216806-1** (2004).
- [5] A. M. Yakunin, A.Yu. Silov, P. M. Koenraad, J.-M. Tang, M. E. Flatté, W. Van Roy, J. De Boeck, and J. H. Wolter *Phys. Rev. Lett.* **95**, **256402** (2005).
- [6] D. Kitchen, A. Richardella, J.-M. Tang, M. E. Flatté and A. Yazdani *Nature* **442**, **436** (2006).
- [7] D. Kitchen and A. Richardella P. Roushan J.-M. Tang and M. E. Flatté A. Yazdani *J. Appl. Phys.* **101**, **09G515** (2007).
- [8] D. Kitchen, A. Richardella, A. Yazdani *J. Superc.: Incorp. Nov. Magn.* **18**, **23** (2005).
- [9] T. Tsuruoka, N. Tachikawa, S. Ushioda, F. Matsukura, K. Takamura, and H. Ohno *Appl. Phys. Lett.* **81**, **2800** (2002).
- [10] N. Braslau, J. B. Gunn, J. L. Staples, *Sol. St. Electr.* **10**, **381** (1967).
- [11] J.-M Jancu, J.-C. Girard, M.O. Nestoklon, A. Lemaître, F. Glas, Z. Z. Wang, and P. Voisin *Phys. Rev. Lett.* **101**, **196801** (2008).

Ringraziamenti

Vorrei ringraziare innanzitutto il Prof. Adalberto Balzarotti per avermi dato la possibilità di svolgere il dottorato nel suo laboratorio e tutto il suo gruppo in particolare il Dr. Fabrizio Arciprete e il Dr. Ernesto Placidi che mi hanno insegnato molto e con cui ho passato piacevoli giornate ... molto lunghe nel caso delle crescite! Vorrei ringraziare il Dr. Antonio Cricenti che mi ha permesso di svolgere tutta l'attività di microscopia presso l'ISM e di tutto il suo gruppo (Fabio, Paola, Marco, Gianni e Giuliano) e soprattutto vorrei ringraziare il mio relatore Dr. Stefano Colonna grazie al quale con i suoi stimoli, suggerimenti e telefonate è stata realizzata questa tesi tra mille peripezie (e senza il quale probabilmente non avrei finito neanche la stesura). Vorrei ringraziare tutta la mia famiglia che mi ha sempre sostenuto (specialmente economicamente ... vero mamma?) e ha sempre creduto in me. Vorrei fare inoltre una dedica a mia moglie che mi ha sostenuto sempre nei momenti di depressione e mio figlio, piccolo Simon, che con i suoi sorrisi mi ha sempre dato una marcia in più. Un ringraziamento speciale anche a tutti i miei cari amici che mi hanno spinto a finalizzare i miei sforzi (Roberto, Marco, Sandro e Mario).